COMPREHENSIVE ANALYSIS OF FILTER INDUCTOR ASYMMETRY ON CONDUCTED EMISSIONS IN BUCK AND BOOST CONVERTERS

by

JARED C HELTON

ANDREW LEMMON, COMMITTEE CHAIR
AARON BROVONT
TODD FREEBORN

A THESIS

Submitted in partial fulfillment of the requirements for the
degree of Master of Science in the Department of
Electrical and Computer Engineering
in the Graduate School of
The University of Alabama

TUSCALOOSA, ALABAMA

2020

ABSTRACT

Increased edge rates and switching frequencies have led to higher efficiency and increased power density for dc-dc converter topologies utilizing wide band-gap (WBP) devices. These improvements in intended behavior come with a cost in the form of elevated EMI profiles and higher magnitude CM currents, which cause challenges in fielded systems. Therefore, there is an increasing need to model the CM behavior for these systems and provide efficient EMI mitigation techniques. A method to decompose a system's mixed-mode (MM) behavior into its differential-mode (DM) and common-mode (CM) behavior is utilized in this thesis. This thesis analyzes the role of filter inductor asymmetry in decreasing emissions in common dc-dc converters while preserving the intended behavior of these systems.

The proposed decomposition method is applied to buck and boost converters. This method produces common-mode equivalent models (CEMs) that provide simplified expressions for the CM behavior of systems. CEMs are developed for both simplified and practical implementations of the considered topologies. Analysis of these CEMs reveals that both converters demonstrate similar CM behavior trends for the simplified models but exhibit different CM behavior trends for the practical models. Two prototype buck converters are then utilized to empirically validate the CEMs for this topology. A low-power prototype is utilized to validate the simplified model. This example demonstrates the necessity of considering high-frequency voltage ripple to accurately represent the CM behavior of this topology. A high-power prototype is utilized to validate the practical model. This example demonstrates the sensitivity of a fielded system to unintended couplings with the grounding network.

LIST OF ABBEVIATIONS AND SYMBOLS

BPC	Baseplate Capacitance
CEM	Common Mode Equivalent Model
CM	Common Mode
DM	Differential Mode
DUT	Device Under Test
E-HEMT	Enhancement Mode High Electron Mobility Transistor
EMC	Electromagnetic Compatibility
EMI	Electromagnetic Interference
EPR	Equivalent Parallel Resistance
EUT	Equipment Under Test
GaN	Gallium Nitride
KVL	Kirchhoff's Voltage Law
MM	Mixed Mode
MOSFET	Metal-Oxide-Semiconductor Field-Effect Transistor
MCPM	Multichip Power Module
PCB	Printed Circuit Board
Si	Silicon
SiC	Silicon-Carbide
SRF	Self-Resonant Frequency
WBG	Wide Band-gap

ACKNOWLEDGEMENTS

I would like to start by thanking Dr. Andrew Lemmon for providing the resources and support in my studies and this thesis. Under his guidance I was able to learn and accomplish more than I would have thought possible. I am grateful for him as a mentor, and for the experiences that he has provided for me that led me to this point.

Additionally, I would like to thank Dr. Aaron Brovont for providing guidance at the onset of my graduate studies. I would have likely never been exposed to this material, and my knowledge as a student would have suffered without his mentorship and guidance.

I would like to thank Dr. Todd Freeborn for being a mentor throughout my time as a graduate student. He has reliably been open and honest as both a person and a professor, and I am grateful for his guidance and advice.

To my coworkers, thank you for providing help and guidance at every possible opportunity. You all allowed me to flourish in this environment, and I will forever be thankful. Chris, without your knowledge and guidance I wouldn't have known where to start let alone been able to achieve half of what is in this thesis. Blake, you provided informative and friendly conversations helped me not only develop my work but also keep my spirits up. Brian, your work with modeling and measuring provided crucial insights into this work that it would've suffered without. Jin, you provided a "Common-Mode Confidante (CMC)" that helped reassure me in my research when I had doubt. Shelby, your constant support as a friend was timely and priceless, and you helped ease the burden of this process. Jamie, your conversations continuously put me in a good mood, which was always welcomed. Sergio, your cheerful attitude was always welcomed, and your

recommendations for the PCB design helped keep any problems at bay. Ali, Marshall, you both provided an amazing atmosphere of positivity and developed learning. Dylan, Henry, you were always upbeat and great to be and work around.

To my family, thank you for your continuous support throughout this process. I could not have achieved what I have without knowing that I had you in my corner. To my mother, Teresa, I can't put words to the support that you provided me from day one, but I'll try with two: thank you. To my father, Alan, you were constantly engaging with my studies and providing advice that I took to heart. To my sister, Jessie, you were my best friend growing up, and you always pushed me to reject complacency. To my grandmother, Princess, you are the greatest role model a grandson could ask for, and my work is done to make you proud. To my close friends – Zach, Tristan, Christy, Foster, Tripp, Nolan, and Joseph – I would be nothing close to the person I am today without your support. You suffered through my rants, yet you still let me tag along. You all represent the best of who I am as a person, and I want to thank you for never wavering in your friendship.

TABLE OF CONTENTS

LIST OF TABLES

LIST OF FIGURES

CHAPTER 1:

INTRODUCTION

The field of power electronics is diverse and is applied where power conversion is necessary. This field ranges from applications in information technology to renewable energy, but the focus of this thesis is on dc-dc converters [1]. As the terminology informs, these converters take an input dc voltage and output a dc voltage that connects to a load. The widespread use of dc-dc converters is due in part to their high efficiency ratings. Many converters topologies are able to achieve greater than 99% efficiency. This efficiency is tied into the recent advances in technology in terms of semiconductors. Semiconductors are the primary active devices for a converter topology. Modern semiconductor devices demonstrate fast transitions that minimize the amount of power loss during switching. In their simplest form, semiconductors switches have two states: on and off. More realistically, these devices have finite rise and fall times, which define the time between the on and off states. The efficiency ratings of dc-dc converters are directly tied to the rise/fall times of the semiconductors utilized for their implementation. Minimizing these transition times is a primary concern for designers seeking to achieve high efficiency for this type of system. Unfortunately, increasing efficiency by implementing fast switching devices also introduces challenges in terms of elevated electromagnetic emissions.

Ongoing advancement in semiconductor technology is leading to higher switching frequency capabilities. Older technologies like insulated-gate bipolar transistors (IGBTs) are able to switch at frequencies on the order of 10 kHz. Newer technologies like silicon-carbide (SiC) and gallium-nitride (GaN) are able to switch at frequencies on the order of 100 kHz or even in the MHz regime [2]. These technologies, called wide bandgap (WBP) devices, enable higher efficiencies and greater power density. However, these improvements come with a tradeoff in the form of elevated emissions. Both radiated and conducted emissions are a concern, but the focus of this thesis is conducted emissions. Fast rise and fall times introduce additional energy into the higher frequency regimes. This elevated high-frequency content can cause circulating currents to flow in unintended grounding paths. These conducted emissions are part of a broader concern known as electromagnetic interference (EMI). The ability of a system to operate in the presence of EMI is a description of its electromagnetic compatibility (EMC). EMC defines the interaction of the system with its environment. With the progression of faster switching devices, EMI mitigation techniques have become necessary to minimize emissions and meet guidelines for EMC. The ability to model and understand this unwanted behavior is a powerful tool that can be used to mitigate the EMI for a given topology.

1.1. DC-DC Converter Topologies

The specific focus of this thesis is dc-dc converters and their EMI behavior. These converter topologies are utilized to scale across large voltage magnitudes, so high efficiency is generally a design requirement. The higher switching frequencies and faster edge rates made possible by WBG devices are essential to meeting these efficiency and power density requirements. Common examples of dc-dc converters are the buck and boost converter. Figure 1 shows canonical examples of these topologies. The two converter topologies are similar in design, but the buck converter converts the dc input to a lower voltage, while the boost converts the dc input to a higher voltage [1].

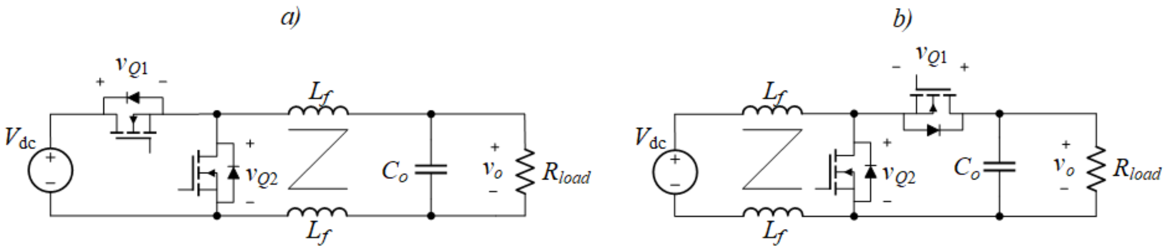

Figure 1. Canonical (a) buck and (b) boost converter

The primary operation of a dc-dc converter is to convert a dc input voltage into a dc output voltage that is attached to a load. To achieve this, switching devices are used to configure the system into two primary states. The "on" state describes the condition in which the output side of the circuit is connected to the input voltage, and the "off" state describes the condition in which the output side is disconnected from the source. This is demonstrated for a canonical buck converter in Figure 2. Figure 2 (a) shows the conduction path in the "on" state and Figure 2 (b) shows the conduction path of the "off" state. The switching devices are gated "on" and "off" to create a square waveform, and the duty cycle parameter determines how long the system is kept in each switching state. The duty cycle ranges from zero to one. A duty cycle of zero indicates that the system is always in the "off" state. A duty cycle of one indicates that the system is always in the "on" state. This switch voltage is then filtered to produce a dc output voltage that is applied to the load. The two switching devices are labelled as Q_1 for the upper switch and Q_2 for the lower switch. For a buck converter, the lower switch is not a necessary control variable. Instead, a diode is often used to allow the circuit to conduct in the "off" state. When Q_1 is on, the input and output are connected (Figure 2(a)). When Q_1 is off, Q_2 is on, which allows the circuit to conduct on the output side (Figure 2(b)).

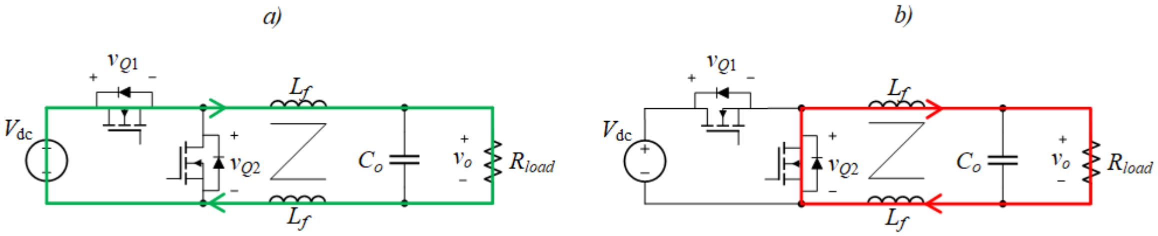

Figure 2. Current flow in a canonical buck converter for an (a) on and (b) off state

The buck converter takes advantage of filtering devices to smooth the action of the switching devices and produce a dc output. The filtering function required for buck and boost converters is realized with an inductor and a capacitor. The canonical configuration of these topologies utilizes one filter inductor in the upper rail of the output. However, the system in Figure 1 shows a generalized setup with two inductors on the converter output. The filter inductor acts as a smoothing device to stabilize the current pulses generated by the switching devices turning on/off, and it stores energy in the magnetic field. The filter capacitor is in parallel with the load so that it can smooth the output voltage of the system, and it stores energy in the electric field. The filter components act together to create a cutoff frequency that is less than the switching frequency so that the switching behavior is properly filtered from the output voltage [1]. A perfect design is able to generate a pure dc output voltage. Practical examples define a tolerance for an acceptable ac ripple voltage across the load. The filtering components are designed so that the ac component of the output voltage is minimized. The final result for these converter topologies is an output voltage that is predominantly dc but contains a small ac ripple component.

1.2. Why EMC is important

The converter topologies of dc-dc converters are used in a wide variety of applications, and the need for the converters to be more efficient and power dense has led to elevated EMI signatures. These elevated EMI profiles are caused by the use of increased switching frequencies and faster rise/fall times. These fast transitions cause elevated EMI signatures due to the increased spectral content of switching waveforms in the high-frequency regime.

To analyze the frequency spectrum of switching waveforms, the use of a Fourier series is beneficial. Fourier series analysis transforms time-domain signals into their frequency domain equivalents, also known as their spectrum [3]. This analysis identifies the magnitudes of the different frequency components that would otherwise be combined together in a time domain waveform. For dc-dc converters, the waveforms of interest are fundamentally square or trapezoidal waves. An ideal switch will demonstrate instantaneous rise/fall times. Realistic switching waveforms demonstrate finite rise/fall times. Thus, practical switching waveforms are trapezoidal in nature. When describing trapezoidal and square waveforms, it can be shown that their spectra are a function of the switching frequency and associated harmonics [4]. Figure 3 shows a square wave and a trapezoidal wave in the time domain along with the equivalent spectrum of each waveform determined by Fourier series analysis in the frequency domain. A triangular waveform is also included as a point of comparison.

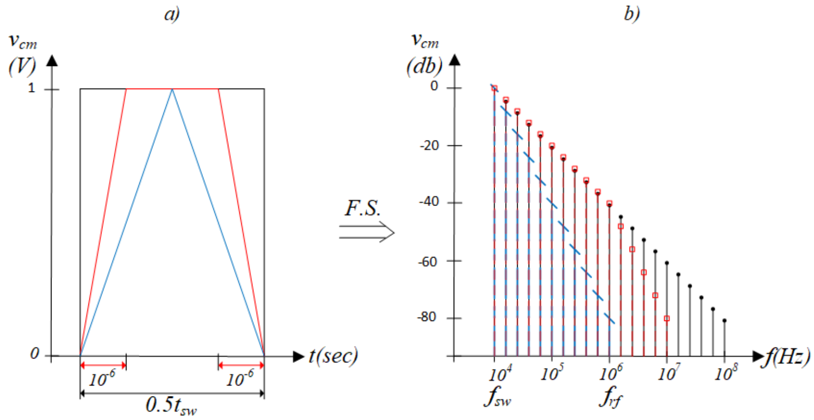

Figure 3. Spectral representation of a square, trapezoidal, and triangular wave time domain signal

Figure 3 demonstrates that a square waveform contains additional high frequency content compared to a trapezoidal waveform and a triangular waveform. The figure shows that the magnitudes of the waveforms are all the same at the switching frequency. The primary difference between the square and trapezoidal waveform spectra is dependent on the effect of the rise/fall time. The square waveform decreases by 20dB in magnitude per decade across the frequency spectrum. On the other hand, while the trapezoidal waveform spectrum does initially decrease by 20dB in magnitude per decade, it has an additional inflection point related to the rise/fall time. At this inflection point, the magnitude of the trapezoidal wave spectrum falls at 40dB per decade. To clarify the difference in magnitude between these cases, Figure 4 shows the normalized spectral envelopes for the waveforms operating at a switching frequency of f_{sw} over 4 decades of frequency. Figure 4 shows that the square waveform has a more significant magnitude at high frequency compared to the trapezoidal waveform.

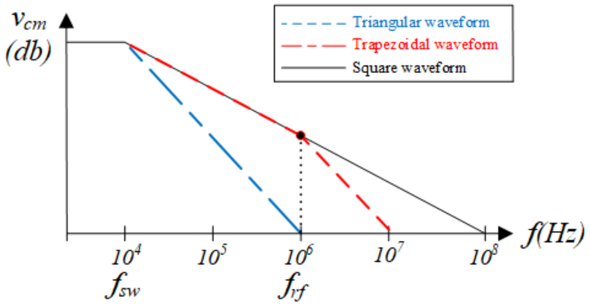

Figure 4. Spectral comparison of square, trapezoidal, and triangular waveforms

This elevated magnitude at high frequencies is a fundamental reason why conducted emissions propagate through unintended grounding paths in dc-dc converters. Unintended coupling paths are normally capacitive in nature. The frequency-domain impedance of capacitors falls off at a rate of 20 dB per decade with increasing frequency [1]. Thus, these paths become low-impedance at high frequency. Applications utilizing WBG devices introduce significant spectral content in frequency regimes for which these capacitive couplings become a favorable path for current to flow.

1.3. Need for Modeling EMI

The increased emissions for systems utilizing WBG devices demand proper understanding. If a system can be modeled for this behavior, effective measures for mitigation can be designed accordingly. The area of study that encompasses this modeling technique is related to common-mode (CM) analysis. A generalized decomposition technique is leveraged in this thesis to describe the emissions profiles for the systems of interest. This method is concerned with decomposing the mixed-mode (MM) behavior for a system into the differential-mode (DM) and the CM behavior. The MM behavior represents of the total behavior of the system; the DM behavior represents what is normally the intended behavior of the system; and the CM behavior represents what is normally unintended behavior.

The decomposition technique provides a means to deterministically isolate the CM behavior from the MM representation of the system. The resulting models are called common-mode equivalent models (CEMs). MM models carry the burden of the entire behavior of the system, and thus it can be difficult to infer CM behavior from such models. On the other hand, CEMs allow the CM behavior of the system to be isolated from the DM behavior. This representation enables a designer to identify degrees of freedom within the system that can be leveraged to reduce EMI. Commercial products generally have to meet a certain requirement for conducted emissions that are derived from larger system-level requirements. An example of a conducted emissions limit line is shown in Figure 5 for MIL-STD-461 CE102 [5]. In practice, commercial applications generally apply filtering components such as CM chokes to the system in an attempt to attain compliance with emissions standards. The approach taken in this thesis is to understand the CM behavior of the system at a more fundamental level so that emissions can be minimized without negatively affecting system performance. Using CEMs, solutions can be incorporated much earlier in the design process to mitigate EMI sources and improve the EMC of the system. This heightened understanding of the driving emission sources and circuit elements that are present in the CM behavior of the system is expected to lead to a more efficient design process that can improve EMC.

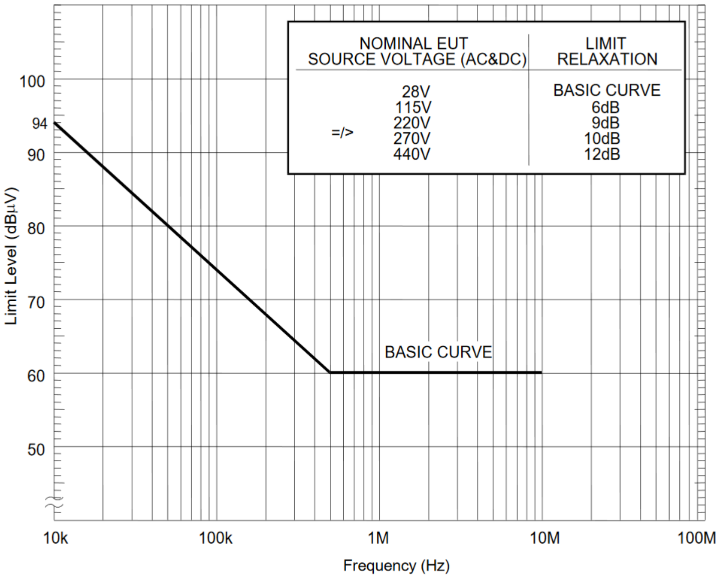

Figure 5. Example of limit line for conducted emissions [5]

1.4. Thesis Overview

Due to the inherent tradeoff between high efficiency and elevated emissions, a more fundamental understanding of CM behavior is needed. This thesis uses a generalized decomposition technique to describe buck and boost converters for both simplified and practical implementations of these topologies. The decomposed MM models are represented as CEMs and subsequently analyzed to reveal the impact of filter inductor asymmetry on emissions. A case study is then conducted utilizing the buck topology and a two-phase experimental procedure. In the first phase, the simplified buck CEM is empirically validated using a low-power experimental setup. In the second phase, the practical buck CEM is empirically validated using a high-power experimental setup.

This thesis is organized as follows. Chapter 2 identifies literature that has examined modeling of EMI, both in the form of detailed MM models and CEMs. This literature review provides insight into modeling of inverters and dc-dc converters, with a particular focus on dc-dc converters. Chapter 3 establishes the methodology for developing CEMs using the generalized decomposition technique. The buck and boost converters are decomposed into their CEMs for the simplified and practical models. Chapter 4 leverages these CEMs to provide analysis regarding the influence of the filter inductor asymmetry for both topologies. Chapter 5 provides empirical validation of both the simplified and practical buck converter CEMs. Finally, Chapter 6 concludes the thesis and describes future work.

CHAPTER 2:

LITERATURE REVIEW

The literature focused on power electronic converters is dense, so this thesis reviews both inverters and dc-dc converters, with a specific focus on dc-dc converters. Between these two topologies, inverters have been treated with more detail in the literature in reference to explanations of CM noise paths and mitigation techniques. Both of these topologies are centered on one of two philosophies for modeling EMI. The first approach involves development of a detailed MM model by means of fully characterizing the components and propagation paths of a system. The second approach is focused on understanding the CM behavior of the larger system through modeling. The following subsections analyze the literature surrounding inverters and dc-dc converters with respect to the identification and modeling of EMI.

2.1. Inverters

The literature describing CM behavior is much more developed for inverters than for dc-dc converters. The literature surrounding inverters is quite developed both for the detailed MM analysis approach and for derived CM model approach. This diversity and years of development for inverters separates the treatment of this topology from the treatment of dc-dc converters.

2.1.1. Detailed MM Modeling

The first subset of literature for inverters is concerned with creating a detailed MM model of a given system to reveal the underlying EMI behavior. The general approach involves characterization of the filter components and parasitic paths in a highly detailed fashion [6]-[8]. For example, Koyama et al. investigate the variety of propagation paths in a fully populated inverter-driven air conditioner system in order to generate a detailed MM model. This model is then leveraged to understand and mitigate unwanted CM noise [6]. Muetze et al. utilize a similar approach to understanding the role of motor bearings in coupling CM noise into the larger system [7]. Julian et al. investigate the use of modulation strategies on a MM model in order to eliminate CM noise sources [8].

2.1.2. CM Modeling

The literature surrounding inverters also contains a large subset of papers that investigate the CM behavior of a system through the development of equivalent CM models. In some cases, the CM models are developed directly from an understanding of the topology [9],[10]. For example, Chen et al. investigate the flow of CM currents through a three-phase inverter via the motor bearings and parasitic capacitances. A detailed analysis is performed to inform a CM model that attempts to explain the primary coupling path [9]. Mastuhisa et al. investigate CM noise sources and propagation paths for a system without an AC utility line grounding connection. Their approach is to develop an equivalent CM model to inform an approach for designed a new filter that could replace a common EMI filter [10]. Another subset of the literature on CM modeling combines thorough characterization of components in the physical system with systematic modeling of the CM behavior. This approach generates detailed CM models with increased precision and accuracy [11],[12]. For example, Ogasawara et al. perform a detailed characterization of an RLC resonant circuit to inform an equivalent CM model that explains how a CM transformer can reduce leakage current in lieu of a common CM choke [11]. Busse et al. perform a detailed characterization of bearings to derive a detailed CM model that explains the interactions between the CM noise sources and the bearings in PWM drives [12].

2.2. DC-DC Converters

EMI noise characterization in dc-dc converters has received less treatment in the literature than inverters. However, the available literature can be categorized into papers that focus on detailed MM models and papers that focus on the development of equivalent CM models. Much of the focus is specifically on the boost converter topology [13]-[16],[18]-[20]. Most of the analysis for boost converters is based on a "general balancing technique" that seeks to create symmetry within the system in order to mitigate EMI profiles [13]-[15],[17],[19],[20]. This technique proliferates for this converter topology and is the prevailing approach for reducing the CM noise for these systems. On the other hand, very few papers are dedicated to describing the EMI characteristics of buck converters [17],[22]. The analysis presented in Brovont et al. provides foundational work utilized in this thesis [22]. The systematic approach utilized to construct the CM model as well as the analysis techniques presented therein are leveraged and developed throughout this thesis for both the buck and boost converter topologies.

2.2.1. Detailed MM Modeling

The first of the two major categories that define the field of EMI noise reduction for dc-dc converters is concerned with detailed MM modeling. This modeling is based on detailed characterization of the circuit elements in the physical system in order to simulate the emissions behavior. Leveraging an understanding of the system component values and parasitic paths, these papers advocate for the use of best practices to mitigate CM noise. The "general balancing technique" is dominant in this type of modeling, specifically as a concept to explain why EMI in the system is reduced. For example, Shoyama et al. investigate the CM noise reduction that results from balancing the circuit elements in a boost converter [14]. These authors develop a detailed MM model to inform "intuitive" CM noise flow in the system under study. Xin et al. investigate the “general balancing technique” of a boost converter in more detail [15]. This paper extends the previous research concerning the balancing technique and seeks to balance all appropriate components affecting CM behavior. Specifically, this paper analyzes the relationship between balancing the CM current through the power module parasitics, the total CM impedance of the system, and the CM noise sources to reduce emissions.

There is a smaller subsection of literature concerned with MM modeling that looks less at balancing the system, but rather at the individual components that are designated as having the largest effect on EMI behavior. Nomura et al. investigate the effect of a coupled inductor in reducing CM noise in a boost converter [18]. Specifically, this paper provides a detailed analysis of different filter inductor configurations with emphasis on a coupled inductor to show the benefit of the technique for CM noise reduction. Boyer et al. provide a general approach to identify the main EMI sources within the components on a printed circuit board [21]. Rockhill et al. investigate the application of techniques found in the literature concerning boost converters to buck converters, with the goal of actively cancelling out CM noise sources in the system [17]. This is one of the few papers within this subsection that addresses the behavior of a buck converter instead of a boost converter. This paper relies on the common techniques used to analyze boost converters. This paper achieves CM noise reduction by specifically adding an additional switching device in the lower rail of the system that acts as an equal and opposite CM noise source to reduce the total EMI in the system. The system derived in [17] does balance the filter inductors but makes no specific reference to the “general balancing technique”.

2.2.2. CEM Modeling

The second of the two major categories that define the field of EMI noise reduction for dc-dc converters is centered on developing CM models that identify noise sources and impedances that dominate CM behavior. Papers within this subset of literature vary on how generalized the process used is with reference to the construction of an equivalent CM model. However, all of the identified papers attempt to capture the CM behavior of the larger system in an equivalent CM model. There currently exists very little treatment for the buck converter in the literature on CM emissions [17], [22]. Within this subset, Brovont et al. provides foundational work for this converter topology that this thesis leverages [22]. Additionally, this paper provides motivation for the analysis presented herein. This work identifies the influence of filter inductor asymmetry on the buck converter with respect to minimizing EMI signatures. Specifically, the unexpected benefit associated with asymmetric filter inductors for reducing the CM emissions of the buck topology is identified in [22]. The systematic method employed in [23] to decompose the proposed MM model into its CEM is leveraged in this thesis to decompose models for both converter topologies. The techniques used to analyze the subsequent CEM and highlight influential noise sources are also leveraged herein for both the buck converter and the boost converter to generalize the effect of filter inductor asymmetry.

The literature surrounding the boost converter focuses on the “general balancing technique”. For example, Wang et al. develop a CEM by identifying the specific circuit elements within a PFC boost converter that contribute to the overall CM noise [13]. This paper performs a thorough analysis of the CM behavior for a boost converter by analyzing different sections of the circuit individually and then combining those discrete circuits together into a singular CEM. This technique is then used to identify CM noise reduction techniques that result from balancing the ratio of filter inductors and parasitic capacitances within the system. Kong et al. build on [13] in an attempt to derive a more symmetric topology for the boost converter in order to further reduce CM noise [19]. This paper extends the “general balancing technique” that is used in the dominant part of the literature. This is done in an attempt to create a CEM to help identify CM noise reduction techniques that arise as a function of the symmetry of the system.

Other papers take a more general approach to identifying the CM behavior of the system without direct reliance on the “general balancing technique”. For example, Xin et al. investigate the use of symmetry and a CEM not only to understand the CM noise sources, but also to reduce the total emissions in the system [20]. This paper analyzes the relationship between reduced CM current and the balancing of power module parasitic capacitances. This paper also introduces the use of an anti-phase transformer in the place of a typical filter inductor to actively cancel out CM noise in the system. Yang et al. describe a detailed approach to characterizing the components of a system to directly inform development of a CM model that attempts to predict CM noise [16]. This paper differs slightly from the balance of the literature concerned with CM modeling by providing a detailed characterization of individual components. The detailed characterization is then applied to produce an equivalent CM model to achieve agreement with the experimentally observed EMI in the system. This subset of literature identifies the relationship between EMI mitigation and symmetry for a boost converter, while not being over-reliant on the balancing technique to explain the fundamental behavior of the overall system.

CHAPTER 3:

CM DERIVATION OF GENERALIZED BUCK/BOOST TOPOLOGY

In order to further understand the CM behavior of the buck and boost converters, it is necessary to define a modeling technique that decomposes a given circuit's MM quantities into its CM equivalent relationships. The generalized modeling technique described herein is developed out of [23]. When applied correctly, the technique derived in [23] produces a CEM that extracts the dominant CM behavior from a detailed MM model of a given system. The process requires detailing a MM model of the circuit under consideration, and then partitioning the components in the MM model about the active devices, which are normally the switching devices for dc-dc converters. With this partitioning, the decomposition technique can be performed about an arbitrary reference point identified for each individual section of the MM model. Finally, the completed CEM is constructed by connecting all of the sections together at specified reference points or nodes from the MM model. These reference points associate the CM voltage terms to sources that exist in the MM model. Due to the complexity of the decomposition process, it is often beneficial to start by defining the simplest MM model that is believed to capture all circuit elements relevant to the CM behavior of the system. After decomposing the simple MM model, iteratively applying this method with additional complexity usually leads to a final CEM that contains the necessary components to provide appreciable agreement with the CM behavior of the physical system. The CEM decomposed in this chapter will follow this method rigorously and this treatment will constitute a building block for the analysis that will be performed in later chapters.

3.1. Method for Deriving CEM

Developing a CEM for a given system is extremely challenging without a definitive process. In this chapter, a rigorous and generalized method for deriving a CEM is described. This method helps facilitate an understanding of the fundamental CM behavior of the system under consideration. The decomposition process is defined explicitly by the following four steps: (1) clearly define and setup a detailed MM model; (2) configure the MM model around the dominant emissions sources of the system, which are generally the switching devices; (3) individually decompose the sections of the MM model into their equivalent representations using the analysis in [23]; and (4) combine all of the equivalent representations into a unified CEM with the aid of specific reference points or nodes from the MM model. With this process, it is possible to decompose MM models for the buck and boost converters into their respective CEMs.

3.1.1. Creation of Detailed MM Model

The first step in the process is to generate a schematic representation of the system that is being decomposed. Initially, the MM model should include the designed circuit components and only that subset of parasitic elements that is known to significantly influence the CM behavior of the system. Keeping the parasitic model simple in the initial MM model provides a starting point that streamlines the initial analysis. Generally, this initial model will be too simple to completely describe the CM behavior of the system under analysis. Therefore, an iterative process is subsequently utilized to add layers of complexity to the MM model such that the final CEM provides a suitable representation of the CM behavior of the system under study. This iterative process avoids the difficulty associated with deriving a CEM based on a very complex parasitic model of the system, many aspects of which are not needed to explain its CM behavior. This iterative approach aids in discovering which parasitic elements are necessary for explaining the CM behavior of the system under consideration.

3.1.2. Partitioning MM Model around Switching Devices

The second step in the method is to partition the MM model around the switching devices. This step facilitates subsequent analysis by breaking the overall system into more manageable sections, each of which can be treated independently. When implementing this decomposition technique in reference to power electronic systems, it is often beneficial to partition the MM model about the switching devices. For the analysis of buck and boost converters in this thesis, the switching devices are the primary active devices in the system and thus represent natural locations for partitioning the MM model. To implement the partitioning, the switching devices are removed from the MM model, and critical voltages are defined based on the nodes within each section that are adjacent to the former switch locations. The removal of the switching devices identifies the most critical location when specifying the specific reference nodes in the final step of the method. Simplification of the MM model by removing the switching elements helps identify the important nodes of interest and facilitates defining the voltage sources for the final CEM.

3.1.3. Decomposition of Individual Sections

The third step is concerned with decomposing each individual section of the MM model into its CM equivalent. In this context, a section is defined as a contiguous segment of the MM model that exclusively contains passive circuit elements. KVL is used as the primary circuit analysis technique to describe the MM behavior of the system during this portion of the analysis. In order to decompose the MM behavior of each section into its CM equivalent, definitions for voltage and current terms that represent linear transformation from MM quantities to associated CM and DM quantities are employed. Figure 6 shows the generalization for a two-line system that will act as a guiding example throughout this chapter. The definitions needed for DM and CM decomposition of the individual components for this two-line system are presented in Equations*(1)-(4)*.

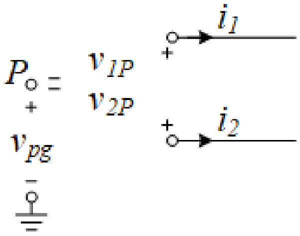

Figure 6. DM and CM definitions for a two-line system

$$\begin{bmatrix} v_{dm} \\ v_{cm} \end{bmatrix} = \begin{bmatrix} 1 & -1 \\ 1/2 & 1/2 \end{bmatrix} \begin{bmatrix} v_{1\mathrm{P}} \\ v_{2\mathrm{P}} \end{bmatrix} \tag{1}$$

$$\begin{bmatrix} i_{dm} \\ i_{cm} \end{bmatrix} = \begin{bmatrix} 1/2 & -1/2 \\ 1 & 1 \end{bmatrix} \begin{bmatrix} i_1 \\ i_2 \end{bmatrix} \tag{2}$$

$$T_v^2 = \begin{bmatrix} 1 & -1 \\ 1/2 & 1/2 \end{bmatrix} \tag{3}$$

$$T_i^2 = \begin{bmatrix} 1/2 & -1/2 \\ 1 & 1 \end{bmatrix} \tag{4}$$

The two transformation matrices T_v^2 and T_i^2 are used to facilitate the linear transformation from MM quantities into CM and DM equivalent quantities. These relationships are defined by the total number of lines in the system under study. By definition, differential mode quantities are specified between two pairs of lines. The common mode definition is generally defined by a singular definition representative of the total CM behavior of all lines in a given system. As an example, a four-line system can be described by three DM definitions, along with a single CM definition. However, the more lines in a given system, the more complex the analysis, and thus the more powerful the linear transformation technique. The four-line system example could be represented with three DM terms and one CM term as described previously. Alternatively, this system could be split into two subsections of the MM model; each subsection would be defined by two individual lines within the four-line system. In this formulation, each submatrix would include one DM term and one CM term.

This complexity is not necessary for the fundamental MM model that will be analyzed first in this chapter, so the definitions that will be used for the main part of this chapter are established in Equations *(1)-(4)*. The analysis technique used here is KVL, so the approached outlined in this thesis employs voltage definitions to generate the CEMs. The CM impedance of each considered component is defined by the constitutive laws of the given device as in traditional linear circuit analysis. The CM definitions in Equations *(1)-(4)* are then used to decompose these MM voltage definitions into their CM and DM equivalents.

3.1.4. Combination into a Final CEM

The final step in the decomposition method is combining the individual decomposed sections into a final CEM. This step requires explicitly defining the arbitrary reference points that relate each section to the MM model. These arbitrary points are normally labelled as P/P', and are defined in reference to a specific node in the MM model. The CM equivalent model of each section normally includes at least one CM voltage source. Combining two sections at a common reference point will put two similarly defined, but opposite in sign, voltage sources together in series. When this occurs, cancellation of the CM voltage sources leads to the construction of a simpler CEM. However, there are sections where this type of cancellation is not possible. This is generally where the dominant CM voltage sources arise. Setting the reference nodes for each CM model in a specific way helps simplify the final CEM. The decomposition in the following sections illustrates this principle.

3.2. CM Derivation of Simplified Buck and Boost Converter

In this section, the method described previously is utilized to derive CEMs for the particular converter topologies considered in this thesis: buck and boost converters. Here, the steps established are further detailed for both topologies in the order in which they were introduced. The description of each step includes the detail necessary to highlight the important aspects of the method for each topology. The final CEMs are used to understand the CM behavior of the buck and boost converters in their most "fundamental" configuration, and also in a more complex configuration that builds on these fundamental CEMs. The fundamental model is constructed and decomposed in Section 3.2 of this chapter, and the more complex model is constructed and decomposed in Section 3.3 of this chapter. Since the derivation is similar for both topologies in the fundamental configuration, both are considered together. The differences in the derivation of the two topologies are highlighted at the point of relevance within the decomposition procedure.

3.2.1. MM Model Construction

The first step in the CM analysis method is to construct the fundamental MM model of the system under study. Accordingly, MM models for the buck and boost converter topologies are presented in Figure 7(a) and Figure 7(b), respectively. The MM models are designed to mimic a conducted emissions compliance setup for the topologies highlighted. Therefore, in addition to the core components of these converters, the models include compliance elements labeled Line Impedance Stabilization Networks (LISNs). The LISNs in this figure are configured in accordance with MIL-STD 461 [5]. LISNs serve as a standard reference impedance that also provides the point of measurement in conducted emissions compliance testing. LISNs are bonded to a metallic ground plane that represents the conductive cabinet that is typically included for safety reasons in a fielded power electronics system. In Figure 7, this ground plane is labelled as the testbed ground.

The capacitors on the output of the MM model connecting from the resistive load to the testbed ground also represent an important feature of a fielded system that is not an intentional part of the converter design. These parasitic couplings can arise from the proximity between conductive structures within the converter and the enclosing cabinet. Such couplings can also arise due to the presence of a heat exchanger that may be needed to maintain thermal stability of the converter or load. The LISNs and output capacitance add complexity to the fundamental model, but these elements are necessary to include in the MM model. These elements are included because they commonly exist in fielded systems, and they have a significant influence on the CM behavior of the topologies under consideration.

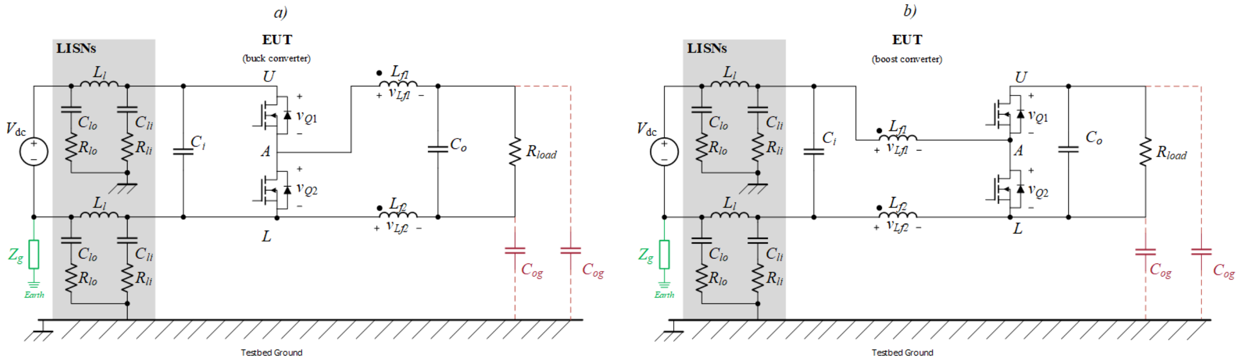

Figure 7. MM models for (a) buck and (b) boost converters

The filter inductors are another unique element of the system that require additional explanation. In a canonical configuration for a buck or boost converter, the filter inductance is only present in the upper rail. The decision to separate the inductance and include a portion of this inductance in both rails is made to generalize the model. This generalization allows a more robust understanding of CM behavior to be developed. In the literature, some treatments that analyze the CM behavior of dc-dc converters include balanced inductors in both rails [13]. Other treatments describe how mutually coupled inductors can be used to actively cancel CM current in the system [18]. The prevalence of this approach suggests that a general configuration for the filter inductors may be desirable for this analysis. The governing equation that establishes this configuration of the inductors in the MM model of both converters is given by Equation *(5)*:

$$\begin{bmatrix} v_{Lf1} \\ v_{Lf2} \end{bmatrix} = L_f \begin{bmatrix} 1+a & m \\ m & 1-a \end{bmatrix} \frac{\mathrm{d}}{\mathrm{dt}} \begin{bmatrix} i_1 \\ i_2 \end{bmatrix} \tag{5}$$

where a represents the asymmetry factor between the upper and lower rails, and m represents the amount of mutual coupling between L_{f1} and L_{f2}. The range of validity for these two coefficients are $a \epsilon [-1,1]$ and $m \epsilon (-1,1)$. The filter inductors are considered symmetric when $a = 0$, with the inductance equally "split" between the upper and lower rails. The filter inductors are considered asymmetric when $a = 1$, with the total inductance "lumped" only in the upper rail. It is also noted that $m = -1$ corresponds to an ideal coupled inductor that only influences the DM behavior of the circuit; while $m = 1$ corresponds to an ideal CM choke that only influences the CM behavior of the circuit. As will be shown later in this thesis, parametrizing the asymmetry and mutual coupling factors for the filter inductors introduces an important element of flexibility into the CM decomposition. These two factors will play a dominant role in determining the CM behavior of the larger system and can also be leveraged to minimize emissions.

3.2.2. Partitioning around Switching Devices

The second step in the CM analysis method is to partition the system about the switching devices. Updated MM models that omit the switching devices and define the necessary voltages for the CM derivation are shown in Figure 8(a) and Figure 8(b) for the buck and boost converters, respectively. This formulation focuses on the dominant behavior that will define the CEM in terms of voltage sources. It also highlights which impedances remain in model and will be present in the CEM. Configuring the MM model in this way also facilitates a preliminary identification of suitable reference points. In the next section, these reference points are utilized for the derivation of the CM behavior of each component. The voltages about the switching devices highlighted in

Figure 8 are v_{AP}, v_{UP}, v_{LP}, and v_{NP}. The subscripts on these voltages indicate the nodes U, L, A, and N that the voltages are defined by with reference to the arbitrary node P. The A and N nodes are connected to the filter inductors for both the buck and boost converters in order to identify the AC-side behavior throughout the analysis. In contrast, the U and L nodes are connected to the side of the switching cell that is dominated by DC behavior.

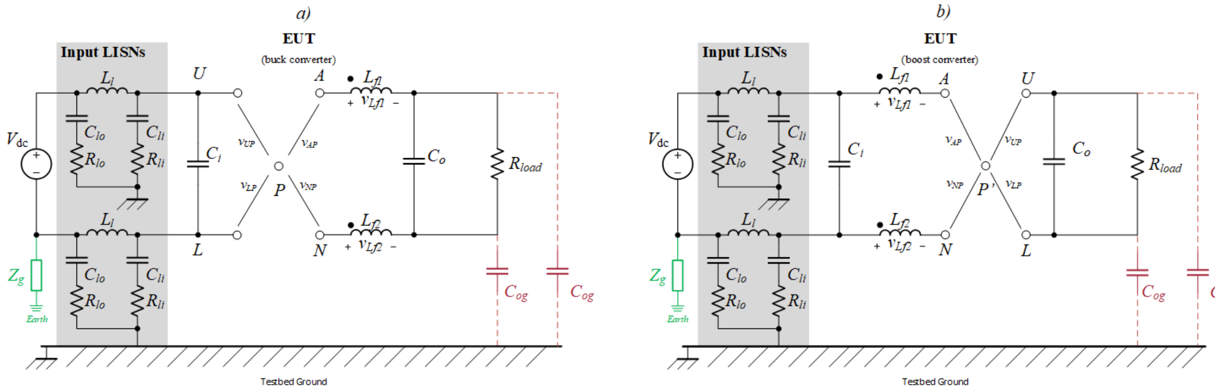

Figure 8. Original MM models oriented about switching devices for (a) buck and (b) boost converters

3.2.3. Component Decomposition

The third step in the CM analysis method is to decompose each section of the MM model into its CM equivalent representation. For this step, the behavior of interest is organized by analysis of the following sections: the LISNs, the filter inductors, and the parasitic capacitances at the load. These three sections are treated with the CM definitions established in the previous section in order to derive the associated CM behavior. Decomposition of the LISNs and load capacitances is straightforward because these sections are a combination of passive components. On the other hand, decomposition of the filter inductors is more complex, because they are closer to the switching devices and more variate by the definition given by Equation *(5)*.

3.2.3.1. CM Decomposition of LISNs

The first analysis in the decomposition is finding the CM equivalent representation of the LISNs. The MM model representation for the LISNs is shown in Figure 9(a). As stated previously, the specific configuration for the LISNs used in this work is detailed by MIL-STD-461 CE 102 [5]. The LISNs are treated as an individual section, so the right side of the model shown in Figure 9(a) is referred to an arbitrary reference point P. This reference point is used as a placeholder to complete the KVL loop. This reference point will be linked to the MM model to form the complete CEM once each section is decomposed.

It is noted that the input capacitance, C_i, defined in Figure 7 is not considered in this decomposition. The reason is that this capacitor does not provide a CM current path since it appears between the upper and lower rails. Also, due to the complexity of the LISN configuration, it is advantageous to consider all of the LISN passive elements as a lumped, equivalent impedance. Such a simplified MM model for the LISNs can be created by viewing the input impedance of the LISN from the converter side, with V_{dc} disconnected. This simplification of the LISN impedance network is shown in Figure 9(b). With this configuration, it is much easier to observe the MM elements that are of interest for the decomposition process. The equation used to describe the single impedance for the LISNs is given by Equation *(6)*:

$$Z_{LISN} = \frac{(Z_{Cli} + Z_{Rli})(Z_{Clo} + Z_{Ll} + Z_{Rli})}{Z_{Cli} + Z_{Rli} + Z_{Clo} + Z_{Ll} + Z_{Rli}} \tag{6}$$

where each impedance is governed by the frequency domain representation of the passive element indicated by the subscript.

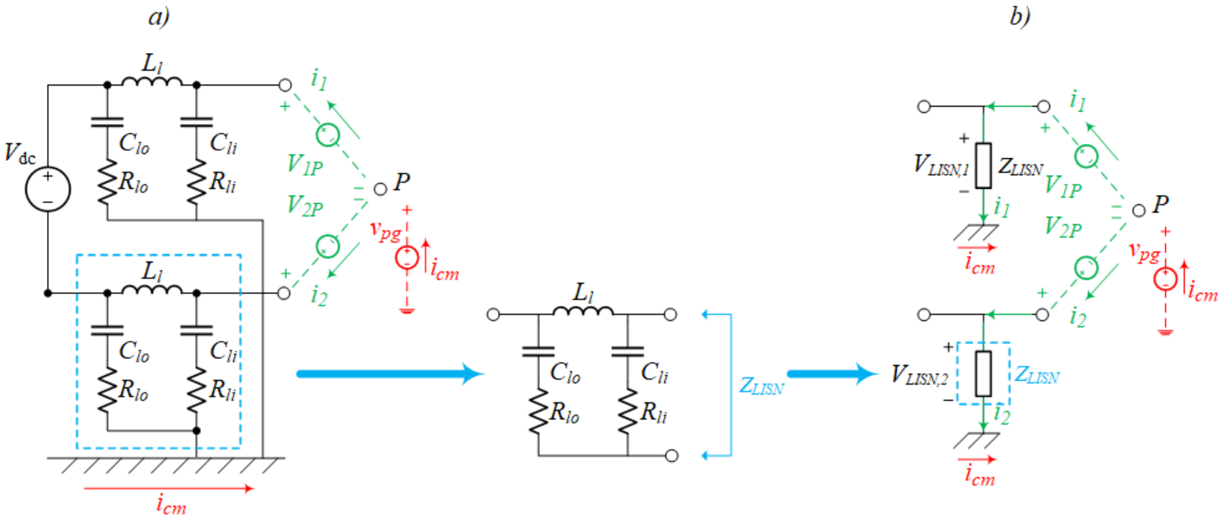

Figure 9. (a) Detailed and (b) simplified MM models for LISNs

Throughout the following analysis, the decomposition takes advantage of a list of elements of the MM model and transforms these elements into DM and CM relationships. The elements that are defined for the DM and CM behavior can be difficult to differentiate from the elements that define the MM behavior. Accordingly, Table 1 enumerates the elements that are highlighted in the following analysis, along with a designation of the behavior associated with each (MM, CM, DM).

TABLE 1
LIST OF ELEMENTS USED IN LISN DECOMPOSITION

Elements	Description	Behavior
v_{1P}, v_{2P}, v_{pg}	Path Dependent Voltages	MM
i_1, i_2	LISN Input Currents	MM
$v_{LISN,1}, v_{LISN,2}$	LISN Voltages	MM
v_{dm}, i_{dm}	DM Elements	DM
v_{cm}, i_{cm}	CM Elements	CM

Utilizing the model shown in Figure 9(b), the MM voltage across each of the LISNs is defined by Equation *(7)*:

$$\begin{bmatrix} v_{LISN,1} \\ v_{LISN,2} \end{bmatrix} = \begin{bmatrix} Z_{LISN} & 0 \\ 0 & Z_{LISN} \end{bmatrix} \begin{bmatrix} i_1 \\ i_2 \end{bmatrix} \tag{7}$$

With this definition, it is possible to resolve the CM equivalent relationship for this circuit. This is achieved by performing a KVL loop that starts at the reference point P, follows a path through the LISNs and returns through the testbed ground as indicated in Figure 9(b). This relationship is established in Equation *(8)*:

$$-v_{Pg}\begin{bmatrix}1\\1\end{bmatrix}-\begin{bmatrix}v_{1P}\\v_{2P}\end{bmatrix}+\begin{bmatrix}v_{LISN,1}\\v_{LISN,2}\end{bmatrix}=0 \tag{8}$$

Equation (*8*) establishes the MM KVL loop used to decompose the system into its DM and CM behavior. The detailed analysis for the LISNs is described in Section A.1 of the Appendix. The symmetric configuration for the LISNs decouples the DM and CM behavior for the system. Therefore, the CM KVL loop used to describe CM equivalent relationship for the LISNs is given in Equation *(9)*:

$$v_{Pg}=-v_{cm}+\frac{Z_{LISN}}{2}i_{cm} \tag{9}$$

Equation *(9)* describes the behavior for all elements that exist in the individual CM equivalent relationship. The relationship given by Equation *(9)* can be mapped to the CM equivalent circuit shown in Figure 10. From Equation *(1)*, the CM voltage is defined as $v_{cm}=\frac{1}{2}(v_{1P}+v_{2P})$. The node P will be explicitly defined when assembling the final CEM. Figure 10(a), shows the full CM equivalent model of the LISN section; while Figure 10(b) shows the reduced representation where the LISN impedance is represented as a single lumped element. The latter configuration is the preferred form for the following analysis and formulation of the complete CEM.

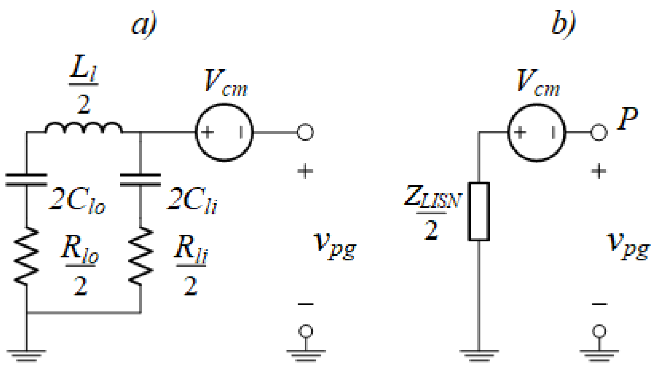

Figure 10. CEM with (a) detailed and (b) lumped impedance for the LISNs

3.2.3.2. CM Decomposition of Filter Inductors

The next section of interest within the MM model is the filter inductors. In this section, a variation arises between the buck and boost converter, but the analysis is similar enough that they are treated in the same fashion. The differences will be highlighted at the appropriate points in the decompensation process. The main difference arises from the orientation of the filter inductors with respect to the switching devices for each topology. However, this difference does not impact the MM model for the filter inductor section, which is shown in Figure 11. The components used in the decomposition of this section are enumerated in Table 2.

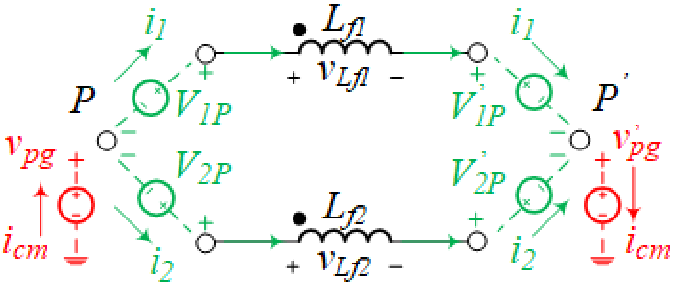

Figure 11. MM model for filter inductor configuration

TABLE 2

LIST OF ELEMENTS USED IN FILTER INDUCTOR DECOMPOSITION

Elements	Description	Behavior
v_{1P}, v_{2P}, v_{pg}	Path Dependent Voltages Referenced to Node P	MM
$v'_{1p}, v'_{2p}, v'_{pg}$	Path Dependent Voltages Referenced to Node P'	MM
i_1, i_2	Filter Inductor Currents	MM
v_{Lf1}, v_{Lf2}	Filter Inductor Voltages	MM
v_{dm}, i_{dm}	DM Elements	DM
v_{Q2}, v_{Co}, v_{Ci}	DM Voltages	DM
$v_{Lf,dm}$	DM Filter Inductor Voltage	DM
$v_{Lf,cm}$	CM Filter Inductor Voltage	CM
v_{cm}, i_{cm}	CM Elements	CM

Applying KVL to both branches within the MM model shown in Figure 11 produces Equation *(10)*:

$$-v_{Pg}\begin{bmatrix}1\\1\end{bmatrix}-\begin{bmatrix}v_{1P}\\v_{2P}\end{bmatrix}+\begin{bmatrix}v_{Lf1}\\v_{Lf2}\end{bmatrix}+\begin{bmatrix}v'_{1P}\\v'_{2P}\end{bmatrix}+v'_{Pg}\begin{bmatrix}1\\1\end{bmatrix}=0 \tag{10}$$

Equation (*10*) establishes the MM KVL loop used to decompose the system into its DM and CM behavior. The detailed CM decomposition analysis is described in Section A.2 of the Appendix. The asymmetry of the filter inductors causes both CM and DM behavior to appear in the CEM. The DM term indicates mode conversion that exists based on the asymmetry and mutual coupling of the filter inductors. CM KVL loop used to describe CM equivalent relationship for the filter inductors is given in Equation *(11)*:

$$v_{Pg}=-v_{cm}+\frac{L_f}{2}\frac{(1-a^2-m^2)}{1-m}pi_{cm}+\frac{a}{2(1-m)}v_{Lf,dm}+v'_{cm}+v'_{Pg} \tag{11}$$

Equation *(11)* describes the behavior for all elements that exist in the individual CM equivalent relationship. The relationship given by Equation *(11)* can be mapped to the CM equivalent circuit shown in Figure 12. The voltage source term v_{cm}^{dm} represents the mode conversion of the filter inductor asymmetry. It is noted that the reference points P/P' will be explicitly defined when assembling the final CEM. For completeness, each element represented in Figure 12 should be defined explicitly. The voltage source v_{cm} is described by Equation *(12)*:

$$v_{cm} = \frac{1}{2}(v_{1P} + v_{2P}) \tag{12}$$

The CM filter inductance, L_f^{cm}, is described by Equation *(13)*:

$$L_f^{cm} = \frac{L_f}{2}\frac{(1 - a^2 - m^2)}{1 - m} \tag{13}$$

The voltage source v'_{cm} is described by Equation *(14)*:

$$v'_{cm} = \frac{1}{2}(v'_{1P} + v'_{2P}) \tag{14}$$

The mode conversion term v_{cm}^{dm} is defined dependent on topology. The mode conversion equation for the buck converter is given by Equation *(15)*:

$$v_{cm}^{dm}(buck) = \frac{a}{2(1-m)} v_{Lf,dm,buck} = \frac{a}{2(1-m)}\left(v_{Q2} - v_{Co}\right) \tag{15}$$

The corresponding mode conversion equation for the boost converter is given by Equation *(16)*:

$$v_{cm}^{dm}(boost) = \frac{a}{2(1-m)} v_{Lf,dm,boost} = \frac{a}{2(1-m)}\left(v_{Ci} - v_{Q2}\right) \tag{16}$$

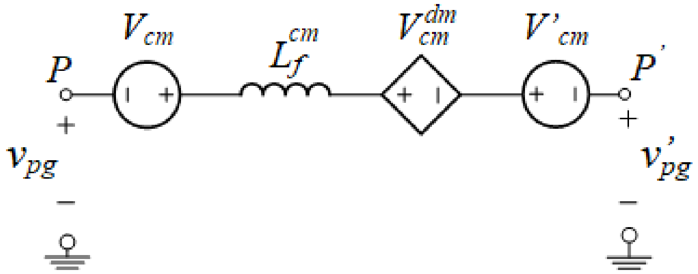

Figure 12. CEM for filter inductor configuration

3.2.3.3. CM Decomposition of Output Load Capacitances

The last section of the MM model requiring decomposition is the capacitive coupling of the output load. The section of the MM model in question is highlighted in Figure 13. Although not desired, coupling of the load to the ground network is usually present in fielded power electronic systems. This coupling arises due to proximity between converter elements and nearby conductive structures, such as the heat exchanger and converter enclosure, which are generally bonded to a system ground. It is noted that the output capacitance C_o is not included in this analysis because it does not influence the CM behavior of the system. The resistive load is neglected for the same reason. The components used in the decomposition of this section are enumerated in Table 3.

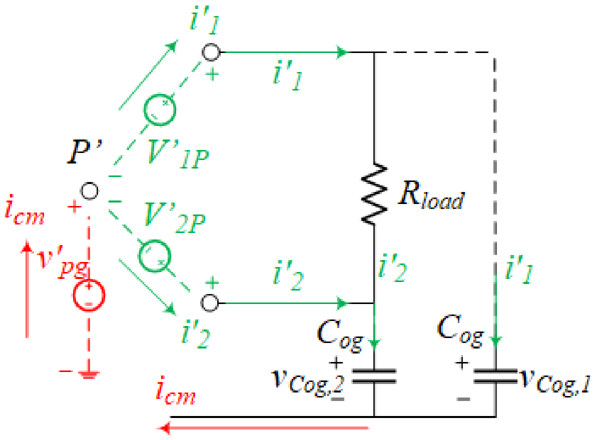

Figure 13. MM model for output capacitance

TABLE 3

LIST OF ELEMENTS USED IN OUTPUT CAPACITANCE DECOMPOSITION

Elements	Description	Behavior
$v'_{1P}, v'_{2P}, v'_{Pg}$	Path Dependent Voltages	MM
i'_1, i'_2	Load Capacitance Currents	MM
$v_{Cog,1}, v_{Cog,2}$	Load Capacitance Voltages	MM
v'_{dm}, i'_{dm}	DM Elements	DM
v'_{cm}, i'_{cm}	CM Elements	CM

Applying KVL to both branches within the MM model shown in Figure 13 produces Equation *(17)*:

$$-v'_{Pg}\begin{bmatrix}1\\1\end{bmatrix}-\begin{bmatrix}v'_{1P}\\v'_{2P}\end{bmatrix}+\begin{bmatrix}v_{Cog,1}\\v_{Cog,2}\end{bmatrix}=0 \tag{17}$$

Equation (*17*) establishes the MM KVL loop used to decompose the system into its DM and CM behavior. The detailed analysis is described in Section A.3 of the Appendix. The symmetric configuration for the capacitive coupling of the load decouples the DM and CM behavior for the system. Therefore, the CM KVL loop used to describe CM equivalent relationship for the capacitive coupling is given in Equation *(18)*:

$$v'_{Pg} = -v'_{cm} + \frac{1}{p2C_{og}} i'_{cm} \tag{18}$$

Equation (*18*) describes the behavior for the elements that exist in the individual CM equivalent relationship. The relationship given by Equation *(18)* can be mapped to the CM equivalent circuit shown in Figure 14. From Equation *(1)*, the CM voltage is defined as $v'_{cm} = \frac{1}{2}(v'_{1P} + v'_{2P})$. The node P' will be explicitly defined when assembling the final CEM. The two elements in the CEM include the voltage source v'_{cm} and the parallel combination of the two output capacitors.

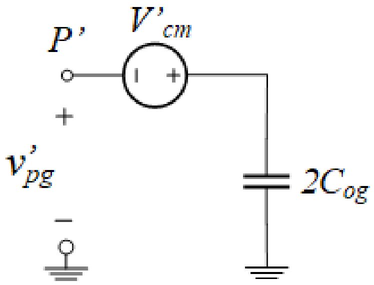

Figure 14. CEM for output capacitance

3.2.4. Final CEM Construction

The fourth and final step for the CM analysis method is concerned with combining all individual CEM sections into the final CEM. This CEM is produced by defining each of the individual CM equivalent relationships with respect to specific reference points for P and P'. Specifying the reference points allows the voltage sources to be explicitly defined by MM voltage sources. The reference points need not be defined at any specific node in the MM model, but some choices are better than others. For example, selection of certain reference points leads to cancellation of CM voltage sources, which produces a simpler model without loss of information. Due to the differences that arise when finalizing the CEMs, the buck and boost converters are analyzed separately in this section. The buck converter is resolved first, and the analysis is applied to the boost converter to identify and resolve the differences.

3.2.4.1. Buck Converter

The first step to resolve the final CEM for the buck converter is to specify the reference points to nodes in the MM model. This allows the CM voltage sources to be defined by MM sources. The model analyzed in this section is shown in Figure 15. The MM model is also included in this figure to highlight the MM elements used in the subsequent derivation. As a means to analyze the system in its totality, each of the individual CM voltage sources is given a unique name in the CEM shown in Figure 15. In addition, Table 4 provides a mapping of these unique names to the general names used in the previous sections. The CEM contains two reference points that need to be resolved: P and P'. The reference point P is defined at the switching devices, while P' is defined as the node that connects the filter inductors and the capacitive coupling at the load.

TABLE 4

LIST OF REDEFINED ELEMENTS FOR THE BUCK CONVERTER

Individual Section	Previously Defined	New Definition
LISNs	v_{cm}	v_{cm1}
Filter Inductors	v_{cm}	v_{cm2}
Filter Inductors	v'_{cm}	v_{cm3}
Output Capacitance	v'_{cm}	v_{cm4}

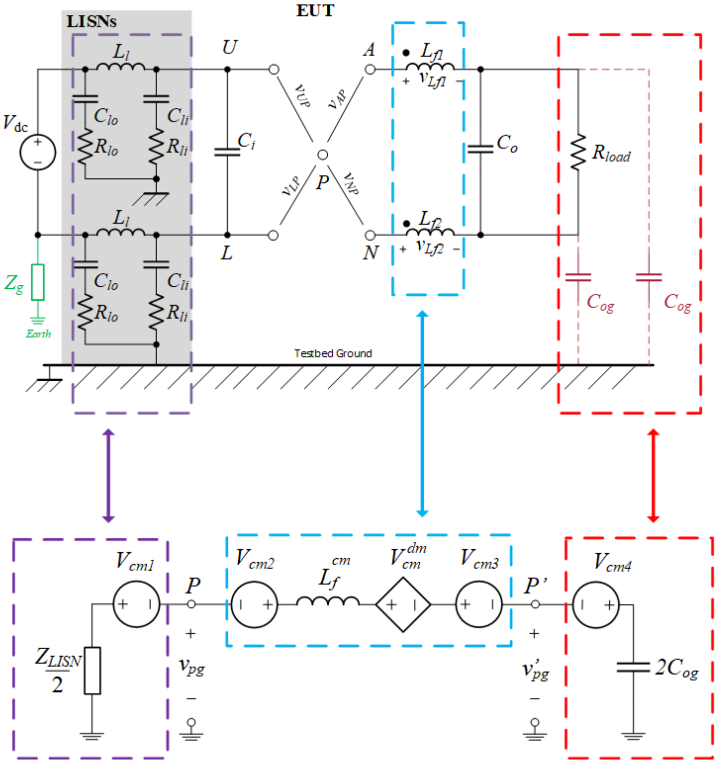

Figure 15. Initial CEM representation for the buck converter

Defining the reference points P/P' at specific nodes from the MM model facilitates the construction of the final CEM. The detailed analysis is performed in Section A.4 of the Appendix. The voltages v_{cm3} and v_{cm4} cancel each other out because they have the same magnitude and opposite signs. The voltages v_{cm1} and v_{cm2} persist and are defined relative to the MM node set for P. The reference point P is defined to the midpoint of the nodes U, L. This eliminates v_{cm1} from the CEM by its definition, and v_{cm2} is defined by Equation (*19*):

$$v_{cm2} = \frac{1}{2}\left(v_{Q2} - v_{Ci}\right) \tag{19}$$

Therefore, the total CM voltage source is defined by the series combination of v_{cm2} and v_{dm}^{cm}. Substituting the definitions for v_{dm}^{cm} and v_{cm2} given by Equations (*15*) and (*19*) respectively produces Equation (*20*):

$$v_{nom,1}^{cm} = \frac{1}{2}\left(v_{Q2} - v_{Ci}\right) - \frac{a}{2(1-m)}\left(v_{Q2} - v_{Co}\right) \tag{20}$$

Simplifying Equation (*20*) produces Equation (*21*).

$$v_{nom,1}^{cm} = \frac{1}{2}\left[v_{Q2} - \frac{a}{1-m}\left(v_{Q2} - v_{Co}\right) - v_{Ci}\right] \tag{21}$$

The final CM KVL loop that describes Figure 16 is shown in Equation (*22*):

$$v_{nom,1}^{cm} = \frac{Z_{LISN}}{2} i_{cm} + \frac{L_f}{2} \frac{(1 - a^2 - m^2)}{1-m} p i_{cm} + \frac{1}{p2C_{og}} i_{cm} \tag{22}$$

Equation (*22*) describes the behavior for the elements that exist in the fully formed CEM. The relationship given by Equation (*22*) can be mapped to the CM equivalent circuit shown in Figure 18. The LISN impedance is defined by Equation *(6)*; the filter inductors are defined by their frequency-domain representation with inductance equal to Equation *(13)*; and capacitive couplings of the load are defined by their frequency-domain representations with the magnitudes shown in Figure 16.

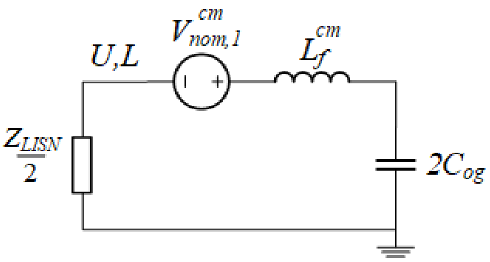

Figure 16. Final CEM for the fundamental model of the buck converter

3.2.4.2. Boost Converter

The analysis needed to derive final CEM for the fundamental model of the boost converter is contained in this section. The boost converter is similar in construction to the buck converter, so this analysis takes advantage of the analysis performed in 3.2.4.1. Figure 17 shows the MM model and CEM analyzed in this section. As shown in Figure 17, the main difference between the two topologies is where the switching devices are located. In the boost converter, the switching devices are located at P'; in the buck converter, the switching devices are located at P. Similar to the previous analysis, Figure 17 utilizes a unique name for each of the CM voltage sources present in the CEM. Table 5 provides a mapping of these unique names to the general names used in the previous sections of this thesis.

TABLE 5

LIST OF REDEFINED ELEMENTS FOR THE BOOST CONVERTER

Individual Section	Previously Defined	New Definition
LISNs	v_{cm}	v_{cm1}
Filter Inductors	v_{cm}	v_{cm2}
Filter Inductors	v'_{cm}	v_{cm3}
Output Capacitance	v'_{cm}	v_{cm4}

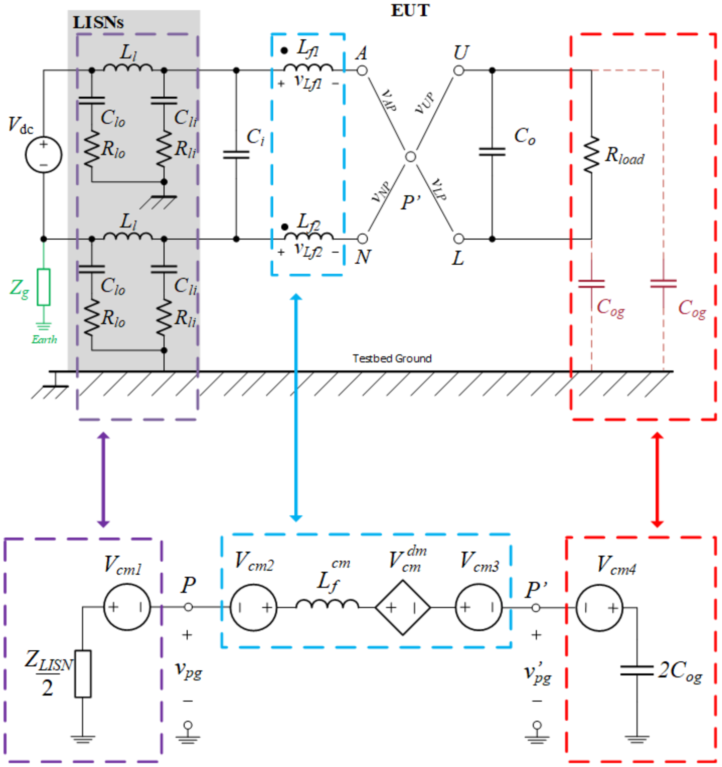

Figure 17. Initial CEM representation for the boost converter

Defining the reference points P/P' at specific nodes from the MM model facilitates the construction of the final CEM. The detailed analysis is performed in Section A.5 of the Appendix. The voltages v_{cm1} and v_{cm2} cancel each other out because they have the same magnitude and opposite signs. The voltages v_{cm3} and v_{cm4} persist due to their placement with respect to the switching devices. The reference point P is defined as the midpoint of the nodes U, L. This eliminates v_{cm4} from the CEM by its definition, and v_{cm3} is defined by Equation (*23*):

$$v_{cm3} = \frac{1}{2}\left(v_{Q2} - v_{Co}\right) \tag{23}$$

Therefore, the total CM voltage source is defined by the series combination of v_{cm3} and v_{dm}^{cm}. Substituting the definitions for v_{dm}^{cm} and v_{cm2} given by Equations (*16*) and (*23*) respectively produces Equation *(24)*:

$$v_{nom,2}^{cm} = \frac{a}{2(1-m)}\left(v_{Ci} - v_{Q2}\right) + \frac{1}{2}\left(v_{Q2} - v_{Co}\right) \tag{24}$$

Simplifying Equation (*24*) produces Equation *(25)*:

$$v_{nom,2}^{cm} = \frac{1}{2}\left[v_{Q2} - \frac{a}{1-m}\left(v_{Q2} - v_{Ci}\right) - v_{Co}\right] \tag{25}$$

The final CM KVL loop that describes Figure 16 is thus given by Equation *(26)*:

$$-v_{nom,2}^{cm} = \frac{Z_{LISN}}{2} i_{cm} + \frac{L_f}{2}\frac{(1 - a^2 - m^2)}{1-m} p i_{cm} + \frac{1}{p2C_{og}} i_{cm} \tag{26}$$

Equation (*26*) describes the behavior for the elements that exist in the fully formed CEM. The relationship given by Equation (*26*) can be mapped to the CM equivalent circuit shown in Figure 18. The LISN impedance is defined by Equation *(6)*; the filter inductors are defined by their frequency-domain representation with inductance equal to Equation *(13)*; and capacitive couplings of the load are defined by their frequency-domain representations with the magnitudes shown in Figure 18.

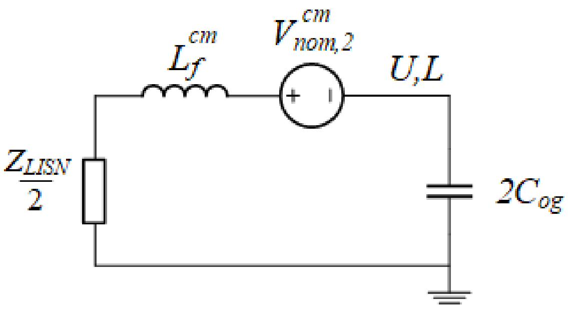

Figure 18. Final CEM for the boost converter

3.3. CM Derivation of Practical Buck and Boost Converter

The analysis in the previous section defines a fundamental description of the CM behavior of the buck and boost converter. However, there is often additional complexity in the MM model for a fielded system which dramatically affects the CM behavior. The complexity incorporated in the MM model arises from the packaging of the switching elements. This packaging usually takes the form multi-chip power modules (MCPMs) in converters that process more than a few kilowatts. Power modules are designed to provide thermal stability for the switching elements when operating at full-scale current and voltage levels for a given application. Due to the nature of the thermal interfaces within these structures, non-negligible parasitic couplings are formed between the switching elements and the module baseplate. Further treatment of the origin of these couplings can be found in [24]. For a traditional half-bridge power module, each of the three power terminals will be capacitively coupled to the baseplate of the module, which is bonded directly to the testbed ground for the buck and boost converters considered in this thesis. These capacitive couplings are referred to as baseplate capacitances (BPC). With the inclusion of the BPC, the CM modeling methodology established previously in this chapter can be re-applied to the buck and boost converters to construct CEMs that better represent the CM behavior of practical, fielded applications utilizing these topologies.

3.3.1. Updated MM Model

The first step in the CM analysis method is to establish new MM models that include BPC. The updated MM models are shown in Figure 19(a) and Figure 19(b) for the buck and boost converters, respectively. Inclusion of the parasitic capacitances attached to the switching devices is the only difference compared to the fundamental model shown in Figure 7(a) and Figure 7(b). Therefore, the analysis necessary to derive the CEM for the new MM model is nearly the same as that described in the previous section. The revised derivation will extend the previous analysis to include the impact of the new parasitic branch of the MM model. Three parasitic capacitances are included in the updated models: C_{ug} is the coupling of the upper node to the testbed ground; C_{ag} is the coupling of the phase node to the testbed ground; and C_{lg} is the coupling of the lower node to the testbed ground. An element labelled Z_h is also included in this model as a placeholder that represents the impedance between the baseplate and the testbed ground. Z_h may be negligible in some systems but is included here for completeness.

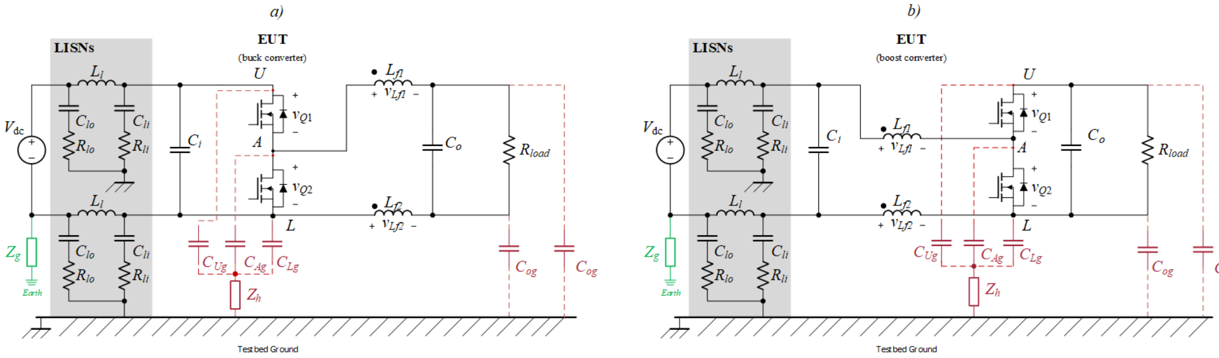

Figure 19. Updated MM model for (a) buck and (b) boost converter

3.3.2. Partitioning around Switching Devices

The second step in the CM analysis method is partitioning the updated MM model about the switching devices. Figure 20 presents the MM models for both the buck and boost converters with the switching devices removed and all appropriate voltages defined. Because the parasitic capacitances are attached directly to the switching devices, the associated voltage definitions are referenced directly to the testbed ground rather than to the arbitrary reference point P. The analysis in this section is focused on describing the attachment of these new branches to the larger CEM.

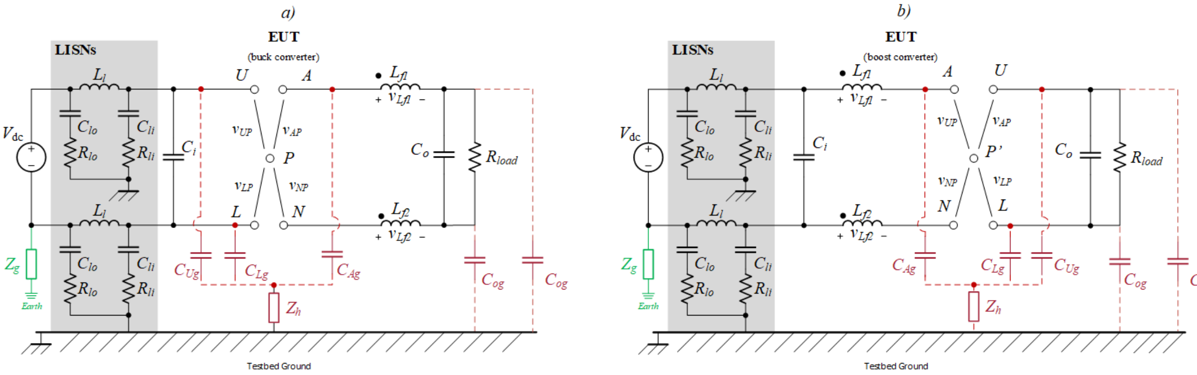

Figure 20. Updated MM model oriented about switching devices for (a) buck and (b) boost converter

3.3.3. Component Decomposition

The third step in the CM analysis method is decomposition of the individual sections of the MM model into their CM equivalents. The branch introduced by the BPC elements constitutes an independent section of the MM model. Therefore, the derivation for the LISNs, filter inductors, and output load capacitances do not change. Thus, the primary focus of this section is the decomposition of the new parasitic capacitance branch. However, it should be noted that the previous CM decomposition required DM and CM definitions only for a two-line system. The updated MM models include elements attached at all three terminals of the half-bridge. Therefore, the revised derivation presented in this section requires updated DM and CM definitions. Following the definitions given in [23], the generalized formulation for a three-line system provides two DM and one CM relationship. The resulting matrices are given by Equations *(27)*-*(30)*:

$$\begin{bmatrix} v_{UL,dm} \\ v_{LA,dm} \\ v_{cm} \end{bmatrix} = \begin{bmatrix} 1 & -1 & 0 \\ 0 & 1 & -1 \\ 1/3 & 1/3 & 1/3 \end{bmatrix} \begin{bmatrix} v_{UP} \\ v_{LP} \\ v_{AP} \end{bmatrix} \tag{27}$$

$$\begin{bmatrix} i_{UL,dm} \\ i_{LA,dm} \\ i_{cm} \end{bmatrix} = \begin{bmatrix} 1/2 & -1/2 & 0 \\ 0 & 1/2 & -1/2 \\ 1 & 1 & 1 \end{bmatrix} \begin{bmatrix} i_U \\ i_L \\ i_A \end{bmatrix} \tag{28}$$

$$T_v^3 = \begin{bmatrix} 1 & -1 & 0 \\ 0 & 1 & -1 \\ 1/3 & 1/3 & 1/3 \end{bmatrix} \tag{29}$$

$$T_i^3 = \begin{bmatrix} 1/2 & -1/2 & 0 \\ 0 & 1/2 & -1/2 \\ 1 & 1 & 1 \end{bmatrix} \tag{30}$$

Equations *(27)*-*(30)* specify the following relationships: a DM relationship between the U and L nodes; a DM relationships between the L and A nodes; and a CM relationship between all three nodes. These generalized definitions are a suitable formulation of the DM and CM relationships for three lines. However, this configuration leads to unnecessary complexity in the following analysis that can be readily avoided. Figure 21 suggests an alternative method to describe the DM and CM relationships for a three-line system in an analytically simpler formulation.

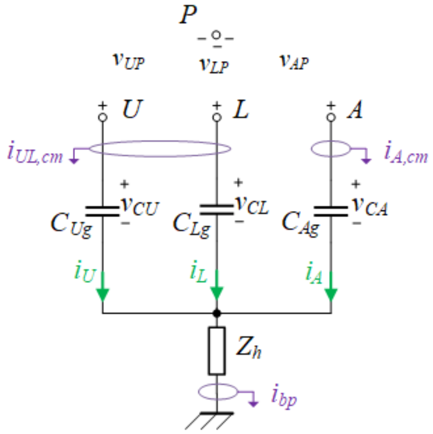

Figure 21. CM formulation with respect to the baseplate capacitance

In Figure 21, the total CM current, labelled i_{bp} is defined by Equation *(31)*:

$$i_{bp} = i_U + i_L + i_A \tag{31}$$

Equation *(31)* directly reflects the definition given in the bottom row of Equation *(28)*. Additionally, Figure 21 suggests that the system can be split into the CM behavior of the U/L branch and the behavior of the A branch. In this configuration, the total CM current i_{bp} can be described by Equation *(32)*:

$$i_{bp} = i_{CUL,cm} + i_{A,cm} \tag{32}$$

where $i_{CUL,cm} = i_U + i_L$ and $i_{A,cm} = i_A$. Thus, the definitions given by Equations *(27)-(30)* can be reconfigured to incorporate this division of CM current into two sections concerned with the behavior of $i_{CUL,cm}$ and $i_{A,cm}$. The newly formulated definitions are given by Equations *(33)-(36)*:

$$\begin{bmatrix} v_{UL,dm} \\ v_{UL,cm} \\ v_{A,cm} \end{bmatrix} = \begin{bmatrix} 1 & -1 & 0 \\ 1/2 & 1/2 & 0 \\ 0 & 0 & 1 \end{bmatrix} \begin{bmatrix} v_{UP} \\ v_{LP} \\ v_{AP} \end{bmatrix} \tag{33}$$

$$\begin{bmatrix} i_{UL,dm} \\ i_{UL,cm} \\ i_{A,cm} \end{bmatrix} = \begin{bmatrix} 1/2 & -1/2 & 0 \\ 1 & 1 & 0 \\ 0 & 0 & 1 \end{bmatrix} \begin{bmatrix} i_U \\ i_L \\ i_A \end{bmatrix} \tag{34}$$

$$T_v^3 = \begin{bmatrix} 1 & -1 & 0 \\ 1/2 & 1/2 & 0 \\ 0 & 0 & 1 \end{bmatrix} \tag{35}$$

$$T_i^3 = \begin{bmatrix} 1/2 & -1/2 & 0 \\ 1 & 1 & 0 \\ 0 & 0 & 1 \end{bmatrix} \tag{36}$$

Equations *(33)-(36)* define the three-line system such that the MM behavior is divided into both the DM and CM behavior of the U/L branch and only the CM behavior of the A branch. A similar approach is presented by Lemmon et al. for representing the baseplate capacitance of a half-bridge power module in [24]. Since the A branch does not have an apparent DM current path, as seen in Figure 20, the MM behavior of this branch is linked only to its CM behavior. Thus, the newly formed matrices describe one DM term and two CM terms. Since this thesis is focused on developing CEMs, this formulation does not lose any necessary information. The matrices given in Equations *(33)-(36)* can be thought of as containing two submatrices that describe independent behavior: the upper-left 2x2 matrix describes the DM and CM behavior of the U and L nodes; and the lower-right 1x1 matrix describes the CM behavior of only the A node. The other terms of the matrices are zero to indicate the independence between these two behaviors.

The power of this formulation is that it differentiates the AC-side and DC-side behavior for both converters. This segmentation of behavior was utilized previously in Section 3.2.2 of this thesis for the fundamental models. The terms $v_{UL,cm}$ and $i_{UL,cm}$ define the CM behavior of the U and L nodes around the switching devices. This formulation represents the DC-side behavior of the MM models. On the other hand, the terms $v_{A,cm}$ and $i_{A,cm}$ represent the AC-side behavior of the MM models. Therefore, the decomposition of the parasitic branch can be thought of in the same way as the fundamental analysis.

3.3.3.1. CM Decomposition of Parasitic Capacitances

The method defined in Section 3.1.3 is employed again here to decompose the section of the MM model concerned with the parasitic capacitances. The specific section of the MM model in question is highlighted in Figure 22. The KVL loop used to describe the DM and CM behavior of the section is established through the general impedance Z_h and the return voltage term v_{Pg}. The components used in the decomposition of this section are enumerated in Table 6.

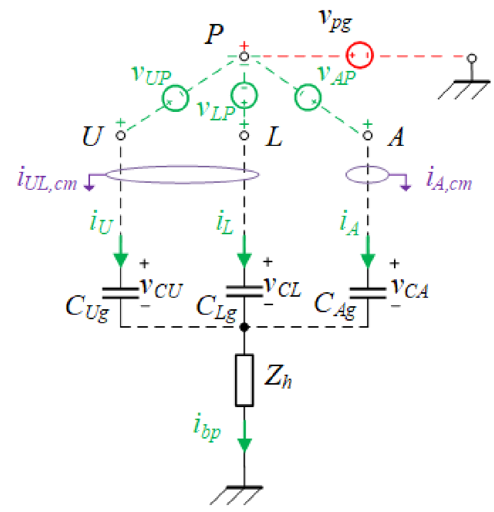

Figure 22. MM model for baseplate capacitance

TABLE 6

LIST OF ELEMENTS USED IN BPC DECOMPOSITION

Elements	Description	Behavior
$v_{UP}, v_{LP}, v_{AP}, v_{pg}$	Path Dependent Voltages	MM
i_U, i_L, i_A	Currents through BPC elements	MM
v_{CU}, v_{CL}, v_{CA}	BPC Voltages	MM
$v_{CUL,dm}, v_{UL,dm}, i_{UL,dm}$	U/L Node DM Elements	DM
$v_{CUL,cm}, v_{UL,cm}, i_{UL,cm}$	U/L Node CM Elements	CM
$v_{CA,cm}, v_{A,cm}, i_{A,cm}$	A Node CM Elements	CM

Applying KVL to Figure 22 produces Equation *(37)*:

$$-v_{Pg}\begin{bmatrix}1\\1\\1\end{bmatrix}-\begin{bmatrix}v_{UP}\\v_{LP}\\v_{AP}\end{bmatrix}+\begin{bmatrix}v_{CU}\\v_{CL}\\v_{CA}\end{bmatrix}+Z_h\begin{bmatrix}1&1&1\\1&1&1\\1&1&1\end{bmatrix}\begin{bmatrix}i_U\\i_L\\i_A\end{bmatrix}=0 \qquad (37)$$

Equation (*37*) establishes the MM KVL loop used to decompose the system into its DM and CM behavior. The detailed CM decomposition analysis is described in Section A.6 of the Appendix. The simplicity of the single line CM branch for the *A* branch provides a straightforward CM KVL loop given by Equation (*38*):

$$v_{Pg}=-v_{A,cm}+\frac{1}{pC_{Ag}}i_{A,cm}+Z_h\left(i_{UL,cm}+i_{A,cm}\right) \qquad (38)$$

The CM behavior for the U, L branch is governed by the interaction between each node, and the CM KVL is given by Equation (*39*):

$$v_{Pg} = -v_{UL,cm} + \frac{1}{p\left(C_{Ug} + C_{Lg}\right)} i_{CUL,cm} + \frac{C_{Lg} - C_{Ug}}{2\left(C_{Ug} + C_{Lg}\right)} v_{CUL,dm} + Z_h\left(i_{UL,cm} + i_{A,cm}\right) \tag{39}$$

where $v_{CUL,dm}$ describes the mode conversion term for different values of C_{Lg} and C_{Ug}. The mode conversion term is different for each converter topology due to the placement of the switching devices. By the definition of the MM decomposition matrices, this term is defined by the DM voltage across the U and L nodes in the MM model about the switching devices. In the case of the buck converter, it is readily seen from Figure 20(a) that $v_{CUL,dm}$ is defined by the dc bus voltage across the input capacitor C_i. Thus, the term $v_{CUL,dm} = v_{Ci}$ for the buck converter. In the case of the boost converter, it is readily seen from Figure 20(b) that $v_{CUL,dm}$ is defined by the voltage across the output capacitor C_o. Thus, the term $v_{CUL,dm} = v_{Co}$ for this topology.

As a final step, the CM KVL loops demonstrated in Equations (*38*) and (*39*) are combined to define the complete CM equivalent circuit representation for the parasitic capacitance section of the buck and boost converters. The CEMs defined by these KVL loops are shown in Figure 23(a) and Figure 23(b) for the buck and boost converters, respectively. The reference point P is defined to be arbitrary but will be explicitly defined in the next section in order to create the final CEM.

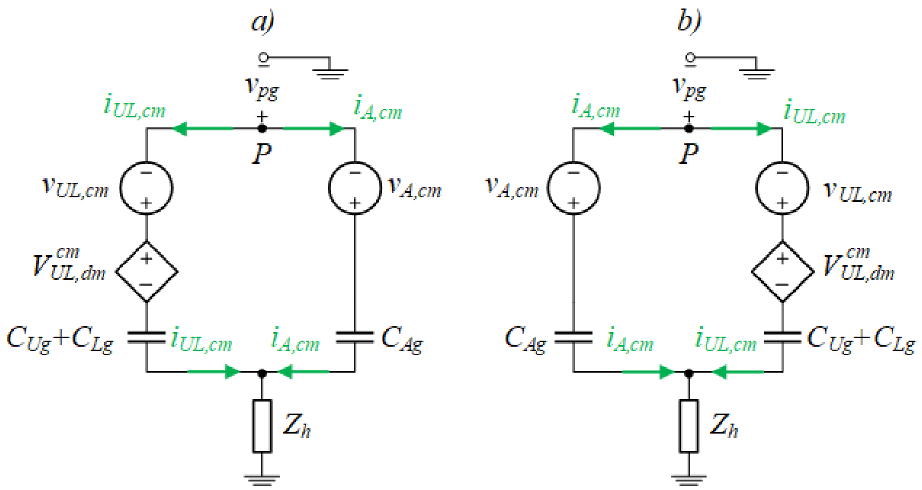

Figure 23. Parasitic BPC branch CM equivalent relationship for (a) buck and (b) boost converters

The voltage term $v_{UL,cm}$ is described by Equation *(40)*:

$$v_{UL,cm} = \frac{1}{2}(v_{UP} + v_{LP}) \tag{40}$$

The term $v_{A,cm}$ is described by Equation *(41)*:

$$v_{A,cm} = v_{AP} \tag{41}$$

Since $v_{UL,dm}^{cm}$ is topology dependent, it is handled in two separate equations. Equation *(42)* describes $v_{UL,dm}^{cm}$ for the buck converter:

$$v_{UL,dm}^{cm}(\text{buck}) = \frac{C_{Lg} - C_{Ug}}{2\left(C_{Ug} + C_{Lg}\right)} v_{Ci} \tag{42}$$

Equation *(43)* describes $v_{UL,dm}^{cm}$ for the boost converter:

$$v_{UL,dm}^{cm}(\text{boost}) = \frac{C_{Lg} - C_{Ug}}{2\left(C_{Ug} + C_{Lg}\right)} v_{Co} \tag{43}$$

3.3.4. Final CEM Construction

The fourth and final step in the decomposition method is to combine the CM equivalent representation for the parasitic capacitance branch with the other individual CM representations described previously. Since the CM decomposition is independent of the larger MM model, the

CM equivalent relationship for the parasitic branch can be combined directly with the CEMs developed in Section 3.2.4. However, because the two topologies under study have different behavior, the buck and boost converters are handled in separate sections. The buck converter is resolved first, and the analysis is readily applied to the boost converter to resolve the differences.

3.3.4.1. Buck Converter

The first step to resolve the final CEM for the buck converter with the additional parasitic branch is to specify the reference points to nodes in the MM model. The model analyzed in this section is shown in Figure 24. The MM model is also included in this figure to highlight the MM elements used in the subsequent derivation. The CEM shown in Figure 24 takes advantage of the straightforward analysis developed in Section 3.2.4.1 and eliminates v_{cm3} and v_{cm4} from the CEM. This cancellation occurs because v_{cm3} and v_{cm4} have the same magnitude and opposite signs. The parasitic branch is connected directly to the reference point P. For completeness, both CM voltage sources v_{cm1} and v_{cm2} are included from the original CEM, but the analysis in Section 3.2.4.1 is leveraged to eliminate v_{cm1} once the reference point is specified. Therefore, the only reference point that needs to be resolved is P.

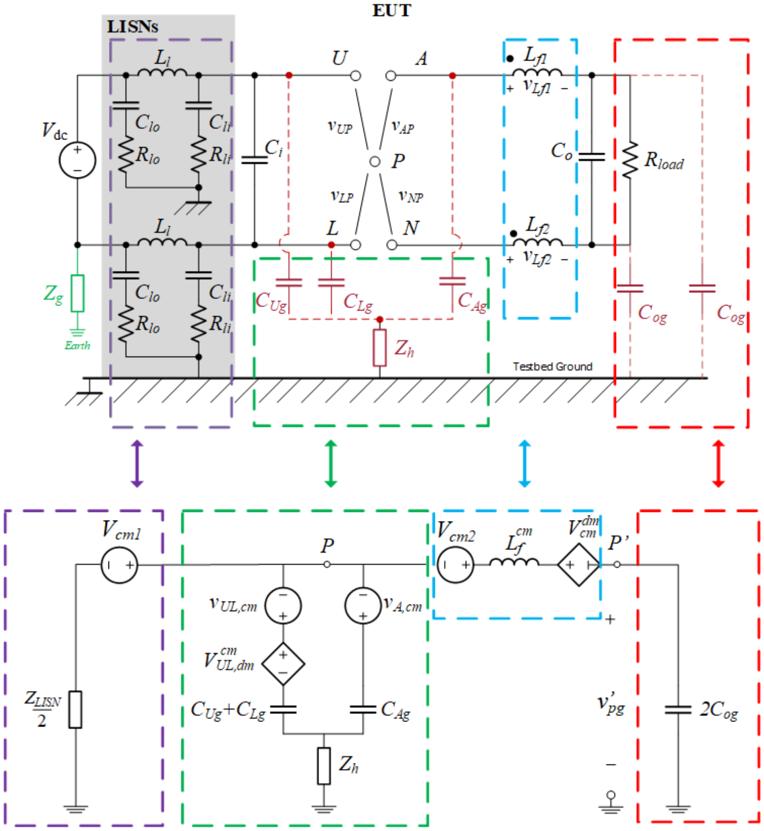

Figure 24. Initial CEM representation for the BPC model of the buck converter

The reference point P is defined in this system to be the midpoint of nodes U, L. This decision allows the parasitic branch to be placed directly into the CEM analyzed in Section 3.2.4.1 because the analysis in that section defines the CEM with respect to this node. Thus, the only analysis required for this section is to resolve the CM voltage sources for the parasitic branch at the specified reference point. The CM voltage sources of interest are $v_{UL,cm}$ and $v_{A,cm}$. The detailed derivation for the voltage sources is derived in Section A.7 of the Appendix. The CM voltage term $v_{UL,cm}$ is equal to zero due to the reference point being defined at the midpoint of the nodes U, L. The term $v_{A,cm}$ is shown to be governed by Equation *(44)*:

$$v_{A,cm} = \frac{1}{2}\left(v_{Q2} - v_{Q1}\right) \tag{44}$$

Equation *(44)* gives a definition for $v_{A,cm}$ that is suitable for defining the final CEM for the buck converter. Accordingly, the final CEM for the buck converter is shown in Figure 25. The LISN impedance is defined by Equation *(6)*; the filter inductors are defined by their frequency-domain representation with inductance equal to Equation *(13)*; and both the BPC capacitors and capacitive couplings of the load are defined by their frequency-domain representations with the magnitudes shown in Figure 25. The CM voltage source for $v_{nom,1}^{cm}$ is given by Equation (*21*), $v_{A,cm}$ is given by Equation *(44)*, and $v_{UL,dm}^{cm}$ is given by Equation *(42)*.

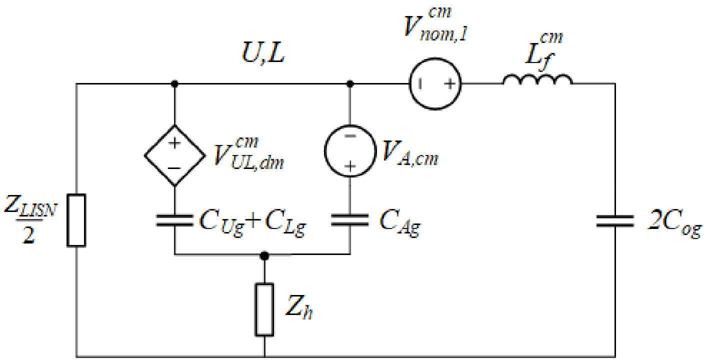

Figure 25. Final CEM for the BPC model of the buck converter

3.3.4.2. Boost Converter

The analysis needed to derive the final CEM for the BPC model of the boost converter is performed in this section. Figure 26 shows the CEM of interest. The MM model is also included in this figure to highlight the MM elements used in the subsequent derivation. The CEM shown in Figure 26 takes advantage of the analysis developed in Section 3.2.4.2 for the boost converter and eliminates v_{cm1} and v_{cm2} from the CEM. This cancellation occurs because v_{cm1} and v_{cm2} have the same magnitude and opposite signs. The parasitic branch is thus connected directly to the reference point P'. Both CM voltage sources v_{cm3} and v_{cm4} are included for the CEM defined with P', but the analysis in Section 3.2.4.2 is leveraged to eliminate v_{cm3} from the CEM once P' is specified.

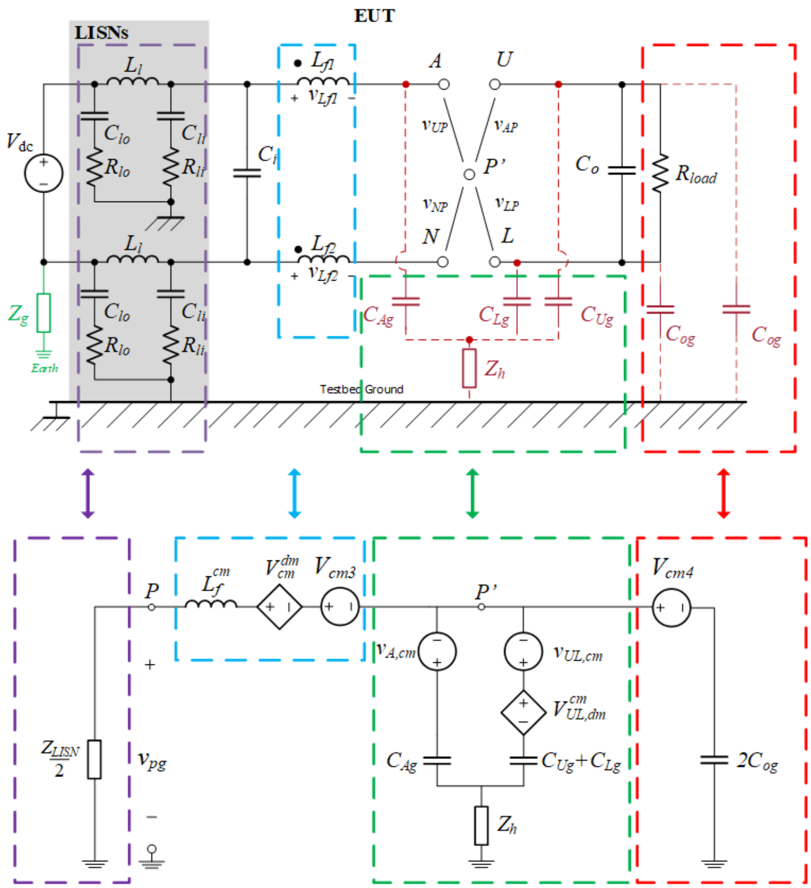

Figure 26. Initial CEM representation for the BPC model of the boost converter

The CEM is constructed for P' defined at the midpoint of nodes U, L. The justification for this choice is similar to the buck converter analysis: the final CEM for the fundamental model was constructed with this reference point specified. Therefore, the only section left to resolve is that associated with the parasitic branch voltages $v_{UL,cm}$ and $v_{A,cm}$. The detailed derivation for the voltage sources is derived Section A.8 of the Appendix. The CM voltage term $v_{UL,cm}$ is equal to zero due to the reference point being defined at the midpoint of the nodes U, L. The term $v_{A,cm}$ is shown to be governed by Equation *(45)*:

$$v_{A,cm} = \frac{1}{2}(v_{Q2} - v_{Q1}) \tag{45}$$

Equation *(45)* gives a definition for $v_{A,cm}$ that is suitable for defining the final CEM for the boost converter. Accordingly, the final CEM for the boost converter is shown in Figure 27. The primary difference between the boost converter and the buck converter is the location of the parasitic branch. The branch itself has similar CM voltage sources in both cases, and the remaining elements in the CEM are similarly defined. The LISN impedance is defined by Equation *(6)*; the filter inductors are defined by their frequency-domain representation with inductance equal to Equation *(13)*; and both the BPC capacitors and capacitive couplings of the load are defined by their frequency-domain representations with the magnitudes shown in Figure 27. The CM voltage source for $v_{nom,2}^{cm}$ is given by Equation (*25*), $v_{A,cm}$ is given by Equation *(45)*, and $v_{UL,dm}^{cm}$ is given by Equation *(43)*.

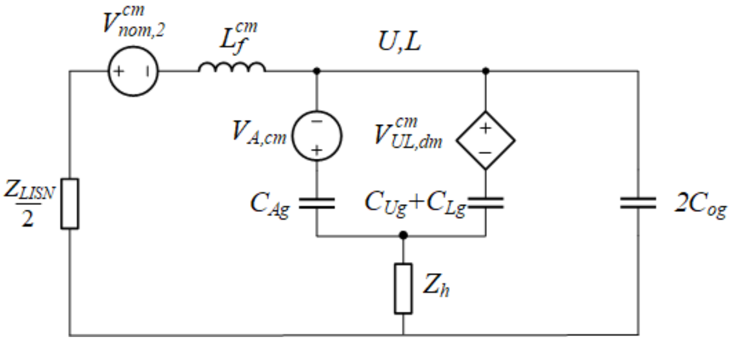

Figure 27. Final CEM for the BPC model of the boost converter

CHAPTER 4:

SIMULATION AND OPTIMIZATION

The primary focus of this chapter is to analyze the CEMs for the selected converters to understand the CM sensitivity for each topology with respect to the models described in the previous chapter. The two models of interest for each topology are the simplified model and the practical model, which includes the influence of parasitic baseplate capacitance (BPC). The analysis of the simplified model focuses on the sensitivity of the CEM to variations in the elements fundamental to the topology itself. On the other hand, the analysis of the practical model is focused on the change in behavior resulting from the introduction of the parasitic branch for each topology. The similarity of the simplified CEMs for both converters derived in Chapter 3 suggests that the CM behavior should also be similar. Due to location of the parasitic branch, the buck and boost converter CEMs for the practical model are expected to have different CM behavior for similar configurations. Therefore, this chapter treats the buck and boost converters separately, and splits the analysis for each topology into two sections. The division is between the analysis of the simplified and practical models. The boost converter is analyzed first due to the complexity that the parasitic branch introduces for the buck converter.

4.1. Boost

The dominant CM behavior for both models of interest with respect to the boost converter is analyzed in this section. The simplified model is analyzed first due to its straightforward configuration. The filter inductors constitute an influential element for this system, and thus a parametric study for the asymmetry factor is conducted for the simplified CEM. The practical model is analyzed to evaluate the impact of the addition of the parasitic branch within the CM behavior. The CEM developed in Section 3.2.4.2 is also simplified by common circuit analysis techniques to form a model that can be more readily analyzed. The resulting "analysis model" is then evaluated with respect to the remaining CM voltage sources and impedance elements. Additionally, the CM behavior predicted by the practical model is compared to a well-established model from the literature [13]. This comparison demonstrates the validity of the CEM developed for the boost converter.

4.1.1. Simplified CEM

The simplified model is analyzed first due to its simplicity. The CEM analyzed in this section is shown in Figure 28. The configuration of this CEM facilitates a straightforward analysis of the boost converter CM behavior. The primary elements considered in this analysis are the degrees of freedom that are under control of the designer for this topology.

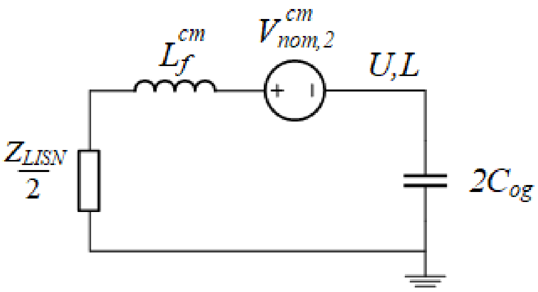

Figure 28. Fundamental CEM for the boost converter

4.1.1.1. Identification of Dominant CM Behavior

The simplicity of the simplified CEM developed for the boost converter limits the degrees of freedom in this system. For example, the impedance of the LISNs is specified by MIL-STD-461 CE102 [5] and not selected by the system designer. Similarly, C_{og} is associated with the parasitic coupling of the load, which is also generally not a design parameter. Therefore, these impedances are not considered degrees of freedom in the following analysis. The elements that are identified as being under the designer's control are those parameters associated with the CM voltage source $v_{nom,2}^{cm}$ and the CM filter inductance L_f^{cm}. These elements are analyzed in this section with respect to their boundary conditions to form a better understanding of the CM behavior of this system.

The CM voltage source shown in Figure 28, $v_{nom,2}^{cm}$, is analyzed first. Equation (*46*) restates the equation derived for $v_{nom,2}^{cm}$ from Section 3.2.4.2.

$$v_{nom,2}^{cm} = \frac{1}{2}\left[v_{Q2} - \frac{a}{1-m}\left(v_{Q2} - v_{Ci}\right) - v_{Co}\right] \tag{46}$$

As shown in Equation (*46*), $v_{nom,2}^{cm}$ is a function of the lower switch voltage, v_{Q2}, and the two capacitor voltages, v_{Ci} and v_{Co}. The lower switch voltage is a function of the input voltage, while the capacitor voltages are assumed to be near constant values with a high-frequency ripple component that is a function of the DM filtering components of these topologies. For a properly designed boost converter, the magnitude of the AC behavior is several orders of magnitude smaller than the switch voltage magnitude.

Equation (*46*) also highlights the influence of the asymmetry factor, a, and the mutual coupling factor, m, with respect to the MM voltage sources that determine $v_{nom,2}^{cm}$. Specifically, if the term $\frac{a}{1-m}$ is set to zero, $v_{nom,2}^{cm}$ is given by Equation (*47*):

$$v_{nom,2}^{cm} = \frac{1}{2}\left[v_{Q2} - v_{Co}\right] \tag{47}$$

By contrast, if the term $\frac{a}{1-m}$ is set to unity, cancellation of the lower switch voltage reduces $v_{nom,2}^{cm}$ to the expression given by Equation (*48*):

$$v_{nom,2}^{cm} = \frac{1}{2}\left[v_{Co} - v_{Ci}\right] \tag{48}$$

In addition, if the term $\frac{a}{1-m}$ is set to negative unity, the influence of v_{Q2} is doubled, and all three MM voltage sources are retained. This scenario is defined by Equation (*49*):

$$v_{nom,2}^{cm} = \frac{1}{2}\left[2v_{Q2} - v_{Ci} - v_{Co}\right] \tag{49}$$

Therefore, the CM voltage can vary widely based on the filter inductor configuration. The boundary of the CM voltage is defined by the smallest expected envelope across frequency given by Equation (*48*) and the largest given by Equation (*49*).

The last element of the system analyzed is the CM impedance. Since the LISNs and the load coupling capacitance are not system design parameters, the filter inductor configuration is the primary degree of freedom that can vary the CM impedance. The filter inductance definition from Equation (*13*) is restated in Equation (*50*):

$$L_f^{cm} = \frac{L_f}{2}\frac{(1 - a^2 - m^2)}{1 - m} \tag{50}$$

Thus, the boundary conditions for the filter inductors are dependent on the term $\frac{1-m^2-a^2}{1-m}$. If there is no mutual coupling for the filter inductors in the system ($m = 0$), the two boundary cases are defined by the definition of the asymmetry parameter, a. For the case $a = 0$, the system is fully balanced, and $\frac{1-m^2-a^2}{1-m}$ is equal to 1. This sets $L_f^{cm} = \frac{L_f}{2}$ by Equation (*13*) and indicates that the even distribution of inductance in the upper and lower rails. For the case $|a| = 1$, the system is unbalanced with an asymmetric filter inductor configuration, and $\frac{1-m^2-a^2}{1-m}$ equals zero. It is noted that $a = 1$ represents the full inductance in the upper rail, and $a = -1$ represents the full inductance in the lower rail. This configuration entirely eliminates the filter inductance from the CEM, as the inductance is strictly a differential mode component in this case. Any value of a

between these boundary cases places a proportional amount of inductance in the CEM bounded by $L_f^{cm} = \frac{L_f}{2}$.

The other influential term that determines the filter inductance in the CEM is the mutual coupling term, m. In order to isolate the influence of this term, the asymmetry factor is set to 0 to provide a simple configuration in which mutual coupling can exist. The boundary conditions for m correspond to the values 1 or -1. As the mutual coupling term approaches -1, the coefficient $\frac{1-m^2-a^2}{1-m}$ approaches zero, the filter inductance is eliminated from the CEM. This follows intuition for the characteristics of a DM filter, which is not expected to influence the CM behavior of the circuit. As the mutual coupling of the system approaches 1, the term $\frac{1-m^2-a^2}{1-m}$ approaches infinity, which approximates the behavior of a CM filter.

4.1.1.2. Assessment of Filter Asymmetry

This section applies the analysis of Section 4.1.1.1 to evaluate the influence of the asymmetry factor across a range of values. Equation (*46*) describes the total CM voltage for the simplified boost converter. Further analyzing the equation shows that dominant term is the lower switch voltage, v_{Q2}. Simplifying the equation for v_{Q2}, setting the mutual coupling term $m = 0$, and neglecting the capacitor voltages v_{Ci} and v_{Co} produces Equation (*51*):

$$v_{nom,2}^{cm} = \frac{1}{2}(1-a)v_{Q2} \tag{51}$$

Equation (*51*) highlights the primary dependency of the total CM voltage source on the asymmetry factor a. Analysis of this equation across a range of values for the asymmetry factor a provides insight into the CM behavior of the system under study. Figure 29 provides the results of this analysis. This figure demonstrates the magnitude of $v_{nom,2}^{cm}$ normalized to the DC bus voltage across a range of values for asymmetry factor a between -1 and +1. Figure 29 corroborates the analysis given in 4.1.1.1, where the largest magnitude in CM voltage was predicted for the case of a equal to negative unity (Equation (*49*)) and the smallest magnitude was predicted for the case of a equal to unity (Equation (*48*)).

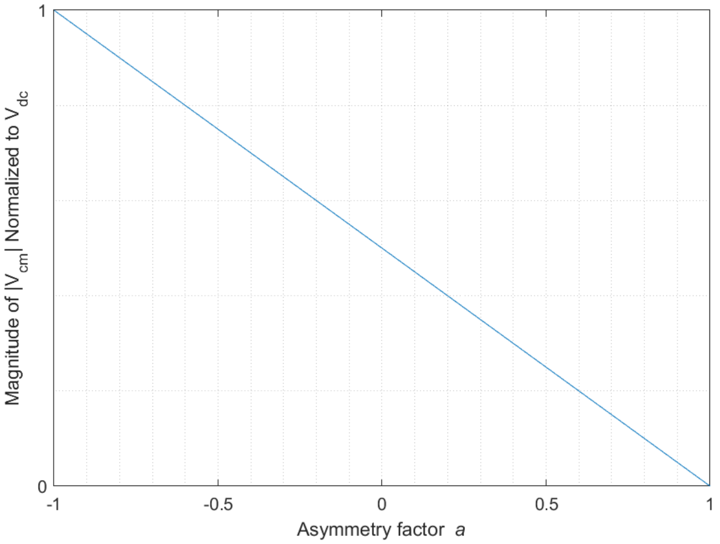

Figure 29. Sweep over asymmetry factor for normalized magnitude of total CM voltage of the simplified the boost converter

4.1.2. Practical CEM

The practical CEM model for the boost converter is developed further in this section. The presence of the BPC parasitic branch in the CEM significantly alters the CM behavior of the system. Common circuit techniques are applied to the CEM of Figure 30 to produce a simpler model that is more amenable to analysis. A more robust understanding of the CM behavior of the boost converter with respect to the inclusion of the parasitic branch is developed from analyzing this analysis CEM. The CEM is also analyzed to identify configurations for the elements of the CEM that can reduce CM emissions.

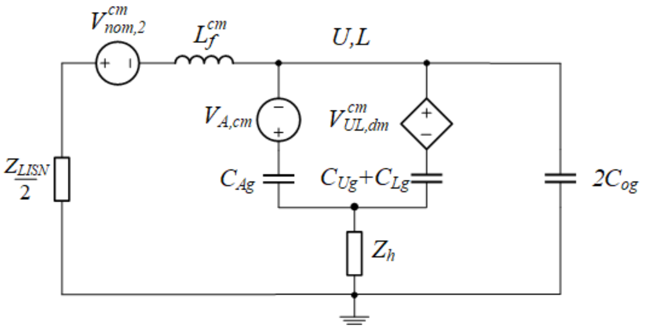

Figure 30. BPC CEM for the boost converter

4.1.2.1. Analysis Model

The analysis CEM is constructed using two techniques: applying a source transformation to the parasitic branch and finding a Thevenin equivalent circuit representation. Performing the source transformation describes the parasitic branch in a single voltage source and impedance. Applying Thevenin analysis reduces the CEM to a series circuit. These techniques simply the CEM into a form similar to the fundamental CEM derived Section 4.1.1.

4.1.2.1.1. Source Transformation for Parasitic Branch

The first step to simplify the CEM is to apply a source transformation to the parasitic branch. Figure 31(a) isolates the section of the CEM in question. The transformation reduces the A and U/L branches referenced in the CEM into a single voltage and impedance branch. The process is applied as follows: apply source transformations to the two branches individually, combine similar elements, and perform a source transformation again to resolve the reduced system into a series voltage source and impedance.

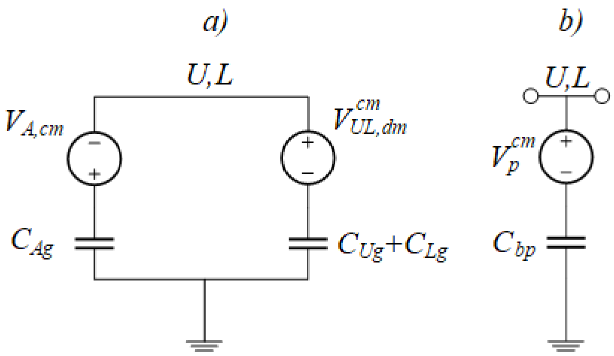

Figure 31. (a) Original and (b) source transformation parasitic BPC branch for the boost converter

The source transformation analysis is detailed in Section A.9 of the Appendix, and the final form for the parasitic branch is shown in Figure 31(b). The equation defining the voltage source v_p^{cm} is given by Equation (*52*):

$$v_p^{cm} = \frac{1}{2}\left[\frac{C_{Ag}}{C_{bp}}\left(v_{Q1} - v_{Q2}\right) + \frac{C_{Lg} - C_{Ug}}{C_{bp}} v_{Co}\right] \tag{52}$$

The impedance Z_{Cbp} defines the frequency domain relationship of the total baseplate capacitance C_{bp}.

4.1.2.1.2. Thevenin Equivalent Circuit

The second step to simplify the CEM involves applying Thevenin analysis to the CEM. Figure 32(a) identifies the CEM of interest with the updated, singular parasitic branch shown in Figure 31(b). This analysis assumes a small impedance for Z_h, so this term is neglected. Thevenin equivalent circuit techniques are applied to Figure 32(a), and the corresponding analysis is detailed in Section A.10 of the Appendix. First, the Thevenin impedance is derived. The Thevenin impedance is found by shorting the voltage sources and combining the remaining elements into a single lumped component. Figure 32(b) demonstrates that the Thevenin impedance is the parallel combination of the capacitors C_{bp} and $2C_{og}$. This is represented as a single capacitor with a value of $C_{bp} + 2C_{og}$.

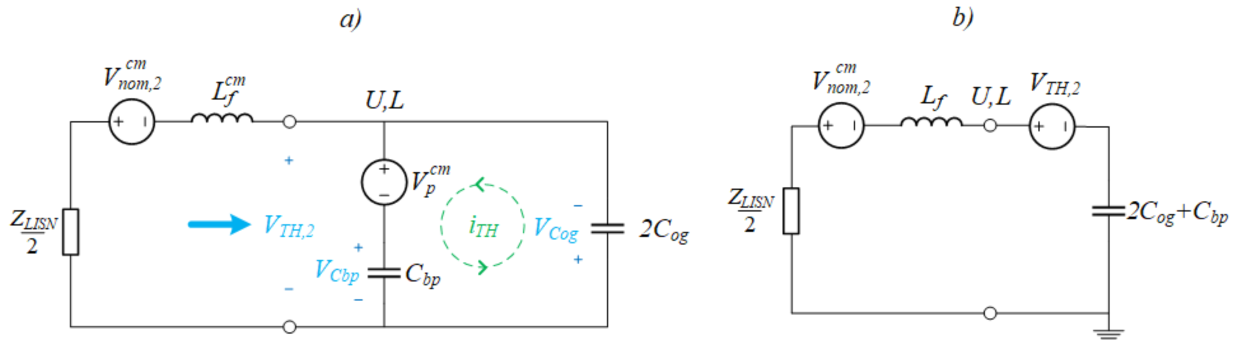

Figure 32. (a) Original CEM and (b) Thevenin equivalent representation for the practical boost converter

The completed representation for the analysis CEM is given by Figure 32(b). The LISNs, filter inductance, and $v^{cm}_{nom,2}$ were previously defined in Section 3.3.4.2 and remain unchanged. The output side of the CEM is given by the Thevenin equivalent representation. Equation (*53*) defines the Thevenin voltage source term $v_{TH,2}$:

$$v_{TH,2} = \frac{1}{2}\left[\frac{C_{Ag}}{C_{bp} + 2C_{og}}\left(v_{Q1} - v_{Q2}\right) + \frac{C_{Lg} - C_{Ug}}{C_{bp} + 2C_{og}} v_{Co}\right] \tag{53}$$

The Thevenin impedance is governed be the parallel combination of the capacitors C_{bp} and $2C_{og}$.

4.1.2.1.3. Identification of Dominant CM Behavior

A better understanding of the CM behavior of the practical boost converter is obtained by analyzing the elements of the analysis CEM developed in Section 4.1.2.1.2. The total CM voltage can be described by the series combination of $v_{TH,2}$ and $v^{cm}_{nom,2}$, which is given by Equation (*54*):

$$v^{cm}_{tot} = v^{cm}_{nom,2} + v_{TH,2} \tag{54}$$

Substituting Equation (*53*) and Equation (*46*) for $v_{TH,2}$ and $v^{cm}_{nom,2}$, respectively while extracting the common coefficient of $\frac{1}{2}$ from both equations produces Equation (*55*):

$$v_{tot}^{cm} = \frac{1}{2}\left\{\left[v_{Q2} - \frac{a}{1-m}\left(v_{Q2} - v_{Ci}\right) - v_{Co}\right] + \left[\frac{C_{Lg} - C_{Ug}}{C_{bp} + 2C_{og}} v_{Co} + \frac{C_{Ag}}{C_{bp} + 2C_{og}}\left(v_{Q1} - v_{Q2}\right)\right]\right\} \tag{55}$$

The analysis required to simplify Equation (*55*) is described in detail in Section A.11 of the Appendix. The simplification is performed by manipulating the coefficients of the MM voltages. The final expression produced by this simplification is given by Equation (*56*):

$$v_{tot}^{cm} = \frac{1}{2}\left[\left(2q_{ac} - \frac{1-m-a}{1-m}\right)\frac{v_{Q1} - v_{Q2}}{2} + \frac{a}{1-m} v_{Ci} + \left(2q_{dc} - \frac{1-m+a)}{1-m}\right)\frac{v_{Co}}{2}\right] \tag{56}$$

where $q_{ac} \triangleq \frac{C_{Ag}}{C_{bp}+2C_{og}}$ and $q_{dc} \triangleq \frac{C_{Lg}-C_{Ug}}{C_{bp}+2C_{og}}$. Equation (*56*) expresses the influence of the filter inductor configuration, BPC, and capacitive coupling from the load on the CM voltage source in a single equation. The coefficient q_{ac} defines the ratio of the A node capacitance to the sum of the BPC and load capacitance. The coefficient q_{dc} defines the ratio of the U and L node capacitances to the sum of the BPC and load capacitance. The coefficient $\left(2q_{ac} - \frac{1-m-a}{1-m}\right)$ describes the AC behavior of the CEM, while the coefficient $\left(2q_{dc} - \frac{1-m+a)}{1-m}\right)$ describes the DC behavior of the CEM with respect to the division in behavior identified in the previous chapter.

4.1.2.2. EMI Mitigation

It is possible to identify novel EMI mitigation techniques by considering the coefficients of the CM voltage source for the simplified boost converter CEM identified in Section 4.1.2.1. This section highlights the specific configurations that could be used to achieve CM mitigation. The analysis is split into two sections. The first section focuses on reducing emissions for the CEM developed in Section 4.1.2.1 by manipulating the coefficients of the CM voltage source defined by Equation (*56*). The second section offers a comparison between the CEM developed in Section 4.1.2.1 and results established in the literature.

4.1.2.2.1. CM Voltage Cancellation Trends

The analysis from Section 4.1.2.1.3 can be leveraged to develop effective EMI mitigation techniques. Analysis of the CEM informs the possibility of theoretically eliminating the CM voltage source. This elimination results from manipulated the coefficients for $(v_{Q1} - v_{Q2})$ and v_{Co}. For the coefficient of the switch voltages, defining $2q_{ac}$ as equal to $\frac{1-m-a}{1-m}$ sets the coefficient described by Equation (*56*) to zero. Similarly, defining $2q_{dc}$ as equal to $\frac{1-m+a}{1-m}$ sets the coefficient of v_{Co} described by Equation (*56*) to zero. This elimination defines v_{tot}^{cm} as a function of only v_{Ci}. The simplest way to eliminate v_{Ci} from v_{tot}^{cm} is to set a to zero. The specific configuration that achieves the described CM voltage elimination is achieved by setting the filter inductor asymmetry coefficient $a = 0$, setting C_{Ug} and C_{og} equal to zero, and setting C_{Ag} equal to C_{Lg}. The mutual coupling term is set to zero for this analysis, but this is not required. Equation (*57*) highlights the CM voltage elimination for this specific configuration:

$$v_{tot}^{cm} = \frac{1}{2}\left[\left(2\left(\frac{1}{2}\right) - 1\right)\frac{v_{Q1} - v_{Q2}}{2} + (0)v_{Ci} + \left(2\left(\frac{1}{2}\right) - 1\right)\frac{v_{Co}}{2}\right] = 0 \tag{57}$$

In reality, this configuration is not easily achieved because it is difficult to eliminate C_{ag} and C_{og} in a fielded system. However, a realistic approximation of this configuration can be achieved by setting C_{Ag} equal to C_{Lg} and making both of these capacitances significantly larger than C_{ug} and C_{og}. This configuration approximates the CM voltage source elimination. The closer the configuration of Equation (*57*) is approximated in a practical converter, the greater the reduction in CM emissions predicted by the CEM.

4.1.2.2.2. Assessment of Filter Inductor Asymmetry

This section applies the analysis of 4.1.2.1.3 to evaluate the influence of the asymmetry factor across a range of values. To demonstrate the variability of the total CM voltage source for the practical boost converter, Equation (*56*) is analyzed further. Equation (*56*) shows that dominant term is with respect to the switch voltage term, $(v_{Q1} - v_{Q2})$. Simplifying the equation for $(v_{Q1} - v_{Q2})$, setting the mutual coupling term $m = 0$, and neglecting the capacitor voltages v_{Ci} and v_{Co} produces Equation (*58*):

$$v_{tot}^{cm} = \frac{1}{2}(2q_{ac} - (1 - a))\frac{v_{Q1} - v_{Q2}}{2} \tag{58}$$

Applying a similar configuration for $2q_{ac} = 1$ as described Section 4.1.2.2.1 and simplifying the coefficients in Equation (*58*) produces Equation (*59*):

$$v_{tot}^{cm} = a\frac{v_{Q1} - v_{Q2}}{4} \tag{59}$$

Equation (*59*) highlights the primary dependency of the total CM voltage source on the asymmetry factor a. Analysis of this equation across a range of values for the asymmetry factor a provides insight into the CM behavior of the system under study. Figure 33 provides the results of this analysis. This figure demonstrates the magnitude of v_{tot}^{cm} normalized to the DC bus voltage across a range of values for asymmetry factor a between -1 and +1. Figure 33 corroborates the analysis given in this section, which predicts that a symmetric configuration ($a = 0$), along with a particular configuration of BPC element values, leads to the elimination of the CM voltage source. It is noted that the relationship between the CM voltage magnitude and the filter asymmetry factor for the practical boost converter CEM is markedly different from that of the simplified boost converter CEM. In the former, CM voltage cancellation is predicted for the balanced inductor case; in the latter, CM voltage cancellation is predicted for the unbalanced inductor case.

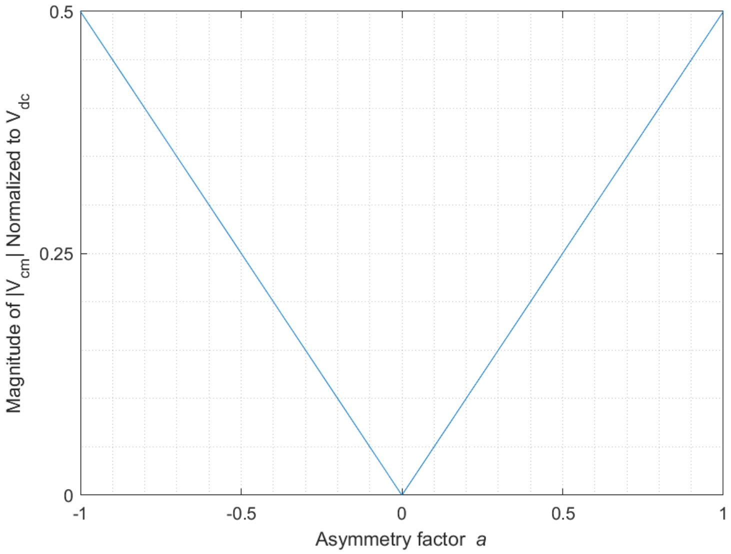

Figure 33. Sweep over asymmetry factor for normalized magnitude of total CM voltage of the practical boost converter

4.1.2.2.3. Comparison to Literature

This section compares the CEM developed in this chapter to established models from the literature. The simulation environment used to perform this analysis is Simulink, along with the Automated State Model Generator Toolbox for Simulink [25]. The model developed in Simulink is derived from the MM model shown in Figure 34The literature contains numerous treatments of the CM behavior of the boost converter. One of the most prominent treatments is the "general balancing technique" proposed by Wang et. al [13]. This analysis is widely recognized and has been used to develop new EMI mitigation techniques for dc-dc converters [14]. The general balancing technique constitutes the primary reference used for comparison of the CEM developed in Section 4.1.2.1.3. Equation (*60*) describes the governing formula for the general balancing technique referenced to the MM model given in Figure 34 [13]:

$$L_{f1}C_{Ag} = L_{f2}\left(C_{Ug} + C_{Lg}\right) \tag{60}$$

where L_{f1} defines the inductance in the upper rail and L_{f2} defines the inductance in the lower rail. Wang et al. predict that closely approximating this behavior in a physical system will essentially eliminate CM emissions for the boost topology.

This claim can also be evaluated by leveraging the CEM developed in Section 4.1.2.1.3. The parameters used to perform this comparison are shown in Table 7. It is noted that Wang et al. utilize a high-frequency assumption for the LISNs that simplifies the LISN impedance network to R_{li}. The figure of merit evaluated in this analysis is the CM voltage across the two R_{li} values that represent the LISNs.

TABLE 7

ELEMENTS USED FOR SIMULATION STUDY FOR BPC MODEL

LISNs			
R_{li}	Inboard resistor	50	Ω
R_{lo}	Outboard resistor	∞	μF
C_{li}	Inboard capacitor	0	μF
C_{lo}	Outboard capacitor	0	μF
L_l	Input inductor	50	μH
EUT			
Vdc	DC voltage	200	V
Ci	Input capacitor	10	μF
C_o	Output capacitor	100	μF
f_{sw}	Switching frequency	400	kHz
d	Duty cycle	0.5	
R_{load}	Load resistor	100	Ω
C_{og}	Capacitive coupling	0	pF
Filter Inductor Configuration			
L_f	Filter inductance	200	μH
a	Asymmetry factor	$[0.95, 0.9, 0.7, 0.4, 0.1, 0.05]$	
m	Mutual coupling	0	
L_{f1}	Upper filter inductor	$[390, 380, 340, 280, 220, 210]$	μH
L_{f2}	Lower filter inductor	$[10, 20, 60, 120, 180, 190]$	μH
Baseplate Capacitance			
C_{Ug}	U node capacitance	50	pF
C_{Ag}	A node capacitance	120	pF
C_{Lg}	L node capacitance	70	pF

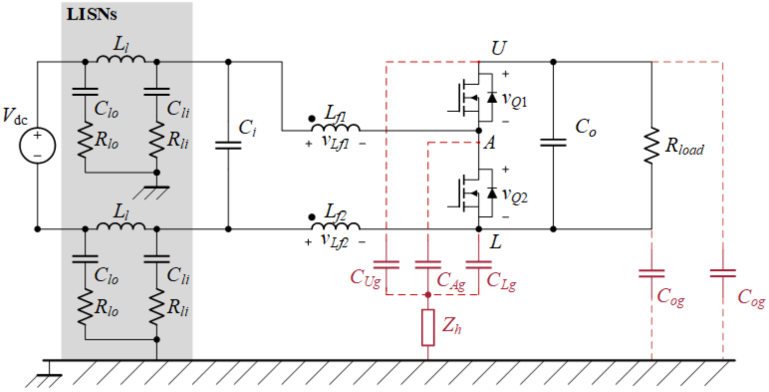

Figure 34. BPC MM model used for simulation study of boost converter

To evaluate the general balancing technique approximation, a coefficient labelled q_w is defined in Equation (*61*):

$$q_w \triangleq \frac{L_{f1}C_{Ag}}{L_{f2}\left(C_{Ug}+C_{Lg}\right)} \tag{61}$$

Equation (*61*) specifies the ratio between the left-hand and right-hand side of Equation (*60*). As q_w approaches 1, the system approaches the perfectly balanced case described in [13]. Figure 35 demonstrates the sensitivity of the CM voltages measured at the LISNs to variation in the parameter q_w. This figure was created by exercising the MM model of the boost converter implemented in Simulink across a range of q_w values. Figure 35 demonstrates that CM emissions are generally reduced when the system is configured in a more symmetric configuration ($q_w = 1.11$) as opposed to a more asymmetric configuration ($q_w = 39$). It is noted that when the system is fully balanced ($q_w = 1$), the driving CM voltage source should be eliminated. In this case, the MM simulation predicts an emissions envelope that is dominated by numerical artifacts, indicating that emissions should be negligible in this configuration. Therefore, the simulation sweep shown in Figure 35 indicates that the emissions for the practical boost converter are reduced as symmetry is approached. This trend corroborates the findings in the literature for the practical configuration of the boost converter in terms of CM emissions, as reported in [13].

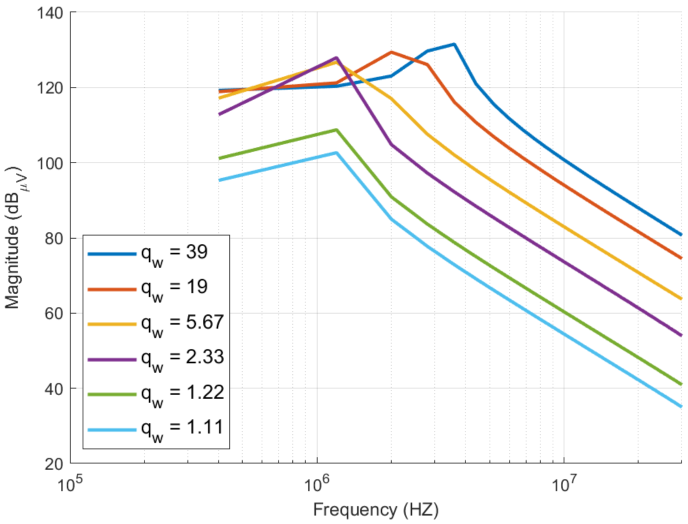

Figure 35. Approximation of the general balancing technique for the boost converter

4.2. Buck

The dominant CM behavior for both models of interest with respect to the buck converter is analyzed in this section. Similar to the boost converter, the two models constitute the division in analysis. The first analysis focuses on the simplified model, and the second analysis focuses on the practical model. The similarity to the boost converter is exploited throughout the analysis for the buck converter to take advantage of material already developed in this chapter. Similarity is exploited for the buck converter for the analysis of the simplified CEM and the source transformation of the parasitic branch in Sections 4.1.1 and 4.1.2.1.1, respectively. Development of the Thevenin equivalent circuit diverges for the buck converter, and the analysis provides a uniquely described CEM. The dominant behavior of the CEM is identified, and EMI mitigation techniques are explored. Unlike the boost converter, there is relatively little treatment of the CM behavior of the buck topology in literature. Therefore, the remainder of this thesis explores the CM behavior of the buck converter in further detail. Empirical validation of the CEMs developed for this topology is provided in the following chapter.

4.2.1. Simplified CEM

The simplified CEM is analyzed first for the buck converter. The CEM of interest is shown in Figure 36. The analysis for this section leverages the analysis in Section 4.1.1 due to the similarity between the CEM shown in Figure 36 for the buck converter and the CEM shown in Figure 28 for boost converter. The analysis in Section 4.2.1.1 explains the relationship between the CM voltage source and the filter inductor configuration. A simulation study with respect to the asymmetry factor of the filter inductors is performed to evaluate the behavior of the CEM.

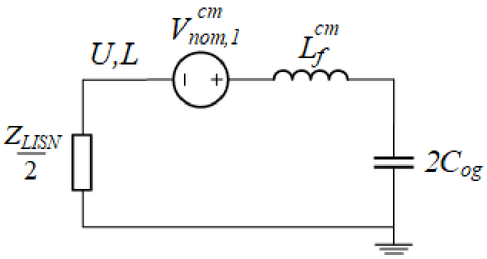

Figure 36. Fundamental CEM for the buck converter

4.2.1.1. Identification of Dominant CM Behavior

Analysis of the simplified CEM of the buck converter explains the relationship between the CM voltage source and the filter inductor configuration. As shown in Figure 36, there are limited degrees of freedom in this system. The buck converter CEM is very similar to the boost converter CEM presented in Section 4.1.1. The polarity and definition of the voltage source $v_{nom,1}^{cm}$ constitutes the primary difference between the two CEMs. The equation that defines $v_{nom,1}^{cm}$ is restated as Equation (*62*):

$$v_{nom,1}^{cm} = \frac{1}{2}\left[v_{Q2} - \frac{a}{1-m}\left(v_{Q2} - v_{Co}\right) - v_{Ci}\right] \tag{62}$$

Similar to the analysis of the boost converter, insight can be gained into the CM behavior of the buck converter by considering the boundary cases for the coefficients in Equation (*62*). For example, if the term $\frac{a}{1-m}$ is set to zero, $v_{nom,1}^{cm}$ is given by Equation (*63*):

$$v_{nom,1}^{cm} = \frac{1}{2}\left[v_{Q2} - v_{Ci}\right] \tag{63}$$

By contrast, if the term $\frac{a}{1-m}$ is set to unity, there is cancellation of the lower switch voltage, and $v_{nom,1}^{cm}$ is given by Equation (*64*):

$$v_{nom,1}^{cm} = \frac{1}{2}\left[v_{Co} - v_{Ci}\right] \tag{64}$$

Additionally, if the term $\frac{a}{1-m}$ is set to equal to negative unity, the influence of v_{Q2} is doubled, and all three MM voltage sources are retained. This configuration for $v_{nom,1}^{cm}$ is given by Equation (*65*):

$$v_{nom,1}^{cm} = \frac{1}{2}\left[2v_{Q2} - v_{Co} - v_{Ci}\right] \tag{65}$$

Thus, the asymmetric, canonical configuration of the buck converter is predicted to provide reduced emissions compared to the symmetric configuration for the filter inductors. Equations (*63*)-(*65*) demonstrate the similar behavior to Equations (*47*)-(*49*), which implies that the buck and boost converter are nearly identical for the simplified CEMs of these converter topologies.

4.2.1.2. Assessment of Filter Asymmetry

This section applies the analysis of Section 4.2.1.1 to evaluate the influence of the asymmetry factor across a range of values. Equation (*62*) describes the total CM voltage for the simplified boost converter. Further analyzing the equation shows that dominant term is the lower switch voltage, v_{Q2}. Simplifying the equation for v_{Q2}, setting the mutual coupling term $m = 0$, and neglecting the capacitor voltages v_{Ci} and v_{Co} produces Equation (*66*):

$$v_{nom,1}^{cm} = \frac{1}{2}(1 - a)v_{Q2} \tag{66}$$

Equation (*66*) highlights the primary dependency of the total CM voltage source on the asymmetry factor a. Analysis of this equation across a range of values for the asymmetry factor a provides insight into the CM behavior of the system under study. Figure 37 provides the results of this analysis. This figure demonstrates the magnitude of $v_{nom,2}^{cm}$ normalized to the DC bus voltage across a range of values for asymmetry factor a between -1 and +1. Figure 37corroborates the analysis given in Section 4.2.1.1, in which the largest magnitude in CM voltage was predicted for the case of a equal to negative unity (Equation (*65*)) and the smallest magnitude was predicted for the case of a equal to unity (Equation (*63*)).

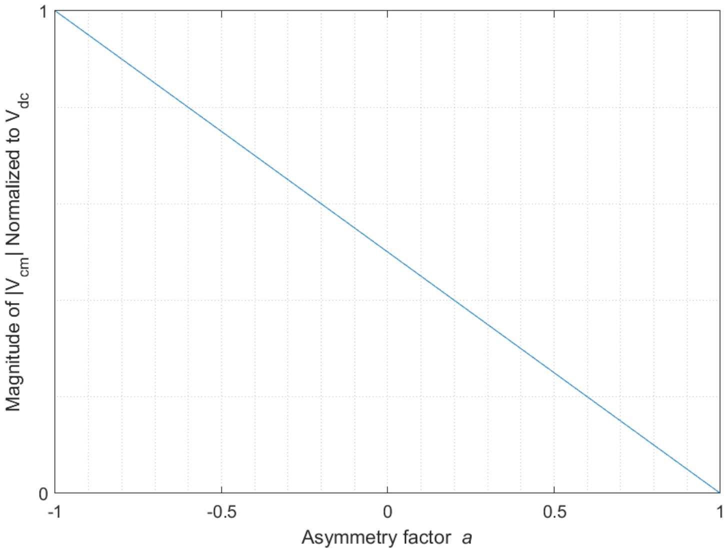

Figure 37. Sweep over asymmetry factor for normalized magnitude of total CM voltage of the simplified the buck converter

4.2.2. Practical CEM

The practical CEM model for the buck converter is developed further in this section. The presence of the BPC parasitic branch in the CEM significantly alters the CM behavior of the system. Common circuit techniques are applied to the CEM of Figure 38 to produce a simpler model that is more amenable to analysis. A more robust understanding of the CM behavior of the buck converter with respect to the inclusion of the parasitic branch is developed from analyzing this simpler CEM. The simpler CEM is also analyzed to identify configurations for the elements of the CEM that can reduce CM emissions.

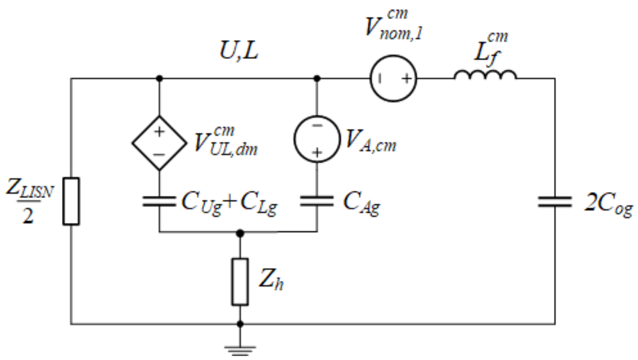

Figure 38. BPC CEM for the buck converter

4.2.2.1. Analysis Model

The practical CEM for the buck converter is reduced to a configuration more amenable for analysis in this section. The analysis CEM is constructed using two techniques: applying a source transformation to the parasitic branch and finding a Thevenin equivalent circuit representation. The parasitic branch introduces unique behavior for the buck converter that is captured in the development of the Thevenin equivalent circuit. The principal uniqueness for the buck converter is the inclusion of a frequency-dependent Thevenin voltage source. A coefficient is defined to describe this frequency dependence, and the system behavior is evaluated with respect to this parameter.

4.2.2.1.1. Source Transformation for Parasitic Branch

The first step to simplify the CEM is to apply a source transformation to the parasitic branch. Figure 39(a) isolates the section of the CEM in question. The transformation reduces the A and U/L branches referenced in the CEM into a single voltage and impedance branch. The process is applied as follows: apply source transformations to the two branches individually, combine similar elements, and perform a source transformation again to resolve the reduced system into a series voltage source and impedance.

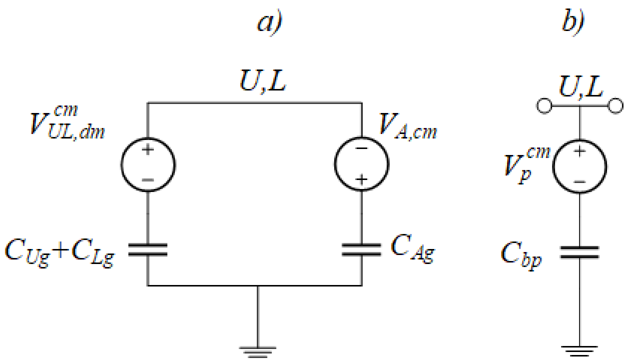

Figure 39. (a) Original and (b) source transformation parasitic BPC branch for the buck converter

The source transformation analysis is detailed in Section A.8 of the Appendix, and the final form for the parasitic branch is shown in Figure 39(b). The equation defining the voltage source v_p^{cm} is given by Equation (*67*):

$$v_p^{cm} = \frac{1}{2}\left[\frac{C_{Lg} - C_{Ug}}{C_{bp}} v_{Ci} + \frac{C_{Ag}}{C_{bp}}\left(v_{Q1} - v_{Q2}\right)\right] \tag{67}$$

The impedance Z_{Cbp} defines the frequency domain relationship of the total baseplate capacitance C_{bp}.

4.2.2.1.2. Thevenin Equivalent Circuit

The second step to simplify the system involves applying Thevenin equivalent circuit techniques to the CEM. The CEM of interest is shown in Figure 40(a), with the updated parasitic branch included from Figure 39(b). This analysis assumes a small impedance for Z_h, so this term is neglected. As shown in Figure 40(a), the parasitic branch constitutes an additional current path electrically located between the filter inductors and the LISNs. Since the LISNs are the primary means of measurement in a compliance test setup, the parasitic branch provides an additional, influential current path between the LISNs and filter inductors. As will be shown, the Thevenin equivalent circuit includes a frequency-dependent term that describes the influence of the parasitic branch on the CM behavior across the frequency spectrum. It is noted that due to the location of the parasitic branch, both v_p^{cm} and $v_{nom,1}^{cm}$ will be integrated into the formulation of $v_{TH,1}$.

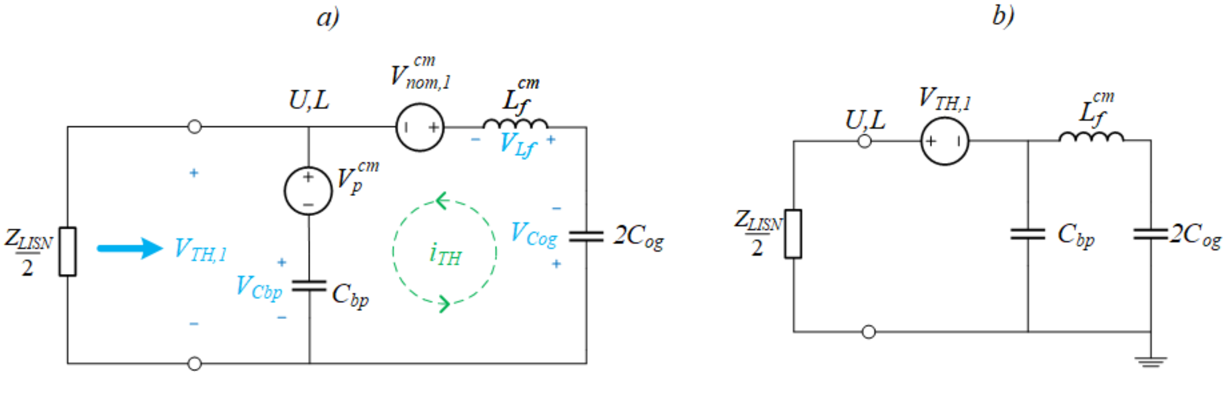

Figure 40. (a) Original CEM and (b) Thevenin equivalent representation of the practical buck converter

The analysis that defines the Thevenin equivalent is provided in Section A.12 of the Appendix. The final equivalent circuit is shown in Figure 40(b). The Thevenin impedance, Z_{TH}, is defined by Equation (*68*):

$$Z_{TH} = \frac{Z_{Cbp}(Z_{Lf} + Z_{Cog})}{Z_{Cbp} + Z_{Lf} + Z_{Cog}} \tag{68}$$

The impedance given by Equation (*68*) is connected in series with the CM LISN impedance to form the total CM impedance for this system. A frequency-dependent coefficient is defined by Equation (*69*):

$$q_{TH} = \frac{1}{1 + \frac{C_{bp}}{2C_{og}} - \omega^2 C_{bp} L_f^{cm}} \tag{69}$$

The term q_{TH} provides a useful construct for defining the Thevenin voltage source. Analysis of this term reveals three primary frequency bands: a low frequency band dominated by the ratio $\frac{C_{bp}}{2C_{og}}$; a resonant point; and a high frequency band governed by the term $-\omega^2 C_{bp} L_f^{cm}$. The Thevenin voltage source is defined with respect to this frequency-dependent coefficient in Equation (*70*):

$$v_{TH,1} = (1 - q_{TH})v_p^{cm} - q_{TH}v_{nom,1}^{cm} \tag{70}$$

Equation (*70*) demonstrates a level of symmetry about q_{TH} that is analyzed in subsequent sections.

4.2.2.2. Identification of Dominant CM Behavior

The dominant CM behavior for the CEM developed in 4.2.2.1.2 is analyzed in this section. The CM behavior is driven by the Thevenin voltage source $v_{TH,1}$, which is dependent on the coefficient q_{TH}. If q_{TH} is equal to one, the dominant behavior is a function of $v_{nom,1}^{cm}$. In contrast, if q_{TH} is equal to zero, the dominant behavior is a function of v_p^{cm}. Thus, the analysis focuses on the coefficient q_{TH}, defined by Equation (*69*), with respect to its impact on $v_{TH,1}$.

The term q_{TH} constitutes a powerful representation of the interaction between the CM impedance elements and the driving CM voltage source across the frequency spectrum. When q_{TH} is unity, the coefficient for v_p^{cm} in Equation (*70*) is eliminated, and $v_{TH,1}$ is defined by Equation (*71*):

$$v_{TH,1} = -v_{nom,1}^{cm} \tag{71}$$

Equation (*71*) indicates that the CM behavior is dominated by the outer loop of the CEM, or the behavior independent of the parasitic branch. By contrast, when q_{TH} is zero, the coefficient for $v_{nom,1}^{cm}$ in Equation (*70*) is eliminated. The voltage source $v_{TH,1}$ is thus defined by Equation (*72*):

$$v_{TH,1} = v_p^{cm} \tag{72}$$

Equation (*72*) indicates that the CM behavior is dominated by the parasitic branch. In this case, CM current flows between the LISNs and the parasitic branch and does not interact with the filter inductance and capacitive load coupling.

4.2.2.3. EMI Mitigation

It is possible to identify novel EMI mitigation techniques by considering the coefficients of the CM voltage source for the simplified boost converter CEM identified in Section 4.2.2.1. This section highlights the specific configurations that could be used to achieve CM mitigation. The analysis is split into two sections. The first section focuses on reducing emissions for the CEM developed in Section 4.2.2.1 by manipulating the coefficients of the CM voltage source defined by Equation (*70*). The second provides an analysis of two specific configurations that are employed for empirical validation of the buck converter CEMs in the following chapter of this thesis. Also included in this section is a simulation study performed to identify the influence of the filter inductor configuration on the CM voltage source.

4.2.2.3.1. CM Voltage Cancellation Trends

The analysis from Section 4.2.2.2 can be leveraged to develop effective EMI mitigation techniques. Analysis of the CEM informs configurations that can be used to minimize emissions for the practical buck converter. The analysis is focused around the CM voltage source given by Equation (*70*) and the frequency-dependent coefficient q_{TH}. Equation (*70*) was defined in Section 4.2.2.2 by two boundary conditions with respect to q_{TH}, which the analysis in this section follows. The CM voltage source is governed by $v_{nom,1}^{cm}$ when q_{TH} was equal to unity (Equation (*71*)), and the voltage source is governed by v_p^{cm} when q_{TH} was equal to zero (Equation (*72*)).

The case for q_{TH} was equal to unity defines the influence of the outer loop of the CEM to be dominant. The analysis for this behavior is given in Section 4.2.1.1. The case for q_{TH} was equal to zero defines the influence of the parasitic branch of the CEM to be dominant. The equation for v_p^{cm} is restated in Equation (*73*):

$$v_p^{cm} = \frac{1}{2}\left[\frac{C_{Lg} - C_{Ug}}{C_{bp}} v_{Ci} + \frac{C_{Ag}}{C_{bp}}\left(v_{Q1} - v_{Q2}\right)\right] \tag{73}$$

Equation (*73*) is governed by the interaction between the U and L nodes together and the A node by itself. The coefficient for the switch voltages can be set to zero by setting C_{Ag} equal to zero; and the coefficient for v_{Ci} can be set to zero by setting C_{Lg} equal to C_{Ug}. This configuration defines the CM voltage source to be zero and predicts reduced emissions.

4.2.2.3.2. Assessment of Filter Asymmetry

Due to lack of treatment, it is not possible to rely on published results to corroborate the CM trends predicted by the buck converter CEMs developed in this thesis. Instead, empirical validation of these trends is provided in the following chapter of this thesis. The remainder of this section provides suitable parametric studies based on the CM voltage source equation for $v_{TH,1}$, given by Equation (*70*). The two voltage sources that constitute $v_{TH,1}$ are v_p^{cm} (Equation (*73*)) and $v_{nom,1}^{cm}$ (Equation (*63*)). The simplified expression for $v_{nom,1}^{cm}$ is given by Equation (*66*). Analyzing Equation (*73*) shows that the switch voltages dominate v_p^{cm}. Simplifying $v_{TH,1}$ for $v_{nom,1}^{cm}$ and v_p^{cm} produces Equation (*74*):

$$v_{TH,1} = (1 - q_{TH})\left[\frac{1}{2}\frac{C_{Ag}}{C_{bp}}\left(v_{Q1} - v_{Q2}\right)\right] - q_{TH}\left[\frac{1}{2}(1 - a)v_{Q2}\right] \tag{74}$$

To further simplify the analysis, C_{Ag} and C_{bp} are configured as described in Section 4.1.2.2.2 so that the ratio $\frac{C_{Ag}}{C_{bp}}$ is equal to $\frac{1}{2}$, which produces Equation (*75*):

$$v_{TH,1} = \frac{(1 - q_{TH})}{4}\left(v_{Q1} - v_{Q2}\right) - \frac{q_{TH}(1 - a)}{2} v_{Q2} \tag{75}$$

Equation (*75*) highlights the primary dependence of the total CM voltage source on the asymmetry factor a. Analysis of this equation across a range of values for the asymmetry factor a provides insight into the CM behavior of the system under study. The term q_{TH} was used in Section

4.2.2.2 to identify boundary conditions for the behavior of the CEM. This parameter is evaluated across a range of values as well to observe its influence on the CM behavior. Figure 41 provides the results of this analysis. This figure demonstrates the magnitude of $v_{nom,2}^{cm}$ normalized to the DC bus voltage across a range of values for asymmetry factor a between -1 and +1. Figure 41 corroborates the analysis given in Section 4.2.2.3.1 with reference to q_{TH} equal to zero and unity. It is noted that the influence of q_{TH} adjusts the asymmetry factor value at which CM voltage cancellation occurs. When the outer loop of the CM is dominant ($q_{TH} = 1$), CM voltage cancellation is predicted for the case with the inductor lumped in the positive rail ($a = 1$). As the influence of the parasitic branch increases ($q_{TH} < 1$), the value of a for which CM voltage cancellation also decreases. It is further noted that when the parasitic branch of the CM is dominant ($q_{TH} = 0$), the filter inductor does not appear in the CEM and CM voltage cancellation is not possible.

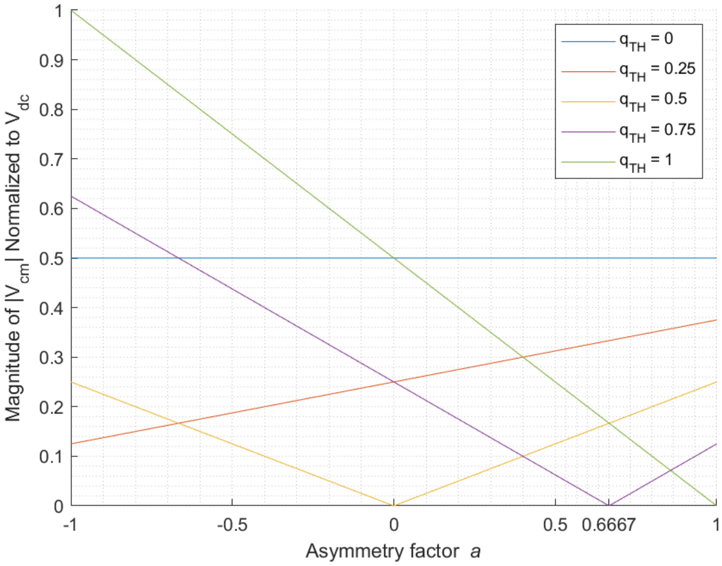

Figure 41. Sweep over asymmetry factor for normalized magnitude of total CM voltage for the practical buck converter

CHAPTER 5:

EMPIRICAL VALIDATION OF BUCK CONVERTER MODELS

To verify the CEMs presented in the previous chapters, a set of empirical studies was conducted at varying operating conditions. Although the CEM analysis of both the buck and boost converters have been discussed in this thesis, these empirical studies focus exclusively on the buck converter. This is due to the relative lack of treatment of the CM behavior of the buck converter in the literature as compared to the boost converter. The experiments for model validation were performed in a two-tier approach. First, a low-power (10 W) buck converter using silicon (Si) MOSFETs was designed and evaluated. The purpose of this set of experiments was to validate the simplified buck converter CEM. Second, a high-power (200 W) buck converter using gallium-nitride (GaN) MOSFETs was designed and evaluated. This set of experiments built on the knowledge gained in the low-power experiments and was performed to validate the practical buck converter CEM. This section describes these two hardware configurations and compares empirical measurements from these systems with the associated model predictions.

5.1. Low-Power Experiments

The first phase of experimental procedures was developed to evaluate the simplified buck converter CEM, without the influence of the parasitic BPC elements. The hardware setup used for these experiments involves SiC MOSFETs that are integrated into a custom-designed PCB based on [28]. The power level permits the design to be isolated to a single board, which allows the CM behavior to be isolated for the simplified CEM. Due to the testing being isolated, test setup simplifies the models used in previous chapters by replacing the LISNs with Y-capacitors and including a CM return path on the PCB that is connected at the midpoint of the input capacitors and load capacitors.

5.1.1. Testing Setup

The first phase of experimental procedures was developed to evaluate the simplified buck converter CEM, without the influence of the parasitic BPC elements. To simplify the number of parameters in this initial set of experiments, the LISNs in the previous modeling descriptions were replaced with Y-capacitors. Although this configuration differs from the derivations described earlier in this thesis, the CEM of the simplified buck converter can be readily modified to describe this system. The MM model for this configuration is shown in Figure 42(a) and the modified CEM for the simplified buck converter is shown in Figure 42(b). The only difference between this setup and the decomposition in previous chapters is the input impedance of the CEM. The updated CEM, shown in Figure 42(b), replaces the LISNs with input capacitors connected to the CM return path.

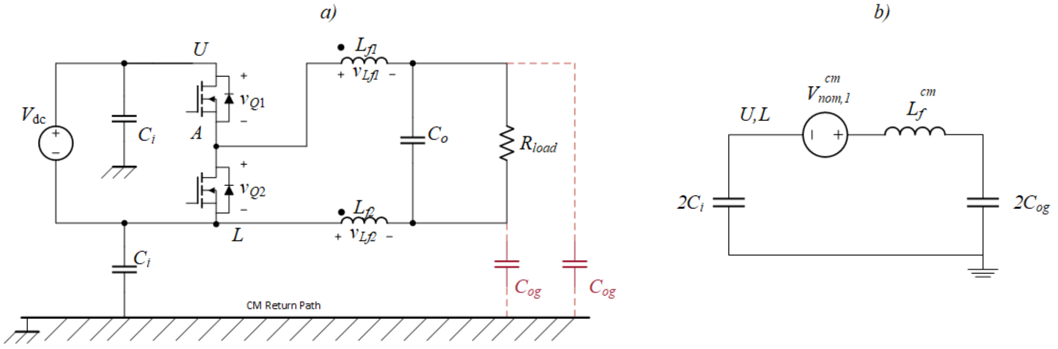

Figure 42: Updated (a) MM model and (b) CEM for the simplified buck converter

With the substitution of Y-capacitors for the LISNs, the entire buck converter setup could be implemented on a single printed circuit board (PCB). The PCB used in this portion of the evaluation is shown in Figure 43. The system was designed based on the design described in [28]. The semiconductor technology used for the active switch in this system is a Fairchild Semiconductor P-Channel Silicon TO-220 FQP11P06 MOSFET with $R_{DS(on)}$ of 140 mΩ [29]. A

Fairchild Semiconductor SB580-D Silicon Schottky diode is used in place of the lower switch [30]. The gate driver for the active switching device was implemented with a single NPN BJT, along with a gate resistance of 100 Ω [31]. The CM return path is established by a large copper area on the PCB that connects the input capacitors to the load capacitors. The bill of materials for the remaining elements for this test setup is presented in Table 8.

TABLE 8

BILL OF MATERIALS FOR LOW-POWER BUCK CONVERTER

Component	Manufacturer	Part Number	Description
C_i	TDK	FG26X5R1E476MRT06	47 µF 25V ceramic capacitors
C_{og}	Kemet	C315C100J2G5TA	10 pF 200V ceramic capacitors
C_o	Nichicon	UVR2C010MED	1 µF 160V aluminum electrolytic capacitor
L_f	Murata	19R683C	68 µH radial lead inductors

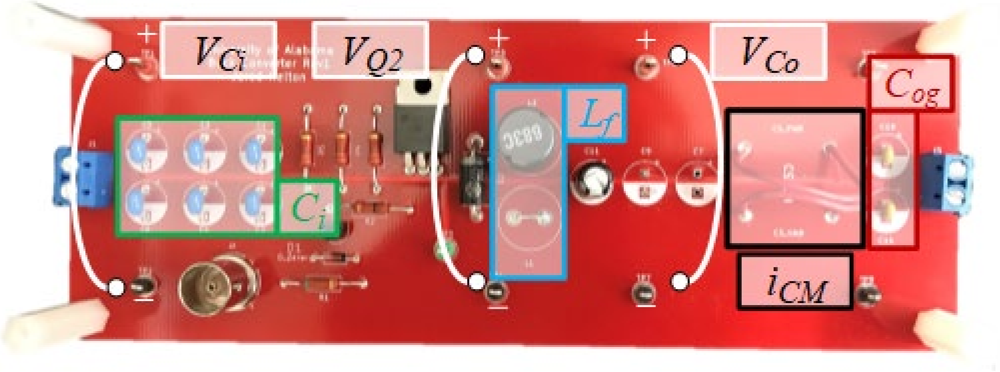

Figure 43. Test setup for low-power buck converter

5.1.2. Testing Procedure

The procedure for operating the low-power buck converter and processing the experimental results is described in this section. The operating conditions employed for these experiments are described in Table 9. The testing procedure is divided into two cases. The first case is the asymmetric filter inductor configuration. This is realized by configuring the test setup shown in Figure 43 with a single 68 µH inductor placed in the upper rail. The second case is the symmetric filter inductor configuration. This setup is realized by configuring the test setup shown in Figure 43 with two 68 μH inductors: one in the upper rail and one in the lower rail.

TABLE 9
PARAMETERS FOR TESTING OF LOW-POWER TEST SETUP

Parameters		Values		Units
		Case 1	Case 2	
EUT				
V_{dc}	Input voltage	15	~	V
C_o	Output capacitance	1	~	μF
f_{sw}	Switching frequency	200	~	kHz
d	Duty cycle	0.67	~	
R_{load}	Load resistor	10	~	Ω
C_i	Input capacitors	70.5	~	μF
C_{og}	Capacitive coupling of load	10	~	pF
Filter Inductors				
L_f	Filter Inductance	68	~	μH
a	Asymmetry factor	1	0	
m	Mutual coupling	0	~	

The results of these experiments are used to evaluate the accuracy of the simplified buck converter CEM. The quantities measured in the experimental setup include three MM voltages and a single CM current. The three voltages are indicated in Figure 43: the input voltage, v_{Ci}; the lower switch voltage, v_{Q2}; and the output voltage, v_{Co}. These MM voltage measurements are used to generate the CM voltage signals needed to populate the CEM. The CM current is measured by simultaneously measuring the upper and lower rail currents with a single current probe on the output of the system. The location within the system where this measurement is performed is highlighted in Figure 43. The CM current measurement is utilized as the reference data for comparison with the predictions of the CEM.

The model is populated by using the measured MM voltages to compute the CM voltage source, and by generating a transfer function to represent the CM impedance. The time-domain measurements are converted to the frequency-domain using the FFT function within MATLAB.

The measured voltages are combined to represent the final CM voltage source by utilizing Equation (62). The transfer function for the CM impedance is formulated by combining the frequency-domain representation of each element in the CEM. The simplified buck converter CEM is a series configuration, as shown in Figure 42(b). Therefore, the total CM impedance is the series combination of the input capacitor impedance, the filter inductor impedance, and the load coupling impedance. The final step in generating the modeled CM current is completed by dividing the CM voltage by the CM impedance.

5.1.3. Metrology

The metrology used to measure the quantities of interest in the low-power test setup is described in this section. The MM voltages are measured using Tektronix THDP0200 differential probes, which have a bandwidth of 200 MHz [36]. For all experiments described here, the differential probes were configured in the low-voltage range setting (150 V) for improved resolution. The CM current was measured using a Tektronix TCP0030A current probe, which has a bandwidth of 120 MHz [37]. The probe was configured in the low-current range setting (5 A) for improved resolution. All measured signals were monitored and recorded using a Tektronix MDO4104B-3 oscilloscope, which has a bandwidth of 500 MHz [38].

5.1.4. Results

To configure the model for comparison with experimental data, the CEM was populated with the parameters shown in Table 9. The model prediction of the CM current for this system is compared in the frequency domain with the measured results for the asymmetric case ($a = 1$) in Figure 44(a) and for the symmetric case ($a = 0$) in Figure 44(b). The basis of this comparison is the CM current evaluated at the output of the system. Since the model constitutes a series loop, the location of the measurement does not change the result. Thus, the choice of location for the measurement is based on convenience. The modeled spectrum is displayed only for the magnitude peaks of the switching frequency and its harmonics. This stylistic choice is made to facilitate a clear comparison between the model and experimental results. Figure 44 demonstrates good agreement between the model predictions and measured results for both the asymmetric and symmetric filter inductor configurations. This agreement is maintained up to the highest frequency considered by conducted emissions standards (30 MHz). Figure 44 also corroborates the predicted reduction in emissions between the two filter inductor configurations. The analysis in Section 4.2.1 predicts that the configuration of the simplified buck converter that produces minimized CM emissions is the asymmetric configuration with the inductance concentrated in the upper rail ($a = 1$). Figure 44 demonstrates greater than a 20 dB decrease in magnitude in the CM current for the asymmetric configuration compared to the symmetric configuration near the switching frequency and its first harmonics.

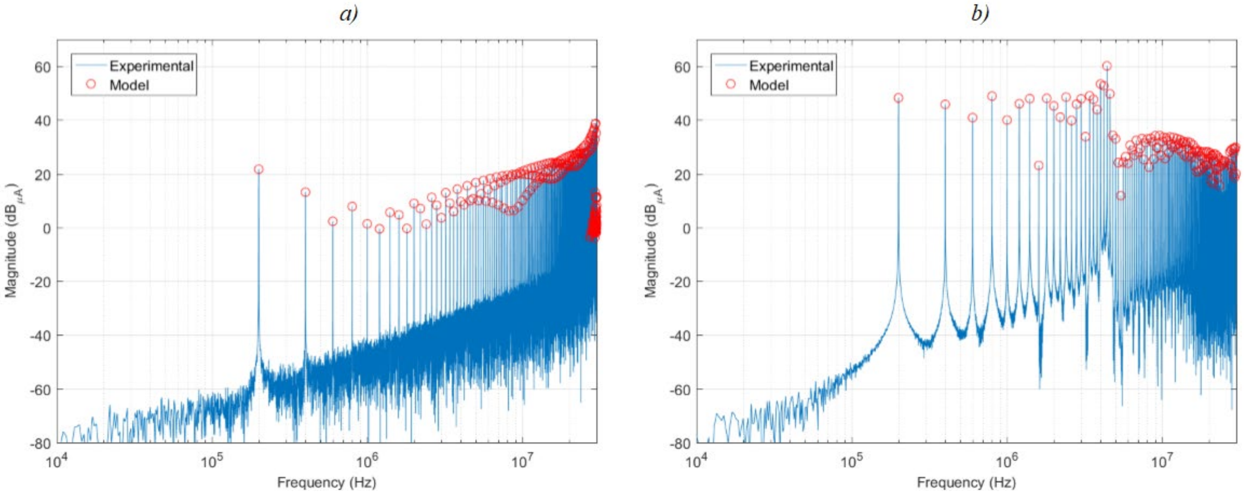

Figure 44. Comparison between the CEM prediction and empirical measurements of output CM current for (a) asymmetric and (b) symmetric filter inductor configuration for simplified buck converter

5.1.5. Parameters of Sensitivity

During the experiments described in Section 5.1.4, several insights were gained into the CM behavior of the simplified buck converter. One significant finding is that the CM behavior in the high-frequency regime (10-30 MHz) is significantly influenced by the input voltage dynamics. The analysis in Section 4.1.1 suggested that the input voltage is essentially a constant value, and that its AC behavior can be neglected. However, during the experiments described in Section 5.1.4, this assumption was found to be invalid. To clarify why this is the case, Figure 45 demonstrates the CM voltage spectrum calculated from the individual MM voltages for the asymmetric configuration of the low-power buck converter.

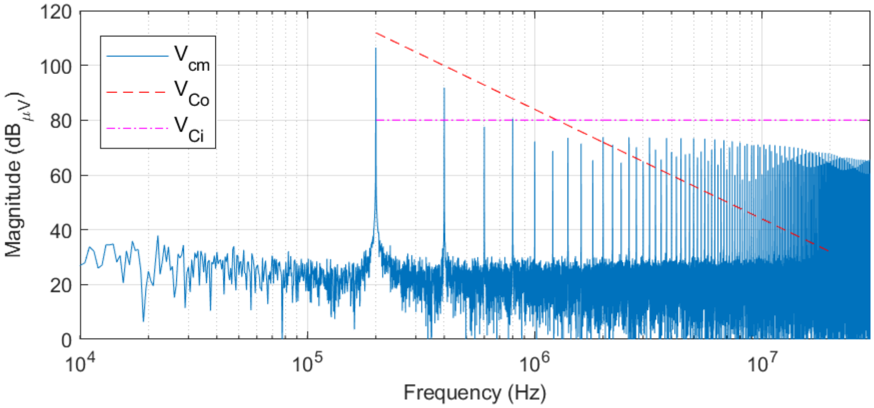

Figure 45. CM voltage spectrum and influential terms

The red dashed line in Figure 45 represents the envelope of the expected 40 dB/decade roll-off associated with the output capacitor voltage. The magenta dashed line represents the envelope of the measured input voltage, which includes substantial high-frequency content out to 30 MHz. The combined CM voltage is predicted to follow the trend of v_{Co} if the input voltage dynamics are neglected. However, Figure 45 shows that the combined CM voltage includes substantial content in the 1-30 MHz range. Thus, the input voltage dynamics cannot be neglected in this setup and must be incorporated through inclusion of the measured v_{Ci} waveform in the combined CM voltage source. The model agreement shown in Figure 44 was obtained through applying this procedure. This procedure is also leveraged for the high-power empirical comparisons that are described in the following section. This finding indicates that the high *dv/dt* transitions of the switch voltages proliferate into the CM behavior by means of the ripple content that appears on the input voltage. This highlights the necessity to include all voltages informed by the CM analysis for the model match.

5.2. High-Power Experiments

The second phase of experimental procedures was developed to evaluate the practical buck converter CEM, which includes the influence of the parasitic BPC elements. Knowledge gained from the first phase of experiments is leveraged and incorporated into the experimental setup for this phase. The hardware setup used for these experiments involves Gallium Nitride (GaN) lateral High-Electron-Mobility Transistors (HEMTs) that integrated into a custom-designed PCB. The GaN devices introduce additional complexity into the system due to their high edge-rates [27]. As will be shown, this behavior increases the energy in the high-frequency regime. The high-power experimental setup also incorporates LISNs as a grounding plane to more faithfully represent the behavior of a practical buck converter implementation.

5.2.1. Testing Setup

The high-power experimental setup directly represents the configuration of the practical buck converter described in Section 4.2.2. For this phase of experiments, a portion of the hardware setup described in [24] is leveraged. This setup includes a pair of LISNs on the input of the converter along with a copper ground plane that mechanically supports the equipment under test (EUT). The MM model that represents this configuration is shown in Figure 46. The switching devices are changed from the Si devices used in the low power testing setup to GaN semiconductors that are incorporated into a fabricated PCB. The individual subsystems that constitute this testbed are described in the following sections.

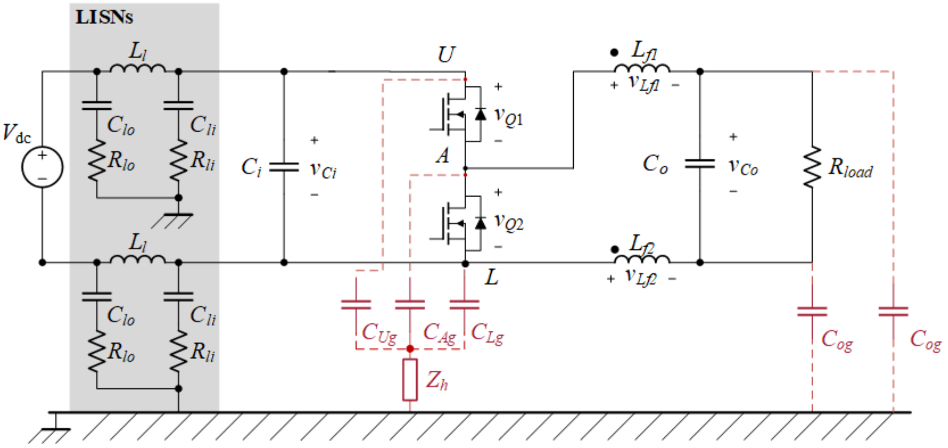

Figure 46. MM model for practical buck converter

5.2.1.1. GaN Development Board

The practical buck converter implementation is based on the GaN Systems GS66508T-EVBDB evaluation module shown in Figure 47(a) [41]. This board contains two 650 V GS66508T enhancement-mode HEMTs along with gate drive circuitry and isolated power supplies. This PCB is intended to be paired with the GaN Systems GS665MB-EVB Universal Motherboard, which acts as an evaluation system [41]. However, the Universal Motherboard is not well-suited for the validation of the practical buck converter CEM because the filter inductor is fixed in the upper rail of this system. This configuration precludes evaluation of the asymmetry factor that is the principal degree of freedom considered in this thesis. Therefore, a custom PCB was designed and fabricated to meet the requirements of this testing. Specifically, the PCB design of the GS665MB-EVB Universal Motherboard was modified to accommodate a symmetric filter inductor configuration by introducing inductor contacts in both the upper and lower rails. The final populated PCB is shown in Figure 47(b).

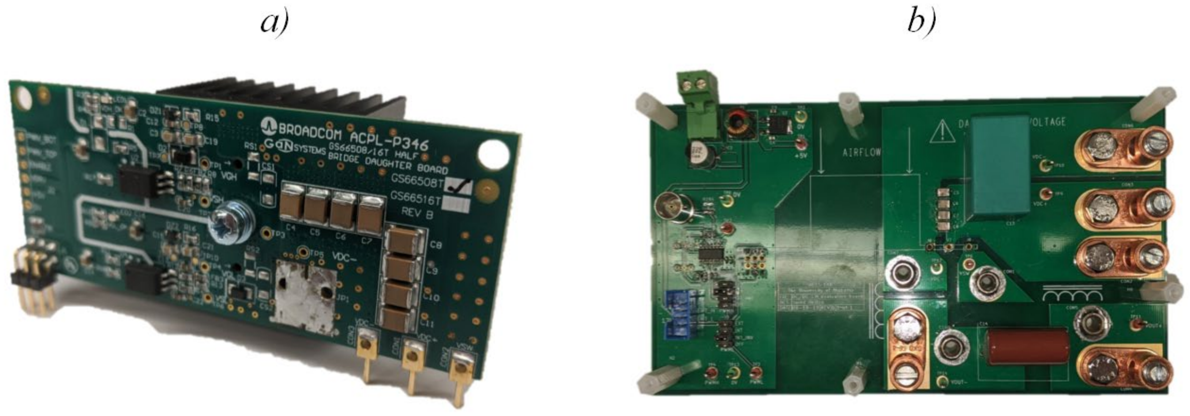

Figure 47. (a) GS66508T-EVBDB Daughter Board and (b) customized universal motherboard PCB

5.2.1.2. LISNs

The first significant component of the high-power experimental setup is the LISNs. The inclusion of LISNs is designed to emulate the implementation of a fielded system with non-negligible coupling to the grounded enclosure or chassis. The LISNs also provide a reference impedance to the ground plane that is used as the measurement location for conducted emissions compliance testing such as that defined in MIL-STD-461 CE102 [5]. The hardware realization of the LISNs utilized in this phase of the experimental procedures is shown in Figure 48.

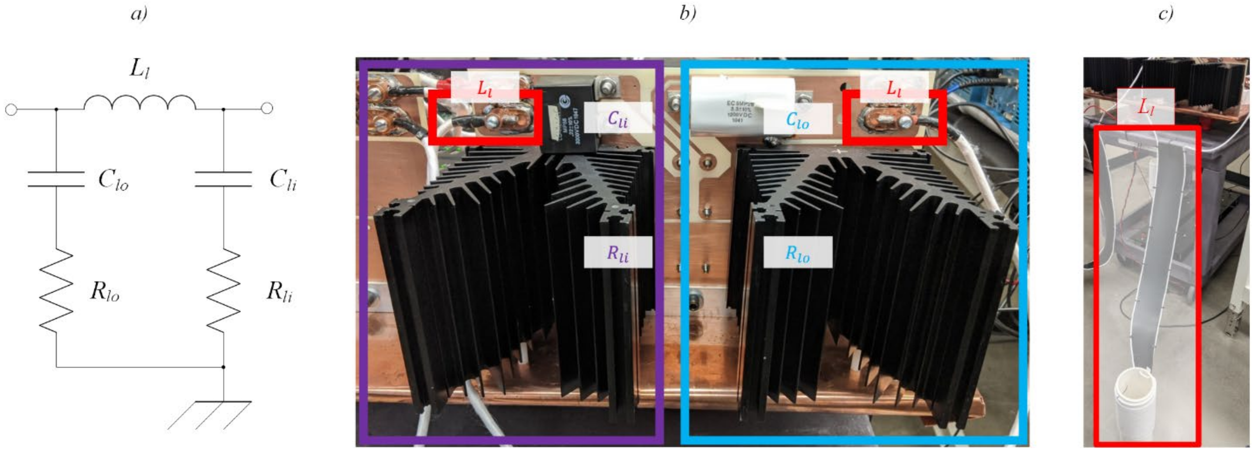

Figure 48. (a) Circuit representation of LISNs (b) physical configurations of LISNs and (b) LISN Inductor

5.2.1.3. Inductor Load Bank

The second significant component of the high-power experimental setup is the filter inductor bank. This custom inductor bank was designed for low equivalent series resistance (ESR) and low equivalent parallel capacitance (EPC) in order to approximate consistent inductance across the frequency of interest [26]. The impedance of the inductor bank was characterized using an impedance analyzer in order to provide parameters for populating the CEM. The total inductance of the bank is 140 μH, and the ESR and EPC of the bank are 145 mΩ and 0.19 pF, respectively. It should be noted that the inductor bank consists of ten series-connected elements of the type shown in Figure 49(a). The entire bank is divided into two groups of five elements apiece. Each group of elements are mounted to a single plastic panel as shown in Figure 49(b). It should be noted that these panels can be linked in series and inserted into a single rail of the converter to establish either of the asymmetric configurations ($a = 1, a = -1$). One the other hand, these two panels can be separated and inserted individually into the two rails of the converter to establish the symmetric configuration ($a = 0$).

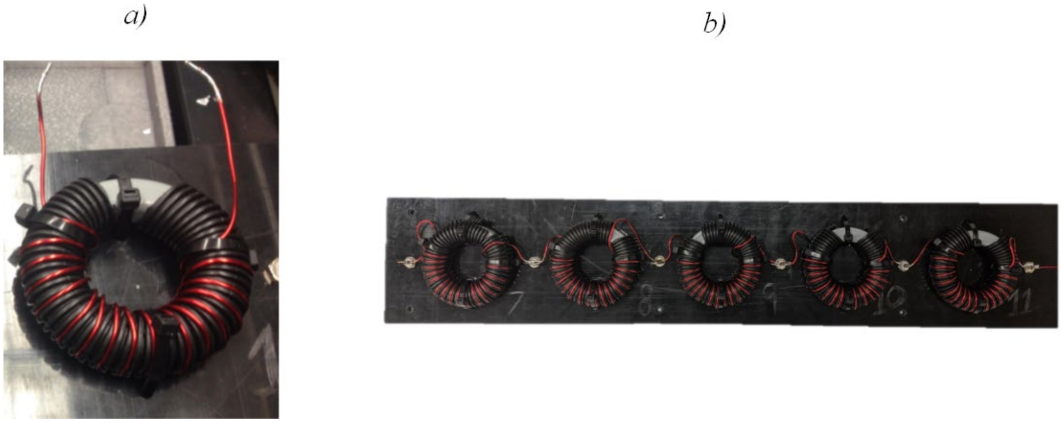

Figure 49. (a) Single core and (b) single panel of inductor bank

5.2.1.4. Capacitive Coupling of the Load

The third significant component of the high-power experimental setup is the capacitive coupling of the load. This coupling was implemented by connecting physical capacitors between the terminals of the load and the ground plane. These capacitors are physically mounted on two PCBs attached to the ground plane as shown in Figure 50. For this setup, one capacitor with a value of 0.22 µF is mounted on each terminal of the load. Electronic Concepts PT88BL224B capacitors with ESR of 2 mΩ are used to implement the load coupling [43].

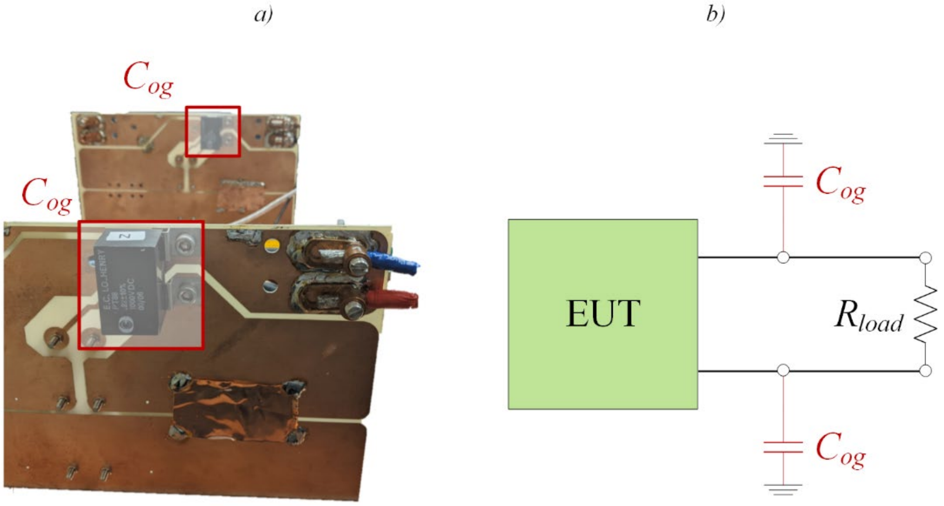

Figure 50. (a) Physical connection and (b) schematic representation for C_{og}

5.2.2. Testing Procedure

The procedure for operating the high-power test stand and processing the experimental results is described in this section. The operating conditions employed for these experiments are detailed in Table 10. The complete experimental setup is shown in Figure 51. The LISNs, EUT, and load capacitance are highlighted in Figure 51(a). The filter inductor banks are located below the testbed as shown in Figure 51(b). The testing procedure is divided into two cases. The first case is the asymmetric filter inductor configuration. This case is realized by inserting the entire inductor bank into the upper rail of the converter. The second case is the symmetric filter inductor configuration. This case is realized by separating the elements of the inductor bank and inserting one half in the upper rail and one half in the lower rail.

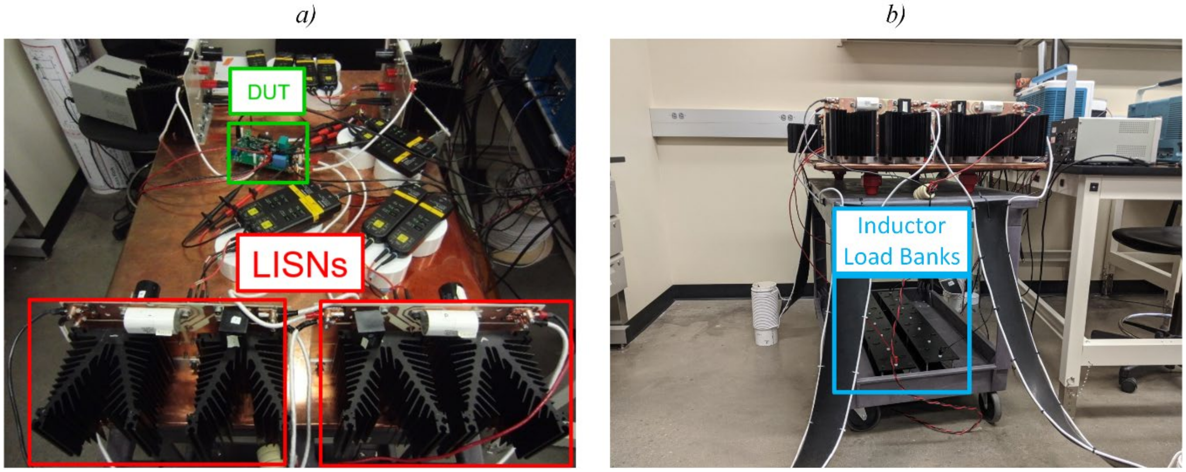

Figure 51. (a) Test setup and (b) inductor load bank

TABLE 10
PARAMETERS FOR TESTING OF LOW-POWER TEST SETUP

Parameters		Values		Units
		Case 1	Case 2	
		LISNs		
R_{li}	Inboard resistor	1000	~	Ω
R_{lo}	Outboard resistor	5	~	Ω
C_{li}	Inboard capacitor	0.22	~	μF
C_{lo}	Outboard capacitor	8	~	μF
L_l	Input inductor	50	~	μH
		EUT		
V_{dc}	Input voltage	200	~	V
C_o	Output capacitance	0.1	~	μF
C_i	Input capacitance	10	~	μF
f_{sw}	Switching frequency	250	~	kHz
d	Duty cycle	0.5	~	
R_{load}	Load resistor	50	~	Ω
C_{og}	Capacitive coupling of load	220	~	nF
		Filter Inductors		
L_f	Filter Inductance	140	60	μH
a	Asymmetry factor	1	0	
m	Mutual coupling	0	~	

The results of these experiments are used to evaluate the accuracy of the practical buck converter CEM. The quantities measured in the experimental setup include three MM voltages and a single CM current. The three voltages are indicated in Figure 46: the input voltage, v_{Ci}; the lower switch voltage, v_{Q2}; and the output voltage, v_{Co}. These MM voltage measurements are used to generate the CM voltage signals needed to populate the CEM. The CM current is measured by simultaneously measuring the upper and lower rail currents with a single current probe on the output of the system. The location within the system where this measurement is performed is highlighted in Figure 46. The CM current measurement is utilized as the reference data for comparison with the predictions of the CEM.

The model is populated by using the measured MM voltages to compute the CM voltage source, and by generating a transfer function to represent the CM impedance. The time-domain measurements are converted to the frequency-domain using the FFT function within MATLAB. The measured voltages are combined to represent the final CM voltage source by utilizing Equation (*70*). It is noted that the CM voltage source for this setup includes a frequency dependent term that is defined in Section 4.2.2.1. The transfer function for the CM impedance is formulated by combining the frequency-domain representation of each element in the CEM. The practical buck converter CEM is shown in Figure 52. The total CM impedance is calculated with Equation (*69*). The final step in generating the modeled CM current is completed by dividing the CM voltage by the CM impedance.

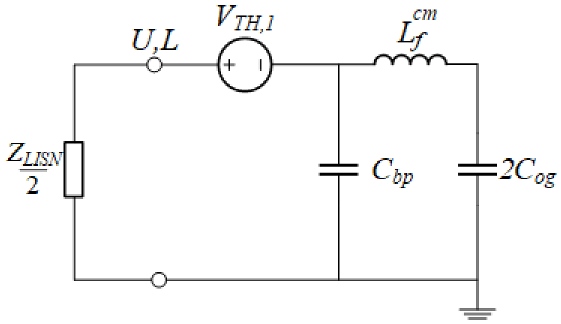

Figure 52. CEM for the high-power buck converter

5.2.3. Metrology

The metrology used to measure the quantities of interest in the low-power test setup is described in this section. The MM voltages are measured using Tektronix THDP0200 differential probes, which have a bandwidth of 200 MHz [36]. For all experiments described here, the differential probes were configured in the low-voltage range setting (150 V) for improved resolution. The CM current was measured using a Tektronix TCP0030A current probe, which has a bandwidth of 120 MHz [37]. The probe was configured in the low-current range setting (5 A) for improved resolution. All measured signals were monitored and recorded using a Tektronix MDO4104B-3 oscilloscope, which has a bandwidth of 500 MHz [38].

5.2.4. Model Comparison

This section presents a comparison of the predictions from the practical buck converter CEM and the measured behavior of the high-power experimental setup. The initial comparisons performed for this setup exposed substantial disagreement between the model predictions and the experimental measurements. This disagreement revealed characteristics of the experimental setup that were not modeled in the CEM. Following the procedure outlined in Section 4.2.2, the CEM was updated to include the parameters needed to satisfactorily explain the experimentally observed behavior. Therefore, this section is split into three subsections. The first section provides the initial model comparison and discusses the challenges involved. The second section details the updates to the CEM to better represent the experimental system. The third section provides the updated model comparison.

5.2.4.1. Initial Results

The initial comparison between the experimental measurements and the predictions of the CEM for the practical buck converter is described in this section. The process outlined in Section 5.2.2 was followed to obtain the experimental results needed for this comparison. Similar to Section 5.1.4, the system was evaluated in two configurations: an asymmetric filter inductor configuration with $a = 1$, and a symmetric filter inductor configuration with $a = 0$. A comparison of the model prediction and empirical measurements is shown in Figure 53(a) for the asymmetric configuration and in Figure 53(b) for the symmetric configuration. The basis of both comparisons is the CM current evaluated at the input of the system. The model developed in Section 4.2.2 defined the analytical model with respect to the input side of the system.

Therefore, the measurement is made on the input to permit a direct comparison. It is noted that the magnitude of the CM output current in Figure 53 is much higher than the results shown in Section 5.1.4 for the low-power experimental setup. This difference is expected due to the higher voltages utilized in the high-power experimental setup. The symmetric configuration shown in Figure 53(b) demonstrates substantially higher CM current magnitude at the switching frequency and harmonics compared to the asymmetric configuration shown in Figure 53(a). This trend is predicted by the analysis in the previous chapter. Figure 53 also demonstrates good agreement between the model prediction and measured results at the fundamental frequency and first few first harmonics. However, the model agreement degrades quickly at frequencies above 1 MHz in both cases. This disagreement indicates that there are critical elements in the physical system that are not adequately represented in the CEM.

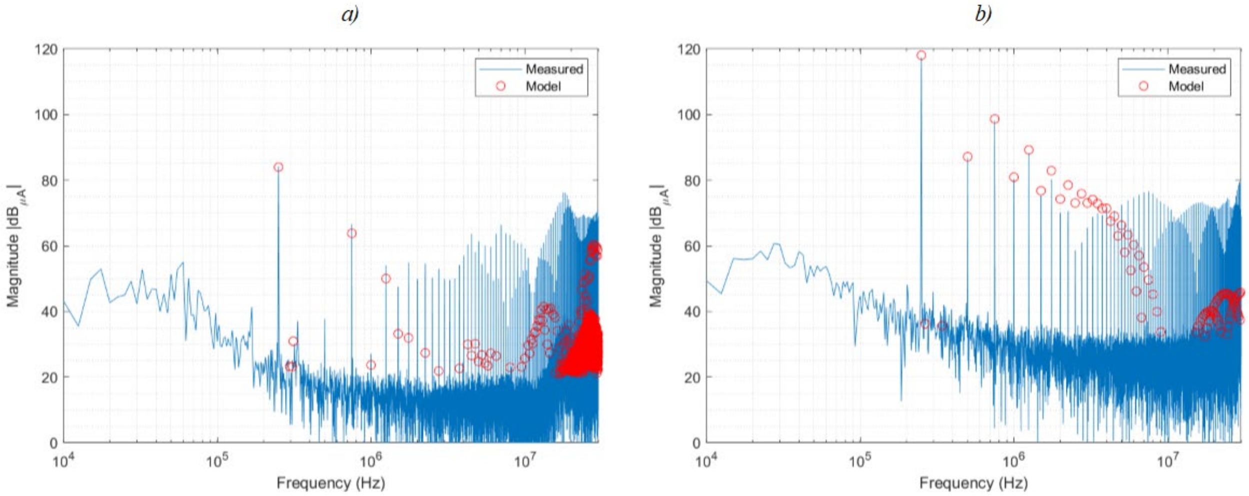

Figure 53. Comparison between the CEM prediction and empirical measurements of input CM current for (a) asymmetric and (b) symmetric filter inductor configuration for practical buck converter

5.2.4.2. Updated CEM

The model disagreement shown in Figure 53 suggests that there are critical elements in the physical system that are not represented in the CEM. In previous studies, such missing elements have usually turned out to be small parasitic couplings between various system elements and the ground plane. However, the model used for the LISNs in this system were validated in a previous study [24]; therefore, the LISNs were considered unlikely to be the cause of this discrepancy.

On the other hand, the model of the output load and associated couplings used in this study has not been previously validated. In order to properly configure this portion of the CEM, the CM impedance between the output side of the converter and the system ground plane was characterized using a Keysight E4990A precision impedance analyzer [39] and a Keysight 42941A impedance probe [40]. This measurement was performed by physically detaching the inductor leads from the converter, attaching the ends of these leads together, and measuring the impedance between this node and the testbed grounding plane. The output impedance characterization revealed significant capacitive coupling to the ground plane. This is demonstrated by the high-frequency roll-off of the measured impedance magnitude shown in Figure 54. Note that the original CM impedance model for the output section of the system is shown as the "nominal" case in Figure 54, which does not include a magnitude roll-off at high frequency.

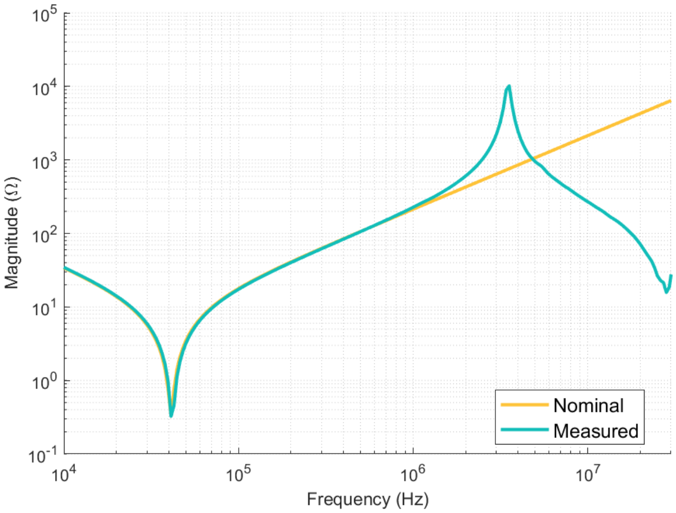

Figure 54. Comparison of nominal and measured CM output impedance

The origin of this parasitic capacitive coupling was identified as originating from the connection of the filter inductors to the EUT. This connection consists of wire leads that pass by the ground plane. Figure 55 shows the routing of these wire leads in the physical system. The proximity of these wire leads to the ground plane provides a shunt path that allows CM current to bypass the filter inductors at high frequencies.

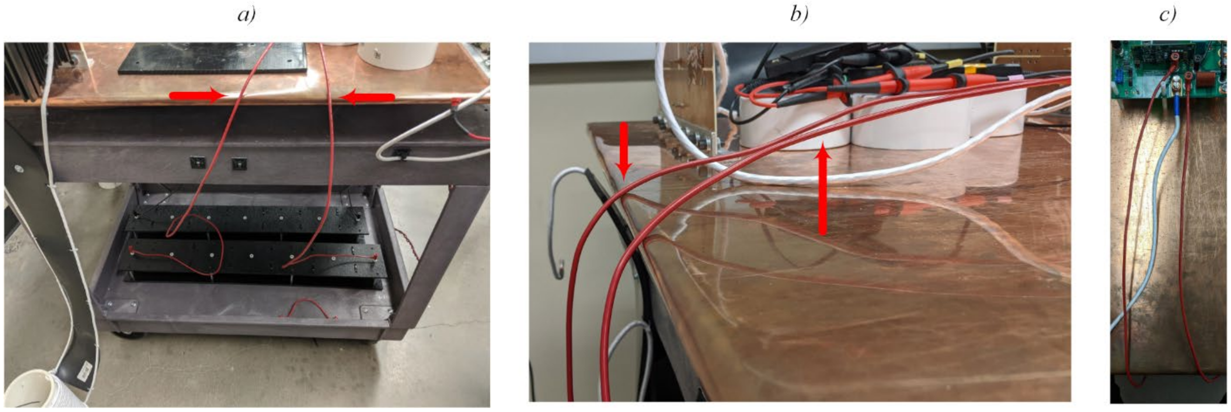

Figure 55. Path of the filter inductor leads (a) from load bank (b) around ground plane (c) over grounding plane to EUT

The model of the output impedance was updated to include the characterized coupling between the inductor leads and the ground plane. The updated CEM is shown in Figure 54(a). The updated elements in the impedance model are shown in red. The element C_p represents the coupling between the inductor leads and the ground plane. The element EPR represents the core loss of the inductor elements, which was tuned to achieve the impedance model agreement shown in Figure 56(b). The values estimated for elements C_p and EPR are 60 pF and 10 kΩ, respectively. Figure 56(b) demonstrates the improved agreement between the measured and modeled CM impedance at high frequency. The impedance above ~2 MHz is dominated by the parasitic capacitance between the filter inductor leads and the ground plane. It is noted that this corresponds directly to the frequencies where the model mismatch is observed in Figure 53(b).

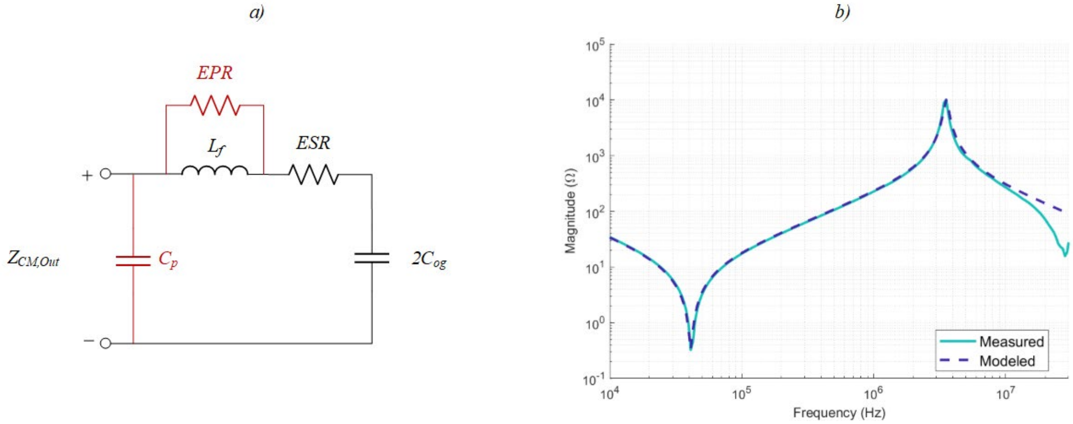

Figure 56. (a) Updated CEM and (b) comparison between measured and modeled CM output impedance

5.2.4.3. Final Results

The updated CM impedance model shown in Figure 56(a) was integrated into the CEM of the practical buck converter in order to improve the high-frequency fidelity of the model. A comparison of the model prediction and empirical measurements is shown in Figure 57(a) for the asymmetric configuration and in Figure 57(b) for the symmetric configuration. The basis of both comparisons is the CM current evaluated at the input of the system. As mention in Section 5.2.2, the analysis is valid on the input side of the system due to the means in which the analytical CEM was developed in Section 4.2.2. The updated model demonstrates improved agreement with the experimental results across the entire frequency spectrum. The symmetric configuration demonstrates good fidelity up to 30 MHz, which is similar to the agreement achieved for the low-power experimental setup. The agreement of the asymmetric configuration shown in Figure 57(a) is also significantly improved compared to the original comparison shown in Figure 53(a), although some discrepancies are observed above 2 MHz. Figure 57 also corroborates the trends predicted by analysis of the CEM in Section 4.2.2. Specifically, the asymmetric filter inductor configuration provides a reduced CM emissions envelope for the switching frequency and harmonics compared to the symmetric configuration when C_{og} is much larger than C_{bp}.

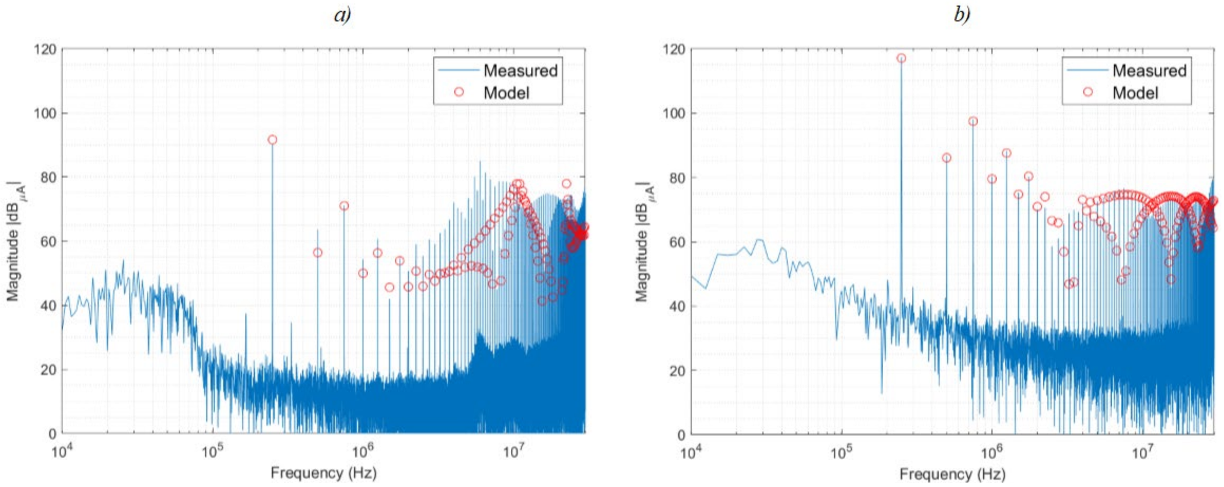

Figure 57. Comparison of measured and modeled input CM currents for (a) asymmetric and (b) symmetric filter inductor configurations for the practical buck converter

It is noted that quantitatively assessing the agreement between the empirical and modeled results shown in Figure 57 proves challenging. A common metric used to provide such assessment is the normalized root-mean-square (RMS) error. Since the comparisons shown in Figure 57 are plotted on a logarithmic scale, the high-frequency results have much greater influence over RMS error than the low-frequency results. However, model accuracy is usually more important for the switching frequency and its first few harmonics than for the high-frequency regime (above 10 MHz). Therefore, to provide a more useful assessment of model accuracy, the difference in magnitude peaks between the switching frequency and the 10th harmonic is utilized as a figure of merit herein. Table 11 presents a synopsis of these error values for both the initial (Figure 53) and updated (Figure 57) comparisons, for both the asymmetric ($a = 1$) and symmetric ($a = 0$) filter inductor configurations. Table 11 shows that the average error for the updated comparison is reduced by approximately 15 dB for the asymmetric case, and by approximately 1.5 dB for the symmetric case, compared to the initial comparison. This reduction in error is particularly significant for the results near the 10th harmonic. The assessment given in Table 11 provides a quantitative metric that demonstrates the improvement in model agreement from the initial comparison shown in Figure 53 to the updated comparison shown in Figure 57.

TABLE 11

MAGNITUDE ERROR FOR PRACTICAL BUCK CONVERTER

Frequencies	Initial comparison (dB) ($a = 1$)	Initial comparison (dB) ($a = 0$)	Updated comparison (dB) ($a = 1$)	Updated comparison (dB) ($a = 0$)
f_{sw}	0.99	0.30	1.33	0.30
$2f_{sw}$	30.68	0.55	7.24	0.68
$3f_{sw}$	0.20	0.33	0.12	0.64
$4f_{sw}$	23.57	0.15	4.36	0.72
$5f_{sw}$	6.16	0.21	4.34	0.70
$6f_{sw}$	15.00	0.92	3.72	0.46
$7f_{sw}$	22.42	2.14	0.76	0.11
$8f_{sw}$	32.34	3.82	4.99	0.89
$9f_{sw}$	24.94	7.69	8.55	3.41
$10f_{sw}$	37.88	14.32	9.48	7.88
Average Error				
~	19.42	3.04	4.49	1.58

5.3. Experimental Comparison Analysis

Comparing the two experimental configurations explored in this chapter provides additional insight into the CM behavior of the buck converter. The low-power experimental setup represents an idealized system that isolates the CM behavior of the converter topology from its environment. Nevertheless, the comparison presented in Section 5.1.4 revealed analysis assumptions that were not valid even for this simplified case. The assumptions utilized to derive the CEM were modified accordingly, and this approach was also utilized in the evaluation of the practical buck converter CEM. The high-power experimental setup represents the practical implementation of a fielded system. The comparisons presented in Section 5.2.4 highlight the likelihood of undesired coupling paths in a fielded system and their impact on CM behavior. Analyzing these two experimental configurations leads to an improved understanding of the interaction between the converter and its environment.

Additionally, it should be noted that the results shown in Figure 44 and Figure 57 reflect the influence of alterations to the experimental setup made specifically to emphasize the CM behavior of the system. It is shown in Section 4.1.1.1 that the total CM voltage source for the buck topology is a function of switch voltages for the symmetric filter inductor case and a function of capacitor voltage ripple for the asymmetric filter inductor case. Measurement of the symmetric configuration is straightforward due to the substantial emissions profile generated by the switch voltages. On the other hand, the emissions signature for the asymmetric filter inductor configuration is more difficult to measure accurately because a well-designed dc-dc converter minimizes the magnitude of the capacitor voltage ripple. Thus, the comparisons shown in Figure 44 and Figure 57 include the influence of decreasing the size of the filter capacitor to increase the ac component of the output voltage. While this change degrades the DM performance of the converter under study, it is nevertheless necessary to amplify the emissions signature of this system so that a valid assessment of model accuracy can be performed. The necessity of this change also further highlights the improvement that an asymmetric filter inductor configuration provides for this converter topology.

CHAPTER 6:

CONCLUSION

This thesis describes a comprehensive and rigorous approach for modeling the CM behavior of dc-dc converters. CEMs are provided for four different dc-dc converter configurations: (1) a simplified boost converter; (2) a simplified buck converter; (3) a practical boost converter; and (4) a practical buck converter. Each of these models are analyzed using common circuit techniques to provide insight into the parameters that govern their CM behavior. The simplified models for both topologies are shown to behave in the same manner regardless of topology. Analysis of the simplified models reveals that the asymmetric configuration with the filter inductance concentrated in the upper rail provides the lowest CM emissions for both topologies.

On the other hand, analysis of the practical models reveals distinct behavior for the two topologies. The practical boost converter is shown to benefit from a symmetric filter inductor configuration. This finding is consistent with the existing literature regarding the CM behavior of the boost converter. On the other hand, the practical buck converter is shown to benefit in terms of CM emissions from an asymmetric configuration with the filter inductance concentrated in the upper rail. Both considered configurations of the buck converter CEM were also experimentally validated as part of this research. The simplified buck CEM was validated utilizing a low-power experimental setup that permits the topology to be evaluated independent from its environment. The practical buck CEM was validated with a high-power experimental setup that includes features commonly found in a fielded system, and which is representative of a compliance setup for conducted emissions.

Overall, this thesis demonstrates similarity in CM behavior between the buck and boost topologies for the simplified models, but divergent behavior between the buck and boost topologies for the practical models. The similarity in CM behavior observed for the simplified models is not surprising, given the similarity of the two topologies. On the other hand, the difference in CM behavior for the practical models of these two similar topologies is an unexpected outcome. Indeed, the two converter topologies are shown to demonstrate opposite dependence on filter inductor asymmetry with respect to CM emissions. The CM emissions of the boost converter are minimized for the symmetric inductor case, while the CM emissions of the buck converter are maximized for the symmetric inductor case. It is noted that the opposing CM behavior of these two topologies is linked to the influence of the module baseplate capacitance, which is a common parasitic element in high-power, fielded converter systems. Thus, this divergent CM behavior for the buck and boost topologies is expected to be the rule rather than the exception in practical power electronics systems. The CM modeling approach detailed in this thesis is able to capture and predict this unexpected behavior. This is true not only in a qualitative sense, but also in a quantitative sense as demonstrated by the empirical comparisons provided herein. Thus, the modeling approach presented in this thesis is expected to be a powerful tool for identifying the dominant CM behavior of dc-dc converters and discovering new means for the suppression of undesired emissions in these systems.

6.1. Future Work

The process defined in this thesis provides a good starting point for understanding CM modeling. However, the complexity of the system requires some simplification to aid understanding of the CM behavior for the systems under consideration. This thesis focuses on the filter inductor asymmetry and its effect on CM behavior. However, there are other influential terms in dc-dc converter systems that are not considered here. For example, the mutual coupling factor for the filter inductors is set to zero to simplify the analysis in this thesis. This factor can be utilized in combination with the filter inductor asymmetry to further reduce emissions. Additionally, the analysis in Chapter 4 that includes the BPC elements is minimally used in the experimental validation. The three distinct elements of the BPC provide degrees of freedom that can be leveraged to deterministically eliminate CM voltage sources. For example, this thesis identified a configuration of BPC elements that theoretically eliminates the CM voltage source for both considered topologies. This analysis provides an opportunity to implement and validate the proposed cancellation techniques. The same modeling tools can be used to evaluate the impact of the frequency-dependent CM voltage source term for the buck converter. The boost converter CEM includes CM voltage sources that are frequency independent. However, analysis of the buck converter by the frequency-dependence of its CM voltage source terms. In this thesis, the frequency-dependent term was treated in a piecemeal fashion by analyzing only two specific cases. This presents an opportunity to generalize the frequency-dependence of the buck converter such that more complex analysis can be performed.

There is also ample opportunity to experimentally validate the CEM for the various configurations of the boost converter. The buck converter was modeled and experimentally validated in this thesis, but the boost converter model was only qualitatively validated by comparisons to literature [13]. Experimentally validating the boost converter CEM would provide additional confidence in the CM models presented in this thesis. Analysis of additional terms beyond the filter inductor asymmetry can be also performed for the boost converter topology. For example, the CEM can be leveraged to identify configurations of the BPC that eliminate the CM voltage source. Additionally, the boost converter CEM can be leveraged to evaluate the impact of the load capacitance on the CM behavior of the rest of the system. There is also an opportunity to evaluate whether the asymmetric configuration of the practical boost converter can be configured in a manner that leverages other system parameters to provide CM emissions reduction.

REFRENCES

[1] N. Mohan, *Power Electronics: A First Course,* 1st Ed, John Wiley & Sons, 2011.

[2] A. J. Hanson and D. J. Perreault, "A High-Frequency Power Factor Correction Stage with Low Output Voltage," in *IEEE Journal of Emerging and Selected Topics in Power Electronics*.

[3] C. Paul, *Introduction to Electromagnetic Compatibility*, 2nd Ed, John Wiley & Sons, 2008

[4] N. Oswald, B. H. Stark, D. Holliday, C. Hargis and B. Drury, "Analysis of Shaped Pulse Transitions in Power Electronic Switching Waveforms for Reduced EMI Generation," in *IEEE Transactions on Industry Applications*, vol. 47, no. 5, pp. 2154-2165, Sept.-Oct. 2011.

[5] *Department of Defense Interface Standard: Requirements for the control of electromagnetic interference characteristics of subsystems and equipment,* MIL-STD-461G, 2015.

[6] Y. Koyama, M. Tanaka, and H. Akagi, “Modeling and Analysis for Simulation of Common-Mode Noises Produced by an Inverter-Driven Air Conditioner,” IEEE Trans. Ind. Appl., vol. 47, no. 5, pp. 2166-2174, Sep. 2011.

[7] A. Muetze and A. Binder, “Calculation of Motor Capacitances for Prediction of the Voltage Across the Bearings in Machines of Inverter-Based Drive Systems,” IEEE Trans. Ind. Appl., vol. 43, no. 3, pp. 665–672, May 2007.

[8] A. Julian, G. Oriti, and T. Lipo, “Elimination of common-mode voltage in three-phase sinusoidal power converters.” IEEE Trans. Power Electron., vol. 14, no. 5, pp. 982-989, Sep. 1999.

[9] S. Chen, T. Lipo, and D. Fitzgerald, “Source of induction motor bearing currents caused by PWM inverters,” IEEE Trans. Energy Convers., vol. 11, no. 1, pp. 25–32, Mar. 1996.

[10] S. Mastuhisa, E. Ikuta and T. Shimizu, "Common-mode EMI reduction method and filter configuration for equipment without grounding," IECON 2017 - 43rd Annual Conference of the IEEE Industrial Electronics Society, Beijing, 2017, pp. 7006-7011.

[11] S. Ogasawara and H. Akagi, “Modeling and damping of high-frequency leakage currents in PWM inverter-fed AC motor drive systems,” IEEE Trans. Ind. Appl., vol. 32, no. 5, pp. 1105–1114, Sep. 1996.

[12] D. Busse, J. Erdman, R. Kerkman, D. Schlegel, and G. Skibinski, “Bearing currents and their relationship to PWM drives,” IEEE Trans. Power Electron., vol. 12, no. 2, pp. 243–252, Mar. 1997.

[13] S. Wang, P. Kong and F. C. Lee, "Common Mode Noise Reduction for Boost Converters Using General Balance Technique," in IEEE Transactions on Power Electronics, vol. 22, no. 4, pp. 1410-1416, July 2007.

[14] M. Shoyama, Ge Li and T. Ninomiya, "Balanced switching converter to reduce common-mode conducted noise," in IEEE Transactions on Industrial Electronics, vol. 50, no. 6, pp. 1095-1099, Dec. 2003.

[15] Wu Xin, N. K. Poon, C. M. Lee, M. H. Pong and Zhaoming Qian, "A study of common mode noise in switching power supply from a current balancing viewpoint," Proceedings of the IEEE 1999 International Conference on Power Electronics and Drive Systems. PEDS'99 (Cat. No.99TH8475), Hong Kong, 1999, pp. 621-625 vol.2.

[16] Liyu Yang et al., "Modeling and characterization of a 1 KW CCM PFC converter for conducted EMI prediction," Nineteenth Annual IEEE Applied Power Electronics Conference and Exposition, 2004. APEC '04., Anaheim, CA, USA, 2004, pp. 763-769 vol.2.

[17] A. Rockhill, T. A. Lipo and A. L. Julian, "High voltage buck converter topology for common mode voltage reduction," APEC '98 Thirteenth Annual Applied Power Electronics Conference and Exposition, Anaheim, CA, USA, 1998, pp. 940-943 vol.2.

[18] K. Nomura, T. Kojima, A. Takahashi, Y. Hattori and K. Torii, "Conducted common mode noise reduction for boost converters using leakage inductance of coupled inductor," 2017 IEEE Applied Power Electronics Conference and Exposition (APEC), Tampa, FL, 2017, pp. 294-299.

[19] P. Kong, S. Wang and F. C. Lee, "Common Mode EMI Noise Suppression for Bridgeless PFC Converters," in IEEE Transactions on Power Electronics, vol. 23, no. 1, pp. 291-297, Jan. 2008.

[20] Wu Xin, M. H. Pong, Z. Y. Lu and Z. M. Qian, "Novel boost PFC with low common mode EMI: modeling and design," APEC 2000. Fifteenth Annual IEEE Applied Power Electronics Conference and Exposition (Cat. No.00CH37058), New Orleans, LA, USA, 2000, pp. 178-181 vol.1.

[21] A. Boyer, M. A. G. Sentis, C. Ghfiri and A. Durier, "Modeling methodology of the conducted emission of a DC-DC converter board," 2017 11th International Workshop on the Electromagnetic Compatibility of Integrated Circuits (EMCCompo), St. Petersburg, 2017, pp. 73-78.

[22] A. D. Brovont and R. M. Cuzner, "DM and CM Modeling of Non-Isolated Buck Converters for EMI Filter Design," 2018 IEEE Transportation Electrification Conference and Expo (ITEC), Long Beach, CA, 2018, pp. 140-145.

[23] A. D. Brovont, "Generalized Differential-Common-Mode Decomposition for Modeling Conducted Emissions in Asymmetric Power Electronic Systems," in IEEE Transactions on Power Electronics, vol. 33, no. 8, pp. 6461-6466, Aug. 2018.

[24] A. Lemmon, A. D. Brovont, C. D. New, B. W. Nelson and B. T. DeBoi, "Modeling and Validation of Common-Mode Emissions in Wide-Bandgap-Based Converter Structures," in *IEEE Transactions on Power Electronics*.

[25] *Automated State Model Generator Toolbox for Simulink,* PC Krause Associates, West, Lafayette, IN, USA, 2019.

[26] B.W. Nelson, “SPICE modeling and simulation of silicon-carbide power modules,” M.S. thesis, Department of Electrical Engineering, Tuscaloosa, AL, USA, 2017.

[27] D. Han, S. Li, W. Lee, W. Choi and B. Sarlioglu, "Trade-off between switching loss and common mode EMI generation of GaN devices-analysis and solution," *2017 IEEE Applied Power Electronics Conference and Exposition (APEC)*, Tampa, FL, 2017, pp. 843-847.

[28] Shahabi, Ali, “A Controlled Buck Converter: Design and Empirical Implementation,” 2016.

[29] Fairchild Semiconductor, “FQP11P06”, datasheet, November 2013.

[30] Fairchild Semiconductor, “SB580-D”, datasheet, 2001.

[31] Fairchild Semiconductor, “KSP2222A-D”, datasheet, November 2014.

[32] TDK, “FG26X5R1E476MRT06”, datasheet, November 2018.

[33] KEMET, “C315C100J2G5TA”, datasheet, January 2019.

[34] Murata, “19R683C”, datasheet, 2011.

[35] Nichicon, “UVR2C010MED”, datasheet.

[36] Tektronix, “THDP0200 1500 V High-Voltage Probe”, datasheet, April 2019.

[37] Tektronix, “30 A AC/DC Current Probe”, TCP0030A datasheet, August 2017.

[38] Tektronix, “MDO4104B-3 Mixed Domain Oscilloscope”, datasheet, February 2015.

[39] Keysight Technologies, “E4990a Impedance Analyzer 20 Hz to 10/20/30/50/120 MHz,” 5991-3890EN datasheet, November 2018.

[40] Keysight Technologies, “Keysight 42941A Impedance Probe Kit” 42941-90010 datasheet, November 2019.

[41] GaN Systems, “GS66508T User Manual”, 2020.

[42] GaN Systems, “Design with GaN Enhancement Mode HEMT”, GN001 Application Guide, 2020.

[43] Electronic Concepts, “PT88BL224B Datasheet”, datasheet.

[44] E. A. Jones, F. F. Wang and D. Costinett, "Review of Commercial GaN Power Devices and GaN-Based Converter Design Challenges," in *IEEE Journal of Emerging and Selected Topics in Power Electronics*, vol. 4, no. 3, pp. 707-719, Sept. 2016.

[45] F. Wang, Z. Zhang, and E. Jones, *Characterization of Wide Bandgap Power Semiconductor Device,* London, United Kingdom, IET, 2018.

[46] A. D. Brovont and A. N. Lemmon, "Common-mode/differential-mode interactions in asymmetric converter structures," *2017 IEEE Electric Ship Technologies Symposium (ESTS)*, Arlington, VA, 2017, pp. 84-90.

[47] A. D. Brovont and S. D. Pekarek, "Derivation and Application of Equivalent Circuits to Model Common-Mode Current in Microgrids," in *IEEE Journal of Emerging and Selected Topics in Power Electronics*, vol. 5, no. 1, pp. 297-308, March 2017.

APPENDIX

A.1. CM Decomposition of LISNs

Resolving the CM equivalent relationship for the LISNs is detailed in this section. This is achieved by performing a KVL loop that starts at the reference point P, follows a path through the LISNs and returns through the testbed ground as indicated in Figure 9(b). This relationship is established in Equation (*76*):

$$-v_{Pg}\begin{bmatrix}1\\1\end{bmatrix}-\begin{bmatrix}v_{1P}\\v_{2P}\end{bmatrix}+\begin{bmatrix}v_{LISN,1}\\v_{LISN,2}\end{bmatrix}=0 \tag{76}$$

Isolating the LISN voltages produces Equation *(77)*:

$$v_{Pg}\begin{bmatrix}1\\1\end{bmatrix}+\begin{bmatrix}v_{1P}\\v_{2P}\end{bmatrix}=\begin{bmatrix}v_{LISN,1}\\v_{LISN,2}\end{bmatrix} \tag{77}$$

The next step is to left-multiply both sides of Equation *(77)* by the T_v^2 definition in Equation *(3)* to represent the voltages established by the KVL loop in their decomposed DM and CM equivalent relationships. This produces Equation *(78)*:

$$T_v^2 v_{Pg}\begin{bmatrix}1\\1\end{bmatrix}+T_v^2\begin{bmatrix}v_{1P}\\v_{2P}\end{bmatrix}=T_v^2\begin{bmatrix}v_{LISN,1}\\v_{LISN,2}\end{bmatrix} \tag{78}$$

Substituting Equation (*7*) for $\begin{bmatrix}v_{LISN,1}\\v_{LISN,2}\end{bmatrix}$ produces Equation *(79)*:

$$T_v^2 v_{Pg}\begin{bmatrix}1\\1\end{bmatrix}+T_v^2\begin{bmatrix}v_{1P}\\v_{2P}\end{bmatrix}=T_v^2\begin{bmatrix}Z_{LISN} & 0\\0 & Z_{LISN}\end{bmatrix}\begin{bmatrix}i_1\\i_2\end{bmatrix} \tag{79}$$

It is also necessary to substitute $(T_i^2)^{-1}\begin{bmatrix}i_{dm}\\i_{cm}\end{bmatrix}$ for the LISN currents $\begin{bmatrix}i_1\\i_2\end{bmatrix}$ in order to represent them in their DM and CM equivalent relationships. Substituting this relationship into Equation *(79)* produces Equation *(80)*:

$$T_v^2 v_{Pg}\begin{bmatrix}1\\1\end{bmatrix}+T_v^2\begin{bmatrix}v_{1P}\\v_{2P}\end{bmatrix}=T_v^2\begin{bmatrix}Z_{LISN} & 0\\0 & Z_{LISN}\end{bmatrix}(T_i^2)^{-1}\begin{bmatrix}i_{dm}\\i_{cm}\end{bmatrix} \tag{80}$$

By Equation *(1)*, $T_v^2\begin{bmatrix}v_{1P}\\v_{2P}\end{bmatrix}$ is equivalent to $\begin{bmatrix}v_{dm}\\v_{cm}\end{bmatrix}$. Substituting this representation into Equation *(80)* and expressing T_v^2 and $(T_i^2)^{-1}$ in explicit form produces Equation *(81)*:

$$v_{Pg}\begin{bmatrix}1 & -1\\1/2 & 1/2\end{bmatrix}\begin{bmatrix}1\\1\end{bmatrix}+\begin{bmatrix}v_{dm}\\v_{cm}\end{bmatrix}=\begin{bmatrix}1 & -1\\1/2 & 1/2\end{bmatrix}\begin{bmatrix}Z_{LISN} & 0\\0 & Z_{LISN}\end{bmatrix}\begin{bmatrix}1 & 1/2\\-1 & 1/2\end{bmatrix}\begin{bmatrix}i_{dm}\\i_{cm}\end{bmatrix} \tag{81}$$

Applying the matrix multiplication for all effected terms of Equation *(81)* produces Equation *(82)*:

$$v_{Pg}\begin{bmatrix}0\\1\end{bmatrix}+\begin{bmatrix}v_{dm}\\v_{cm}\end{bmatrix}=Z_{LISN}\begin{bmatrix}2 & 0\\0 & 1/2\end{bmatrix}\begin{bmatrix}i_{dm}\\i_{cm}\end{bmatrix} \tag{82}$$

Equation *(82)* describes both the DM and CM relationships for the LISNs. The bottom row of this formulation describes the CM behavior specifically. Isolating v_{Pg} in Equation *(82)* highlights the final CM equation, which is shown as Equation (*83*):

$$v_{Pg}=-v_{cm}+\frac{Z_{LISN}}{2}i_{cm} \tag{83}$$

A.2. CM Decomposition of Filter Inductors

Resolving the CM equivalent relationship for the filter inductors is detailed in this section. Applying KVL to both branches within the MM model shown in Figure 11 produces Equation (*84*):

$$-v_{Pg}\begin{bmatrix}1\\1\end{bmatrix}-\begin{bmatrix}v_{1P}\\v_{2P}\end{bmatrix}+\begin{bmatrix}v_{Lf1}\\v_{Lf2}\end{bmatrix}+\begin{bmatrix}v'_{1P}\\v'_{2P}\end{bmatrix}+v'_{Pg}\begin{bmatrix}1\\1\end{bmatrix}=0 \tag{84}$$

Isolating the filter inductor voltages and primed terms gives Equation *(85)*:

$$\begin{bmatrix}v_{1P}\\v_{2P}\end{bmatrix}+v_{Pg}\begin{bmatrix}1\\1\end{bmatrix}=\begin{bmatrix}v_{Lf1}\\v_{Lf2}\end{bmatrix}+\begin{bmatrix}v'_{1P}\\v'_{2P}\end{bmatrix}+v'_{Pg}\begin{bmatrix}1\\1\end{bmatrix} \tag{85}$$

The next step is to left-multiply *(85)* by the T_v^2 matrix definition in order to decompose the MM voltage sources into their DM and CM representation. This produces Equation *(86)*:

$$T_v^2 \begin{bmatrix} v_{1P} \\ v_{2P} \end{bmatrix} + v_{Pg} T_v^2 \begin{bmatrix} 1 \\ 1 \end{bmatrix} = T_v^2 \begin{bmatrix} v_{Lf1} \\ v_{Lf2} \end{bmatrix} + T_v^2 \begin{bmatrix} v'_{1P} \\ v'_{2P} \end{bmatrix} + v'_{Pg} T_v^2 \begin{bmatrix} 1 \\ 1 \end{bmatrix} \tag{86}$$

Performing the matrix multiplication on each term produces Equation *(87)*:

$$\begin{bmatrix} v_{dm} \\ v_{cm} \end{bmatrix} + v_{Pg} \begin{bmatrix} 0 \\ 1 \end{bmatrix} = \begin{bmatrix} v_{Lf,dm} \\ v_{Lf,cm} \end{bmatrix} + \begin{bmatrix} v'_{dm} \\ v'_{cm} \end{bmatrix} + v'_{Pg} \begin{bmatrix} 0 \\ 1 \end{bmatrix} \tag{87}$$

Isolating the bottom row to highlight the CM behavior of the circuit produces Equation *(88)*:

$$v_{cm} + v_{Pg} = v_{Lf,cm} + v'_{cm} + v'_{Pg} \tag{88}$$

The only term in *(88)* that is not well defined with respect to the arbitrary reference points is $v_{Lf,cm}$. This term is resolved by analyzing the defining equation for the filter inductors, which is given in Equation *(5)*. This definition is repeated for ease of analysis as Equation *(89)*:

$$\begin{bmatrix} v_{Lf1} \\ v_{Lf2} \end{bmatrix} = L_f \begin{bmatrix} 1+a & m \\ m & 1-a \end{bmatrix} \frac{\mathrm{d}}{\mathrm{dt}} \begin{bmatrix} i_1 \\ i_2 \end{bmatrix} \tag{89}$$

Left multiplying both sides by T_v^2 produces Equation *(90)*:

$$T_v^2 \begin{bmatrix} v_{Lf1} \\ v_{Lf2} \end{bmatrix} = L_f T_v^2 \begin{bmatrix} 1+a & m \\ m & 1-a \end{bmatrix} \frac{\mathrm{d}}{\mathrm{dt}} \begin{bmatrix} i_1 \\ i_2 \end{bmatrix} \tag{90}$$

In order to describe the MM current vector $\begin{bmatrix} i_1 \\ i_2 \end{bmatrix}$ by the associated DM and CM relationships, $(T_i^2)^{-1} \begin{bmatrix} i_{dm} \\ i_{cm} \end{bmatrix}$ is substituted for this term in Equation *(90)*, which produces Equation *(91)*:

$$T_v^2 \begin{bmatrix} v_{Lf1} \\ v_{Lf2} \end{bmatrix} = L_f T_v^2 \begin{bmatrix} 1+a & m \\ m & 1-a \end{bmatrix} (T_i^2)^{-1} \frac{\mathrm{d}}{\mathrm{dt}} \begin{bmatrix} i_{dm} \\ i_{cm} \end{bmatrix} \tag{91}$$

Carrying out the matrix multiplication for the filter inductor voltages and explicitly representing the T_v^2 and $(T_i^2)^{-1}$ matrices produces Equation *(92)*:

$$\begin{bmatrix} v_{Lf,dm} \\ v_{Lf,cm} \end{bmatrix} = L_f \begin{bmatrix} 1 & -1 \\ 1/2 & 1/2 \end{bmatrix} \begin{bmatrix} 1+a & m \\ m & 1-a \end{bmatrix} \begin{bmatrix} 1 & 1/2 \\ -1 & 1/2 \end{bmatrix} \frac{\mathrm{d}}{\mathrm{dt}} \begin{bmatrix} i_{dm} \\ i_{cm} \end{bmatrix} \tag{92}$$

Performing matrix multiplication on Equation *(92)* produces Equation *(93)*:

$$\begin{bmatrix} v_{Lf,dm} \\ v_{Lf,cm} \end{bmatrix} = L_f \begin{bmatrix} 2(1-m) & a \\ a & \frac{1}{2}(1+m) \end{bmatrix} \frac{\mathrm{d}}{\mathrm{dt}} \begin{bmatrix} i_{dm} \\ i_{cm} \end{bmatrix} \tag{93}$$

The equation of interest for $v_{Lf,cm}$ is given by the bottom row of *(93)*. That relationship is highlighted in Equation *(94)*:

$$v_{Lf,cm} = L_f a \frac{\mathrm{d}}{\mathrm{dt}} i_{dm} + \frac{L_f}{2}(1+m)\frac{\mathrm{d}}{\mathrm{dt}} i_{cm} \tag{94}$$

The relationship between i_{cm} and $v_{Lf,cm}$ represents the constitutive relationship for an inductor; and this CM equivalent relationship is adequately defined. On the other hand, the influence of the DM current term i_{dm} in Equation *(94)* requires further definition. This term could be defined as a current source; however, voltage expressions are preferred because KVL is used to create the section-specific CEM at the end of this step. Fortunately, this term can be isolated and described in terms of voltage sources.

To derive an equivalent relationship for i_{dm} in terms of voltage sources, it is necessary to revisit the definition given for the inductors in Equation *(5)*. Using this expression, the current equations can be isolated by multiplying the voltage equations by the inverse of the inductance matrix. The normalized inductance matrix without the L_f scaling term is defined in Equation *(95)*:

$$(L) = \begin{bmatrix} 1+a & m \\ m & 1-a \end{bmatrix} \tag{95}$$

The inverse of the inductance matrix is provided in Equation *(96)*:

$$(L)^{-1} = \frac{1}{1-m^2-a^2} \begin{bmatrix} 1-a & -m \\ -m & 1+a \end{bmatrix} \tag{96}$$

The derivative operator also needs to be inverted, so here the Heaviside operator $p \triangleq \frac{d}{dt}$ is applied to manipulate the equations with greater ease algebraically. The remainder of this analysis takes advantage of the simplicity of the Heaviside operator for algebraic operations with respect to differentiation. Leveraging these simplifications, Equation *(5)* is restated in Equation *(97)*:

$$\begin{bmatrix} v_{Lf1} \\ v_{Lf2} \end{bmatrix} = pL_f(L) \begin{bmatrix} i_1 \\ i_2 \end{bmatrix} \tag{97}$$

The filter inductor currents are isolated by multiplying the inverse inductance matrix from Equation *(96)* and dividing by the Heaviside operator p on both sides of Equation *(97)* to produce Equation *(98)*:

$$\begin{bmatrix} i_i \\ i_2 \end{bmatrix} = \frac{1}{pL_f}(L)^{-1} \begin{bmatrix} v_{Lf1} \\ v_{Lf2} \end{bmatrix} \tag{98}$$

The next step is to left multiply both sides of Equation *(98)* by T_i^2 to represent the MM currents in their DM and CM representations. It is also beneficial to substitute $(T_v^2)^{-1} \begin{bmatrix} v_{Lf,dm} \\ v_{Lf,cm} \end{bmatrix}$ for the MM inductor voltage vector to replace the MM voltages with the equivalent DM and CM representations. The result of these manipulations is given by Equation *(99)*:

$$T_i^2 \begin{bmatrix} i_1 \\ i_2 \end{bmatrix} = \frac{1}{pL_f} T_i^2 (L)^{-1} (T_v^2)^{-1} \begin{bmatrix} v_{Lf,dm} \\ v_{Lf,cm} \end{bmatrix} \tag{99}$$

Performing matrix multiplication for the expression $T_i^2 \begin{bmatrix} i_1 \\ i_2 \end{bmatrix}$ and expanding matrices T_i^2, $(L)^{-1}$, and $(T_v^2)^{-1}$ produces Equation *(100)*:

$$\begin{bmatrix} i_{dm} \\ i_{cm} \end{bmatrix} = \frac{1}{pL_f} \begin{bmatrix} {}^{1}\!/_{2} & -{}^{1}\!/_{2} \\ 1 & 1 \end{bmatrix} \frac{1}{1 - m^2 - a^2} \begin{bmatrix} 1 - a & -m \\ -m & 1 + a \end{bmatrix} \begin{bmatrix} {}^{1}\!/_{2} & 1 \\ -{}^{1}\!/_{2} & 1 \end{bmatrix} \begin{bmatrix} v_{Lf,dm} \\ v_{Lf,cm} \end{bmatrix} \tag{100}$$

Performing matrix multiplication on Equation *(100)* produces Equation *(101)*:

$$\begin{bmatrix} i_{dm} \\ i_{cm} \end{bmatrix} = \frac{1}{pL_f} \frac{1}{1 - m^2 - a^2} \begin{bmatrix} \frac{1 + m}{2} & -a \\ -a & 2(1 - m) \end{bmatrix} \begin{bmatrix} v_{Lf,dm} \\ v_{Lf,cm} \end{bmatrix} \tag{101}$$

The DM current i_{dm} is described by the upper row of Equation *(101)*; this relationship is highlighted in Equation *(102)*.

$$i_{dm} = \frac{1}{pL_f} \left[\frac{1 + m}{2(1 - m^2 - a^2)} v_{Lf,dm} - \frac{a}{1 - m^2 - a^2} v_{Lf,cm} \right] \tag{102}$$

From this explicit definition for i_{dm}, it is possible to fully describe Equation *(94)* in terms of only voltage definitions. Restating Equation *(94)* with the derivatives expressed using the Heaviside operator produces Equation *(103)*:

$$v_{Lf,cm} = apL_f i_{dm} + \frac{L_f}{2}(1+m)pi_{cm} \tag{103}$$

Substituting the result for i_{dm} from Equation *(102)* into Equation *(103)* produces Equation *(104)*:

$$\begin{aligned} v_{Lf,cm} = apL_f \left\{ \frac{1}{pL_f} \left[\frac{1+m}{2(1-m^2-a^2)} v_{Lf,dm} - \frac{a}{1-m^2-a^2} v_{Lf,cm} \right] \right\} \\ + \frac{L_f}{2}(1+m)pi_{cm} \end{aligned} \tag{104}$$

Simplifying this expression by cancelling like terms produces Equation *(105)*:

$$v_{Lf,cm} = \frac{a(1+m)}{2(1-m^2-a^2)} v_{Lf,dm} - \frac{a^2}{1-m^2-a^2} v_{Lf,cm} + \frac{L_f}{2}(1+m)pi_{cm} \tag{105}$$

Rearranging Equation *(105)* to isolate all terms associated with $v_{Lf,cm}$ produces Equation *(106)*:

$$\left(1 + \frac{a^2}{1-m^2-a^2}\right) v_{Lf,cm} = \frac{a(1+m)}{2(1-m^2-a^2)} v_{Lf,dm} + \frac{L_f}{2}(1+m)pi_{cm} \tag{106}$$

Simplifying the coefficient in front of $v_{Lf,cm}$ produces Equation *(107)*:

$$\left(\frac{1-m^2}{1-m^2-a^2}\right) v_{Lf,cm} = \frac{a(1+m)}{2(1-m^2-a^2)} v_{Lf,dm} + \frac{L_f}{2}(1+m)pi_{cm} \tag{107}$$

Factoring the numerator of the coefficient in front of $v_{Lf,cm}$ produces Equation *(108)*:

$$\left(\frac{(1-m)(1+m)}{1-m^2-a^2}\right) v_{Lf,cm} = \frac{a(1+m)}{2(1-m^2-a^2)} v_{Lf,dm} + \frac{L_f}{2}(1+m)pi_{cm} \tag{108}$$

Dividing both sides of *(108)* by the coefficient in front of $v_{Lf,cm}$ produces Equation *(109)*:

$$v_{Lf,cm} = \frac{1-m^2-a^2}{(1-m)(1+m)} \frac{a(1+m)}{2(1-m^2-a^2)} v_{Lf,dm} + \frac{1-m^2-a^2}{(1-m)(1+m)} \frac{(1+m)L_f}{2} p i_{cm} \tag{109}$$

Simplifying the coefficients of Equation *(109)* produces Equation *(110)*:

$$v_{Lf,cm} = \frac{a}{2(1-m)} v_{Lf,dm} + \frac{L_f}{2} \frac{(1-a^2-m^2)}{1-m} p i_{cm} \tag{110}$$

Equation *(110)* is close to the final representation needed to describe the filter inductors, but the meaning of the term $v_{Lf,dm}$ is not obvious based on the analysis up to this point. Therefore, it is necessary to revisit the MM model shown in Figure 7 to better understand how the DM voltage across the filter inductors, $v_{Lf,dm}$, can be equivalently represented.

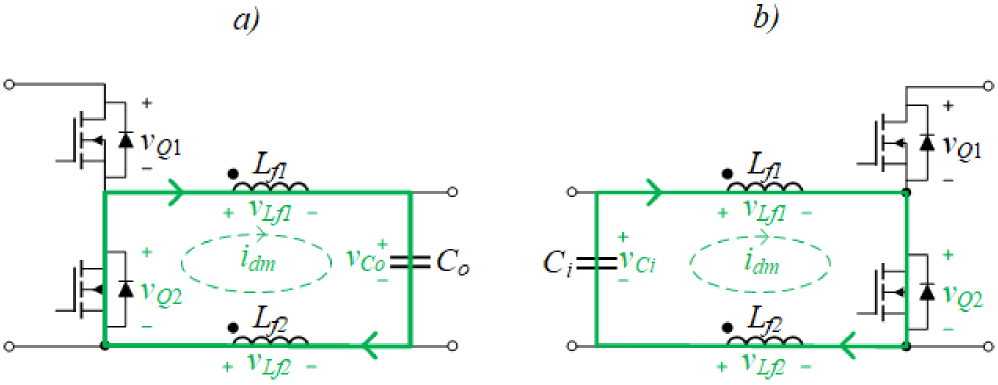

Figure 58. KVL loop to resolve $v_{Lf,dm}$ for (a) buck and (b) boost converter

The DM term $v_{Lf,dm}$ is defined by the decomposition technique to be $v_{Lf,dm} = v_{Lf1} - v_{Lf2}$. Figure 58(a) and Figure 58(b) highlight the sections of the MM model concerned with this behavior for the buck and boost converters, respectively. The KVL loop for each topology can be used to highlight the MM voltages necessary to describe $v_{Lf,dm}$. The topological difference between the buck and boost converters necessitates a separate treatment for this portion of the analysis. Applying KVL to the selected portion of the buck converter, starting at $v_{Lf,1}$, produces Equation *(111)*:

$$v_{Lf1} + v_{Co} - v_{Lf2} - v_{Q2} = 0 \tag{111}$$

Isolating the DM voltage difference for $v_{Lf,dm}$ produces Equation *(112)*:

$$v_{Lf,dm,buck} = v_{Lf1} - v_{Lf2} = v_{Q2} - v_{Co} \tag{112}$$

Therefore, the DM inductor voltage for the buck converter is $v_{Q2} - v_{Co}$. Similarly, applying KVL to the selected portion of the boost converter, starting at $v_{Lf,1}$, produces Equation *(113)*:

$$v_{Lf1} + v_{Q2} - v_{Lf2} - v_{Ci} = 0 \tag{113}$$

Isolating the DM voltage difference for $v_{Lf,dm}$ produces Equation *(114)*:

$$v_{Lf,dm,boost} = v_{Lf1} - v_{Lf2} = v_{Ci} - v_{Q2} \tag{114}$$

Therefore, the DM inductor voltage for the boost converter is $v_{Ci} - v_{Q2}$.

To assemble the final CM equivalent relationship for the filter inductors, the original voltage equation describing the system in Equation *(88)* is updated with Equation *(110)*. Substituting the relationship in and isolating for v_{Pg} produces Equation (*115*):

$$v_{Pg} = -v_{cm} + \frac{L_f}{2}\frac{(1 - a^2 - m^2)}{1 - m} pi_{cm} + \frac{a}{2(1 - m)} v_{Lf,dm} + v'_{cm} + v'_{Pg} \tag{115}$$

A.3. CM Decomposition of Capacitive Couplings of the Load

Resolving the CM equivalent relationship for the capacitive coupling of the load is detailed in this section. Applying KVL to both branches within the MM model shown in Figure 13 produces Equation (*116*):

$$-v'_{Pg}\begin{bmatrix}1\\1\end{bmatrix} - \begin{bmatrix}v'_{1P}\\v'_{2P}\end{bmatrix} + \begin{bmatrix}v_{Cog,1}\\v_{Cog,2}\end{bmatrix} = 0 \tag{116}$$

Isolating the MM output capacitance voltages produces Equation *(117)*:

$$\begin{bmatrix} v'_{1P} \\ v'_{2P} \end{bmatrix} + v'_{Pg} \begin{bmatrix} 1 \\ 1 \end{bmatrix} = \begin{bmatrix} v_{Cog,1} \\ v_{Cog,2} \end{bmatrix} \tag{117}$$

Left multiplying both sides of Equation *(117)* by T_v^2 decomposes the MM elements into their DM and CM representations. This produces Equation *(118)*:

$$T_v^2 \begin{bmatrix} v'_{1P} \\ v'_{2P} \end{bmatrix} + v'_{Pg} T_v^2 \begin{bmatrix} 1 \\ 1 \end{bmatrix} = T_v^2 \begin{bmatrix} v_{Cog,1} \\ v_{Cog,2} \end{bmatrix} \tag{118}$$

The MM voltages for the output capacitance elements are governed by the associated constitutive relations, which are expressed with the aid of the Heaviside operator in Equation *(119)*:

$$\begin{bmatrix} v_{Cog,1} \\ v_{Cog,2} \end{bmatrix} = \frac{1}{pC_{og}} \begin{bmatrix} 1 & 0 \\ 0 & 1 \end{bmatrix} \begin{bmatrix} i_1 \\ i_2 \end{bmatrix} \tag{119}$$

Substituting *(119)* into *(118)* produces Equation *(120)*:

$$T_v^2 \begin{bmatrix} v'_{1P} \\ v'_{2P} \end{bmatrix} + v'_{Pg} T_v^2 \begin{bmatrix} 1 \\ 1 \end{bmatrix} = T_v^2 \frac{1}{pC_{og}} \begin{bmatrix} 1 & 0 \\ 0 & 1 \end{bmatrix} \begin{bmatrix} i_1 \\ i_2 \end{bmatrix} \tag{120}$$

Substituting $(T_i^2)^{-1} \begin{bmatrix} i'_{dm} \\ i'_{cm} \end{bmatrix}$ for the MM current vector produces Equation *(121)*:

$$T_v^2 \begin{bmatrix} v'_{1P} \\ v'_{2P} \end{bmatrix} + v'_{Pg} T_v^2 \begin{bmatrix} 1 \\ 1 \end{bmatrix} = T_v^2 \frac{1}{pC_{og}} \begin{bmatrix} 1 & 0 \\ 0 & 1 \end{bmatrix} (T_i^2)^{-1} \begin{bmatrix} i'_{dm} \\ i'_{cm} \end{bmatrix} \tag{121}$$

Carrying out matrix multiplication on the left-hand side and explicitly representing T_v^2 and $(T_i^2)^{-1}$ on the right-hand side of Equation *(121)* produces Equation *(122)*:

$$\begin{bmatrix} v'_{dm} \\ v'_{cm} \end{bmatrix} + v'_{Pg} \begin{bmatrix} 0 \\ 1 \end{bmatrix} = \frac{1}{pC_{og}} \begin{bmatrix} 1 & -1 \\ 1/2 & 1/2 \end{bmatrix} \begin{bmatrix} 1 & 0 \\ 0 & 1 \end{bmatrix} \begin{bmatrix} 1 & 1/2 \\ -1 & 1/2 \end{bmatrix} \begin{bmatrix} i'_{dm} \\ i'_{cm} \end{bmatrix} \tag{122}$$

Performing matrix multiplication produces Equation *(123)*:

$$\begin{bmatrix} v'_{dm} \\ v'_{cm} \end{bmatrix} + v'_{Pg} \begin{bmatrix} 0 \\ 1 \end{bmatrix} = \frac{1}{pC_{og}} \begin{bmatrix} 2 & 0 \\ 0 & 1/2 \end{bmatrix} \begin{bmatrix} i'_{dm} \\ i'_{cm} \end{bmatrix} \tag{123}$$

The CM voltage equation for the KVL loop that describes the CM equivalent relationship is given by the bottom row of Equation *(123)*. Therefore, the CM KVL loop used to describe CM equivalent relationship for the capacitive coupling is given in Equation (*124*):

$$v'_{Pg} = -v'_{cm} + \frac{1}{p2C_{og}} i'_{cm} \tag{124}$$

A.4. Construction of Final CEM for Simplified Buck Converter

Resolving the final CEM for the simplified buck converter is detailed in this section. The first reference point that is defined explicitly is P'. This reference is defined first because it provides significant insight with little analysis. As specified in Figure 15, P' exists as the physical connection between the filter inductors and capacitive coupling for the load. The insight for this section of the CEM is that irrespective of the choice of reference node from the MM model, the voltage sources v_{cm3} and v_{cm4} will cancel out. This conclusion arises through analysis of the definitions for these two sources. The term v_{cm3} is defined for the filter inductor section and its definition is given by Equation *(125)*:

$$v_{cm3} = \frac{1}{2}(v'_{1P} + v'_{2P}) \tag{125}$$

Similarly, v_{cm4} is defined for the output capacitance section and its definition is given by Equation *(126)*:

$$v_{cm4} = \frac{1}{2}(v'_{1P} + v'_{2P}) \tag{126}$$

Equation *(125)* and Equation *(126)* confirm that these two sources will have the same magnitude regardless of choice of reference point. In addition, Figure 15 shows that these two sources are oriented in opposition. Thus, these two voltage sources cancel each other and are eliminated from the CEM. Since the only elements remaining in the CEM in Figure 15 are passive components, the choice of MM node for P' is not important for the buck converter. The updated CEM that incorporates the cancellation for v_{cm4} and v_{cm4} is shown in Figure 59.

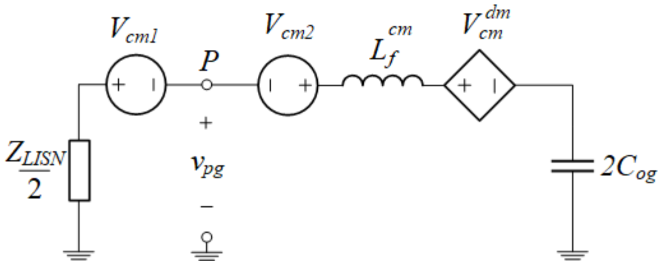

Figure 59. Updated CEM for the buck converter

The final step in constructing the CEM is to define P relative to a node in the MM model. This section of the MM model is concerned with the switching devices, so the CM voltage sources are expected to remain in the CEM and be defined by MM voltages. The two CM voltage sources defined at P are v_{cm1} and v_{cm2}. These terms are specified with respect to their individual sections by Table 4. It is beneficial to start with an intuitive decision for defining P. After resolving the intuitive CEM, redefining the system in a way that simplifies the system concludes the analysis for generating the final CEM. One intuitive MM node that could be used to define P for the buck converter is the lower rail node L. This specification defines v_{cm1}, which is the CM voltage source for the LISN section of the model, as Equation *(127)*:

$$v_{cm1} = \frac{1}{2}(v_{1L} + v_{2L}) \tag{127}$$

Since v_{cm1} is defined at the LISNs, the MM voltages are defined from the upper rail U for v_1 and lower rail L for v_2 as seen in the MM model of Figure 15. Substituting this relationship into Equation *(127)* produces Equation *(128)*:

$$v_{cm1} = \frac{1}{2}(v_{UL} + v_{LL}) \tag{128}$$

The voltage source v_{LL} is zero by the definition of a voltage difference at a single point. The source term v_{UL} is equal to v_{Ci}, which can be seen in Figure 15. Therefore, for P defined as L, v_{cm1} is described by Equation *(129)*:

$$v_{cm1} = \frac{1}{2}(v_{Ci}) \tag{129}$$

The last term to be resolved is v_{cm2}. This voltage source is described by the filter inductor CM equivalent relationship. The definition of the voltage source with P defined by the lower rail of the MM model is given by Equation *(130)*:

$$v_{cm2} = \frac{1}{2}(v_{1L} + v_{2L}) \tag{130}$$

The MM voltages are defined by A and N nodes in Figure 15. Specifically, v_1 is referenced to the A node, and v_2 is referenced to the N node. Substituting these relationships into Equation *(130)* produces Equation *(131)*:

$$v_{cm2} = \frac{1}{2}(v_{AL} + v_{NL}) \tag{131}$$

For this MM model, the node N and the node L are equipotential. Therefore, v_{NL} is zero. The term v_{AL} is described by the lower switch voltage v_{Q2}. Therefore, v_{cm2} is given by Equation *(132)*:

$$v_{cm2} = \frac{1}{2}(v_{Q2}) \tag{132}$$

Equation *(129)* and Equation *(132)* can be combined to produce a complete description of the CEM in Figure 15 for the buck converter. However, as stated previously, some reference points are more advantageous than others in terms of analysis. Therefore, to align the analysis in a more helpful way for the later sections of this thesis, the fundamental model is redefined relative to a new reference point. The process of changing the reference point for a CEM is described in [47]. The goal is generally to simplify the system by means of eliminating CM voltage sources by shifting the MM voltage into a single CM voltage source. The new reference point selected for the buck converter, labelled as P_{new}, is defined as the midpoint between the upper and lower rails, denoted U, L. The change from P to P_{new} can be thought of as shifting the voltage seen at each CM voltage source by a consistent amount, given by Δv_{Pg}.

It is noted that this voltage shift does not change the behavior of the CEM, but it does allow beneficial simplification of CM voltage sources. In order to change the reference point P, defined with respect to the lower rail L, to the new reference point P_{new}, defined with respect to the midpoint of nodes U, L, the reference voltage v_{Pg} needs to be updated. This update defines a new quantity $v_{Pnewg} = v_{Pg} + \Delta v_{Pg}$; where Δv_{Pg} defines the voltage added to CEM to change the reference from P to P_{new}. Shifting the reference voltage from a potential difference between L to the testbed ground to a potential difference defined at the midpoint of nodes U, L to the testbed ground is performed by adding Δv_{Pg} to the original reference potential. The voltage Δv_{Pg} is thus effectively equal to the voltage at the midpoint of nodes U, L, which is equal to $\frac{1}{2} v_{Ci}$ in the MM model. Updating the original equation for the CM equivalent representation of the LISNs by adding Δv_{Pg} on both sides of the KVL loop that constitutes the CM relationship given in Equation *(9)* provides the relationship given for the new reference point. As specified in Table 4, v_{cm} from Equation *(9)* is relabeled as v_{cm1}. Thus, the updated CM KVL loop for the LISN section produces Equation *(133)*:

$$v_{Pg} + \Delta v_{Pg} = \Delta v_{Pg} - v_{cm1} + \frac{Z_{LISN}}{2} i_{cm} \tag{133}$$

Simplifying and substituting the definition of v_{Pnewg} into Equation *(133)* produces Equation *(134)*:

$$v_{Pnewg} = -\left(v_{cm1} - \Delta v_{Pg}\right) + \frac{Z_{LISN}}{2} i_{cm} \tag{134}$$

Therefore, to shift from P to P_{new}, Δv_{Pg} needs only to be subtracted from the original CM voltage source, which is labeled v_{cm1} in this generalized analysis. Subtracting Δv_{Pg} from Equation *(129)* produces Equation *(135)*:

$$v_{cm1} = \frac{1}{2} v_{Ci} - \frac{1}{2} v_{Ci} \tag{135}$$

Thus, v_{cm1} is equal to zero when the reference point is shifted to the midpoint voltage of nodes U, L. The updated CEM from Figure 15 with reference point shifted for the LISN section is shown in Figure 60.

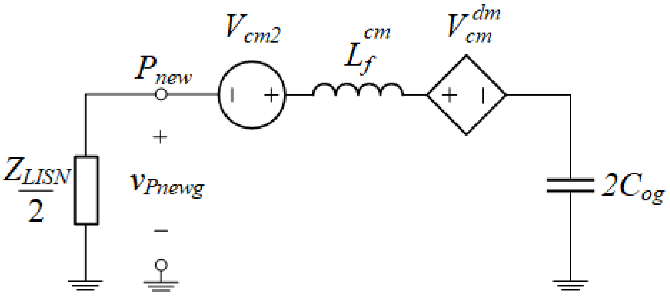

Figure 60. Updated CEM with new reference point for the buck converter

The same process is applied to v_{cm2}. The equation that defines the KVL loop of the CM equivalent relationship for the filter inductors is given by Equation *(11)*. As specified in Table 4, v_{cm} in Equation *(11)* is relabeled as v_{cm2}. Adding Δv_{Pg} on both sides of the generalized form of Equation *(11)* produces Equation *(136)*:

$$\begin{aligned} v_{Pg} + \Delta v_{Pg} = \Delta v_{Pg} - v_{cm2} + \frac{a}{2(1-m)} v_{Lf,dm,buck} + \frac{L_f}{2} \frac{(1 - a^2 - m^2)}{1-m} p i_{cm} \\ + v_{cm}' + v_{Pg}' \end{aligned} \tag{136}$$

Simplifying and substituting the definition of v_{Pnewg} into Equation *(136)* produces Equation *(137)*:

$$v_{Pnewg} = -\left(v_{cm2} - \Delta v_{Pg}\right) + \frac{a}{2(1-m)} v_{Lf,dm,buck} + \frac{L_f}{2}\frac{(1-a^2-m^2)}{1-m} p i_{cm} \\ + v'_{cm} + v'_{Pg} \tag{137}$$

Therefore, v_{cm2} can be shifted to the new reference point P_{new} by simply subtracting Δv_{Pg} from the original source definition. Subtracting Δv_{Pg} from Equation *(132)* produces Equation *(138)*:

$$v_{cm2} = \frac{1}{2} v_{Q2} - \frac{1}{2} v_{Ci} \tag{138}$$

Simplifying the expression produces Equation *(139)*:

$$v_{cm2} = \frac{1}{2}\left(v_{Q2} - v_{Ci}\right) \tag{139}$$

After this manipulation, the total CM voltage for the buck converter is defined only by v_{cm2}. It can be seen from this analysis that changing the reference point from P to P_{new} essentially shifts the MM voltages between the affected CM voltage sources. It is also noted that redefining the CEM at the midpoint of the upper and lower rails is included to facilitate the more complex CEM analysis in the following section of this thesis. This redefinition also permits the removal of v_{cm1}, resulting in the simplified version of the final CEM for the buck converter, which is shown in Figure 16. The circuit is a series combination of passive elements and a single CM voltage source. The CM voltage source $v_{nom,1}^{cm}$ is the series combination of v_{dm}^{cm} and v_{cm2}. The term v_{dm}^{cm} is given by Equation (15); and v_{cm2} is given by Equation *(139)*. Noting the polarity of each CM voltage source shown in Figure 15, $v_{nom,1}^{cm}$ is described in terms of v_{dm}^{cm} and v_{cm2} in Equation *(140)*:

$$v_{nom,1}^{cm} = v_{cm2} - v_{dm}^{cm} \tag{140}$$

Substituting the definitions for v_{dm}^{cm} and v_{cm2} produces Equation *(141)*:

$$v_{nom,1}^{cm} = \frac{1}{2}\left(v_{Q2} - v_{Ci}\right) - \frac{a}{2(1-m)}\left(v_{Q2} - v_{Co}\right) \tag{141}$$

Extracting the $\frac{1}{2}$ coefficient and combining similar terms produces Equation *(142)*.

$$v_{nom,1}^{cm} = \frac{1}{2}\left[v_{Q2} - \frac{a}{1-m}\left(v_{Q2} - v_{Co}\right) - v_{Ci}\right] \tag{142}$$

The final CM KVL loop that describes Figure 16 is shown in Equation *(143)*:

$$v_{nom,1}^{cm} = \frac{Z_{LISN}}{2} i_{cm} + \frac{L_f}{2} \frac{(1 - a^2 - m^2)}{1-m} p i_{cm} + \frac{1}{p 2 C_{og}} i_{cm} \tag{143}$$

A.5. Construction of Final CEM for Simplified Boost Converter

Resolving the final CEM for the simplified boost converter is detailed in this section. The first step in the analysis is to analyze the reference point at P. The analysis for this reference point is handled first because of its simplicity. The affected CM voltages for this section are v_{cm1} and v_{cm2}. Similar to the analysis shown in Section 3.2.4.1, these voltage sources have the same definitions but with opposite signs. Therefore, these sources eliminate each other from the CEM regardless of definition for the reference point. Thus, both v_{cm1} and v_{cm2} do not contribute to the CEM for the boost converter. The updated CEM that incorporates the elimination of v_{cm1} and v_{cm2} is shown in Figure 61.

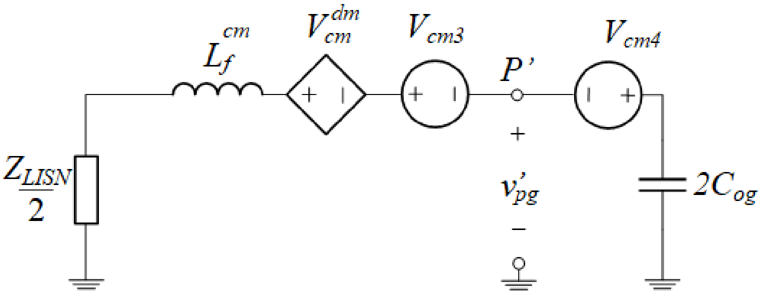

Figure 61. Updated CEM for the boost converter

The final step in the analysis is to explicitly define P'. As seen in Figure 17, the CM voltages associated with P' are v_{cm3} and v_{cm4}. Similar to the analysis in Section 3.2.4.1, P' can be assigned to the lower node in the MM model, labelled L. As noted in Table 5, v_{cm3} is defined as v_{cm}' for the filter inductor section and its definition is given by Equation *(144)*:

$$v_{cm3} = \frac{1}{2}(v'_{1P} + v'_{2P}) \tag{144}$$

Referencing v_{cm3} to the specific MM node L, and defining v_1 as the A node and v_2 as the N node produces Equation *(145)*:

$$v_{cm3} = \frac{1}{2}(v_{AL} + v_{NL}) \tag{145}$$

The voltage term v_{NL} is zero because the MM nodes N and L are equipotential for the boost converter. The term v_{AL} is equal to the lower switch voltage v_{Q2} as seen in the MM model in Figure 17. Thus, the final simplification for v_{cm3} is given in Equation *(146)*:

$$v_{cm3} = \frac{1}{2}(v_{Q2}) \tag{146}$$

The remaining term that needs to be resolved is v_{cm4}. As noted in Table 5, the CM voltage source for the load section of the model is defined as v_{cm}, and its equation is restated in Equation *(147)*:

$$v_{cm4} = \frac{1}{2}(v'_{1P} + v'_{2P}) \tag{147}$$

Referencing v_{cm4} to the specific MM node L, and defining v_1 as the U node and v_2 as the L node produces Equation *(148)*:

$$v_{cm4} = \frac{1}{2}(v_{UL} + v_{LL}) \tag{148}$$

The voltage term v_{LL} is zero. The term v_{UL} is equal to the output capacitance voltage v_{Co} for the boost converter. Therefore, the final equation for v_{cm4} defined at node L is given by Equation *(149)*:

$$v_{cm4} = \frac{1}{2}(v_{Co}) \tag{149}$$

The voltage definitions given in Equations *(146)* and *(149)* are sufficient to complete the CEM for the boost converter. However, as shown for the case of the buck converter in Section

3.2.4.1, it is also beneficial to redefine the reference point for the boost converter. The same reference point shift from node L to the midpoint of the upper and lower rails, denoted U, L, is applied for the boost converter. The new reference point for the boost converter is labelled as P_{new}. The additional term needed to shift the voltage sources is defined as Δv_{Pg}, and the new reference voltage is given by $v_{Pnewg} = v'_{Pg} + \Delta v_{Pg}$. The term Δv_{Pg} is defined as the voltage at the midpoint of nodes U, L with respect to node L.. Thus, Δv_{Pg} is equal to $\frac{1}{2} v_{Co}$ for the boost converter. This midpoint value is similar to that used in the case of the buck converter, except that this voltage is a function of the output capacitor voltage due to the location of the switching devices. It is noted that shifting the reference point does not change the behavior of the CEM but provides a simplification for the system by eliminating certain CM voltage sources.

Section 3.2.4.1 demonstrated the process of changing reference points by subtracting an offset from the CM voltage source in the KVL expression for each individual CEM section. The same process is followed here. Subtracting Δv_{Pg} from v_{cm3} produces Equation *(150)*:

$$v_{cm3} = \frac{1}{2} v_{Q2} - \frac{1}{2} v_{Co} \tag{150}$$

Factoring $\frac{1}{2}$ out of each term produces Equation *(23)*:

$$v_{cm3} = \frac{1}{2} \left(v_{Q2} - v_{Co} \right) \tag{151}$$

The final CM voltage that needs to be resolved is v_{cm4}. Subtracting Δv_{Pg} from Equation *(149)* produces Equation *(152)*:

$$v_{cm4} = \frac{1}{2} v_{Co} - \frac{1}{2} v_{Co} = 0 \tag{152}$$

Equation *(152)* demonstrates that the CEM defined at the midpoint of nodes U, L contains only v_{cm3}. The updated CEM from Figure 17 with reference point shifted for the LISN section is shown in Figure 62.

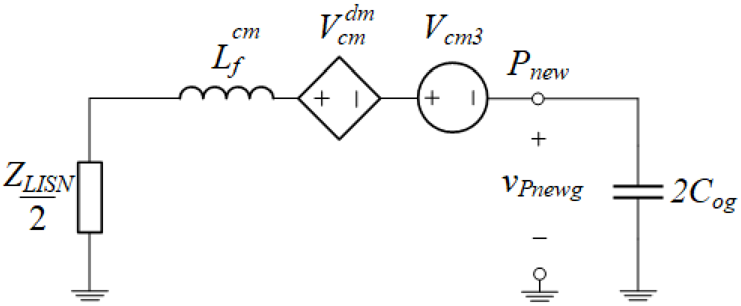

Figure 62. Updated CEM with new reference point for the boost converter

The previous analysis facilitates the construction of a final CEM for the boost converter. The final CEM is shown in Figure 18. The analysis performed with respect to defining the reference point P' at the midpoint of nodes U, L eliminated all CM voltage sources except v_{cm}^{dm} and v_{cm3}. The final voltage source, $v_{nom,2}^{cm}$ is the series combination of v_{cm}^{dm} and v_{cm3}. The term v_{cm}^{dm} is given by Equation (16). The term v_{cm3} is defined by Equation *(23)*. Noting the polarity of each CM voltage source shown in Figure 17, $v_{nom,2}^{cm}$ is described in terms of v_{dm}^{cm} and v_{cm3} in Equation *(153)*:

$$v_{nom,2}^{cm} = v_{dm}^{cm} + v_{cm3} \tag{153}$$

Substituting the definitions for v_{dm}^{cm} and v_{cm3} produces Equation *(24)*:

$$v_{nom,2}^{cm} = \frac{a}{2(1-m)}\left(v_{Ci} - v_{Q2}\right) + \frac{1}{2}\left(v_{Q2} - v_{Co}\right) \tag{154}$$

Extracting a negative sign from the v_{dm}^{cm} term as well as the $\frac{1}{2}$ coefficient, and combining similar terms produces Equation *(25)*:

$$v_{nom,2}^{cm} = \frac{1}{2}\left[v_{Q2} - \frac{a}{1-m}\left(v_{Q2} - v_{Ci}\right) - v_{Co}\right] \tag{155}$$

The final CM KVL loop that describes Figure 16 is shown in Equation *(26)*:

$$-v_{nom,2}^{cm} = \frac{Z_{LISN}}{2} i_{cm} + \frac{L_f}{2} \frac{(1 - a^2 - m^2)}{1 - m} p i_{cm} + \frac{1}{p2C_{og}} i_{cm} \tag{156}$$

A.6. CM Decomposition of BPC Parasitic Branch

Resolving the CM equivalent relationship for the capacitive coupling of the load is detailed in this section. Applying KVL to Figure 22 produces Equation *(37)*:

$$-v_{Pg}\begin{bmatrix}1\\1\\1\end{bmatrix} - \begin{bmatrix}v_{UP}\\v_{LP}\\v_{AP}\end{bmatrix} + \begin{bmatrix}v_{CU}\\v_{CL}\\v_{CA}\end{bmatrix} + Z_h\begin{bmatrix}1 & 1 & 1\\1 & 1 & 1\\1 & 1 & 1\end{bmatrix}\begin{bmatrix}i_U\\i_L\\i_A\end{bmatrix} = 0 \tag{157}$$

Rearranging the voltage sources produces Equation *(158)*:

$$\begin{bmatrix}v_{UP}\\v_{LP}\\v_{AP}\end{bmatrix} + v_{Pg}\begin{bmatrix}1\\1\\1\end{bmatrix} = \begin{bmatrix}v_{CU}\\v_{CL}\\v_{CA}\end{bmatrix} + Z_h\begin{bmatrix}1 & 1 & 1\\1 & 1 & 1\\1 & 1 & 1\end{bmatrix}\begin{bmatrix}i_U\\i_L\\i_A\end{bmatrix} \tag{158}$$

Left multiplying both sides by T_v^3 to separate the voltage sources into their DM and CM components produces Equation *(159)*:

$$T_v^3\begin{bmatrix}v_{UP}\\v_{LP}\\v_{AP}\end{bmatrix} + v_{Pg}T_v^3\begin{bmatrix}1\\1\\1\end{bmatrix} = T_v^3\begin{bmatrix}v_{CU}\\v_{CL}\\v_{CA}\end{bmatrix} + Z_hT_v^3\begin{bmatrix}1 & 1 & 1\\1 & 1 & 1\\1 & 1 & 1\end{bmatrix}\begin{bmatrix}i_U\\i_L\\i_A\end{bmatrix} \tag{159}$$

Substituting $(T_i^3)^{-1}\begin{bmatrix}i_{UL,dm}\\i_{UL,cm}\\i_{A,cm}\end{bmatrix}$ to separate the elements of $\begin{bmatrix}i_U\\i_L\\i_A\end{bmatrix}$ into their DM and CM components produces Equation *(160)*:

$$T_v^3\begin{bmatrix}v_{UP}\\v_{LP}\\v_{AP}\end{bmatrix} + v_{Pg}T_v^3\begin{bmatrix}1\\1\\1\end{bmatrix} = T_v^3\begin{bmatrix}v_{CU}\\v_{CL}\\v_{CA}\end{bmatrix} + Z_hT_v^3\begin{bmatrix}1 & 1 & 1\\1 & 1 & 1\\1 & 1 & 1\end{bmatrix}(T_i^3)^{-1}\begin{bmatrix}i_{UL,dm}\\i_{UL,cm}\\i_{A,cm}\end{bmatrix} \tag{160}$$

Carrying out the matrix multiplication for the voltage sources and currents produces Equation *(161)*:

$$\begin{bmatrix} v_{UL,dm} \\ v_{UL,cm} \\ v_{A,cm} \end{bmatrix} + v_{Pg} \begin{bmatrix} 0 \\ 1 \\ 1 \end{bmatrix} = \begin{bmatrix} v_{CUL,dm} \\ v_{CUL,cm} \\ v_{CA,cm} \end{bmatrix} + Z_h \begin{bmatrix} 0 & 0 & 0 \\ 0 & 1 & 1 \\ 0 & 1 & 1 \end{bmatrix} \begin{bmatrix} i_{UL,dm} \\ i_{UL,cm} \\ i_{A,cm} \end{bmatrix} \tag{161}$$

The CM equations from Equation *(161)* are highlighted in Equations *(162)* and *(163)*, with Equation *(162)* describing the behavior of the A branch and Equation *(163)* describing the U/L branch.

$$v_{A,cm} + v_{Pg} = v_{CA,cm} + Z_h\left(i_{UL,cm} + i_{A,cm}\right) \tag{162}$$

$$v_{UL,cm} + v_{Pg} = v_{CUL,cm} + Z_h\left(i_{UL,cm} + i_{A,cm}\right) \tag{163}$$

The terms $v_{CA,cm}$ and $v_{CUL,cm}$ can be resolved by substituting the constitutive relationships for the parasitic baseplate capacitances. This relationship is defined, taking advantage of the Heaviside operator p, in Equation *(164)*:

$$\begin{bmatrix} i_U \\ i_L \\ i_A \end{bmatrix} = p \begin{bmatrix} C_{Ug} & 0 & 0 \\ 0 & C_{Lg} & 0 \\ 0 & 0 & C_{Ag} \end{bmatrix} \begin{bmatrix} v_{CU} \\ v_{CL} \\ v_{CA} \end{bmatrix} \tag{164}$$

Left multiplying both sides of Equation *(164)* by T_i^3 produces Equation *(165)*:

$$T_i^3 \begin{bmatrix} i_U \\ i_L \\ i_A \end{bmatrix} = pT_i^3 \begin{bmatrix} C_{Ug} & 0 & 0 \\ 0 & C_{Lg} & 0 \\ 0 & 0 & C_{Ag} \end{bmatrix} \begin{bmatrix} v_{CU} \\ v_{CL} \\ v_{CA} \end{bmatrix} \tag{165}$$

Substituting in $(T_v^3)^{-1} \begin{bmatrix} v_{CUL,dm} \\ v_{CUL,cm} \\ v_{CA,cm} \end{bmatrix}$ for the voltage source vector produces Equation *(166)*:

$$T_i^3 \begin{bmatrix} i_U \\ i_L \\ i_A \end{bmatrix} = pT_i^3 \begin{bmatrix} C_{Ug} & 0 & 0 \\ 0 & C_{Lg} & 0 \\ 0 & 0 & C_{Ag} \end{bmatrix} (T_v^3)^{-1} \begin{bmatrix} v_{CUL,dm} \\ v_{CUL,cm} \\ v_{CA,cm} \end{bmatrix} \tag{166}$$

Carrying out the matrix multiplication for the current vector on the left-hand side of Equation *(166)* and explicitly stating the T_i^3 and $(T_v^3)^{-1}$ matrices produces Equation *(167)*:

$$\begin{bmatrix} i_{UL,dm} \\ i_{UL,cm} \\ i_{A,cm} \end{bmatrix} = p \begin{bmatrix} 1/2 & -1/2 & 0 \\ 1 & 1 & 0 \\ 0 & 0 & 1 \end{bmatrix} \begin{bmatrix} C_{Ug} & 0 & 0 \\ 0 & C_{Lg} & 0 \\ 0 & 0 & C_{Ag} \end{bmatrix} \begin{bmatrix} 1/2 & 1 & 0 \\ -1/2 & 1 & 0 \\ 0 & 0 & 1 \end{bmatrix} \begin{bmatrix} v_{CUL,dm} \\ v_{CUL,cm} \\ v_{CA,cm} \end{bmatrix} \tag{167}$$

Multiplying the matrices produces Equation *(168)*:

$$\begin{bmatrix} i_{UL,dm} \\ i_{UL,cm} \\ i_{A,cm} \end{bmatrix} = p \begin{bmatrix} \frac{1}{4}(C_{Ug} + C_{Lg}) & \frac{1}{2}(C_{Ug} - C_{Lg}) & 0 \\ \frac{1}{2}(C_{Ug} - C_{Lg}) & C_{Ug} + C_{Lg} & 0 \\ 0 & 0 & C_{Ag} \end{bmatrix} \begin{bmatrix} v_{CUL,dm} \\ v_{CUL,cm} \\ v_{CA,cm} \end{bmatrix} \tag{168}$$

All the relationships needed to resolve $v_{CA,cm}$ and $v_{CUL,cm}$ are specified in Equation *(168)*. Starting with the *A* branch, the equation used to solve for $v_{CA,cm}$ is identified as the bottom row of Equation *(168)* and is repeated as Equation *(169)*:

$$i_{A,cm} = pC_{Ag} v_{CA,cm} \tag{169}$$

Isolating the CM voltage source produces Equation *(170)*:

$$v_{CA,cm} = \frac{1}{pC_{Ag}} i_{A,cm} \tag{170}$$

Equation *(170)* establishes the necessary CM relationship for $v_{CA,cm}$ that can be substituted back into Equation *(162)*. The final term to solve for is $v_{CUL,cm}$. This voltage is identified as the middle row of Equation *(168)*. This relationship is highlighted in Equation *(171)*:

$$i_{UL,cm} = p\frac{1}{2}(C_{Ug} - C_{Lg}) v_{CUL,dm} + p(C_{Ug} + C_{Lg}) v_{CUL,cm} \tag{171}$$

Isolating $v_{CUL,cm}$ produces Equation *(172)*:

$$v_{CUL,cm} = \frac{1}{p(C_{Ug} + C_{Lg})} i_{CUL,cm} - \frac{C_{Ug} - C_{Lg}}{2\left(C_{Ug} + C_{Lg}\right)} v_{CUL,dm} \tag{172}$$

The relationships defined in Equations *(170)* and *(172)* provide the means to resolve the CM equations established previously in Equations *(162)* and *(163)*, respectively. The *A* branch has a straightforward decomposition. Restating Equation *(162)* and substituting in Equation *(170)* produces the final CM KVL equation for the A branch. Performing this substitution and isolating v_{Pg} produces Equation *(173)*:

$$v_{Pg} = -v_{A,cm} + \frac{1}{pC_{Ag}} i_{A,cm} + Z_h\left(i_{UL,cm} + i_{A,cm}\right) \tag{173}$$

Equation *(173)* defines the CM KVL loop for the A branch section starting at v_{Pg}. This KVL loop describes the behavior for all elements that exist in the CM equivalent relationship for this section. The relationship given by Equation *(173)* can be mapped to the CM equivalent circuit shown in Figure 63.

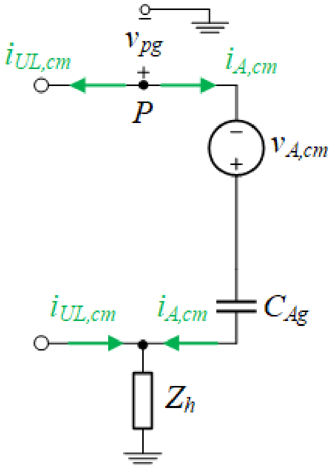

Figure 63. CM equivalent relationship of the A node

For the U/L branch, the same process is applied for Equation *(163)*. Restating Equation *(163)* and substituting in Equation *(172)* produces the final KVL equation for the U/L branch. Performing this substitution and isolating v_{Pg} produces Equation *(174)*:

$$\begin{aligned} v_{Pg} = -v_{UL,cm} + \left(\frac{1}{p\left(C_{Ug} + C_{Lg}\right)} i_{CUL,cm} - \frac{C_{Ug} - C_{Lg}}{2\left(C_{Ug} + C_{Lg}\right)} v_{CUL,dm}\right) \\ + Z_h\left(i_{UL,cm} + i_{A,cm}\right) \end{aligned} \tag{174}$$

Distributing the negative sign to the coefficient for $v_{CUL,dm}$ produces Equation *(175)*:

$$\begin{aligned} v_{Pg} = -v_{UL,cm} + \frac{1}{p\left(C_{Ug} + C_{Lg}\right)} i_{CUL,cm} + \frac{C_{Lg} - C_{Ug}}{2\left(C_{Ug} + C_{Lg}\right)} v_{CUL,dm} \\ + Z_h\left(i_{UL,cm} + i_{A,cm}\right) \end{aligned} \tag{175}$$

Equation *(175)* defines the CM KVL loop for the U/L branch section starting at v_{Pg}. This KVL loop describes the behavior for all elements that exist in the CM equivalent relationship for this section. The relationship given by Equation *(175)* can be mapped to the CM equivalent circuit shown in Figure 64. The only term that is not defined explicitly from Equation *(175)* is the DM voltage term $v_{CUL,dm}$. By the definition of the MM decomposition matrices, this term is defined by the DM voltage across the U and L nodes in the MM model about the switching devices. This term is also dependent on topology. In the case of the buck converter, it is readily seen from Figure 20(a) that $v_{CUL,dm}$ is defined by the dc bus voltage across the input capacitor C_i. Thus, the term $v_{CUL,dm} = v_{Ci}$ for the buck converter. In the case of the boost converter, it is readily seen from Figure 20(b) that $v_{CUL,dm}$ is defined by the voltage across the output capacitor C_o. Thus, the term $v_{CUL,dm} = v_{Co}$ for this topology.

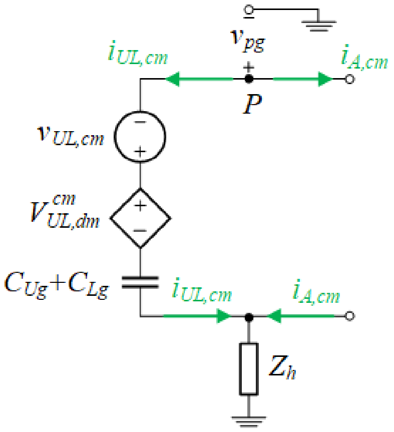

Figure 64. CM equivalent relationship for the U/L midpoint

As a final step, the CM KVL loops demonstrated in Equations *(173)* and *(175)* can be put together to define the complete CM equivalent circuit representation for the parasitic capacitance section of the buck and boost converters. The CEMs defined by these KVL loops are shown in Figure 23(a) and Figure 23(b) for the buck and boost converters, respectively. The reference point *P* is defined to be arbitrary but will be explicitly defined in the next section in order to create the final CEM.

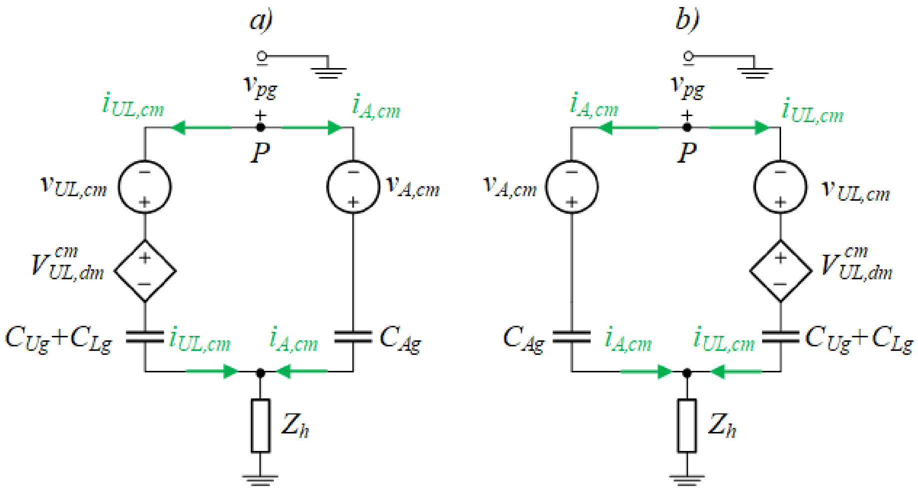

Figure 65. Parasitic BPC branch CM equivalent relationship for (a) buck and (b) boost converters

The voltage term $v_{UL,cm}$ is described by Equation *(40)*:

$$v_{UL,cm} = \frac{1}{2}(v_{UP} + v_{LP}) \tag{176}$$

The term $v_{A,cm}$ is described by Equation *(41)*:

$$v_{A,cm} = v_{AP} \tag{177}$$

Since $v_{UL,dm}^{cm}$ is topology dependent, it is handled in two separate equations. Equation *(42)* describes $v_{UL,dm}^{cm}$ for the buck converter:

$$v_{UL,dm}^{cm}(\text{buck}) = \frac{C_{Lg} - C_{Ug}}{2(C_{Ug} + C_{Lg})} v_{Ci} \tag{178}$$

Equation *(43)* describes $v_{UL,dm}^{cm}$ for the boost converter:

$$v_{UL,dm}^{cm}(\text{boost}) = \frac{C_{Lg} - C_{Ug}}{2(C_{Ug} + C_{Lg})} v_{Co} \tag{179}$$

A.7. CM Voltage Source Definition for Practical Buck Converter

Resolving the final CM voltage source definitions for the simplified buck converter is detailed in this section. Restating Equation *(40)* for $v_{UL,cm}$ with the midpoint of U, L as the reference point produces Equation *(180)*:

$$v_{UL,cm} = \frac{1}{2}\left(v_{U/U,L} + v_{L/U,L}\right) \tag{180}$$

The voltage $v_{U/U,L}$ represents the voltage from U to the midpoint of nodes U, L. This voltage is given by the midpoint voltage $\frac{1}{2}v_{Ci}$ for the buck converter. On the other hand, $v_{L/U,L}$ represents the voltage from L to the midpoint of nodes U, L. This voltage is given by the negative of the midpoint voltage, $-\frac{1}{2}v_{Ci}$, for the buck converter. Applying these values to Equation *(180)* produces Equation *(181)*:

$$v_{UL,cm} = \frac{1}{2}\left(\frac{1}{2}v_{Ci} - \frac{1}{2}v_{Ci}\right) = 0 \tag{181}$$

Therefore, $v_{UL,cm}$ is eliminated from the CEM.

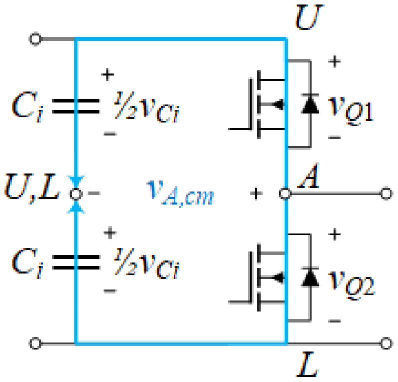

Figure 66. MM representation around the switching devices for the buck converter

The remaining voltage source to resolve is $v_{A,cm}$. Equation *(41)*, for this configuration, indicates that $v_{A,cm}$ represents the voltage defined from the A node to the midpoint of nodes U, L. This definition for the voltage source is particularly difficult to define for this system. Figure 66 indicates why this is the case. The voltage defining $v_{A,cm}$ is not described by one obvious path. The voltage could be defined through the lower rail by the series combination of v_{Q2} and $-\frac{1}{2}v_{Ci}$. Similarly, this voltage could be determined by a path through the upper rail by $-v_{Q1}$ in series with $\frac{1}{2}v_{Ci}$. Due to the lack of an obvious path, these two paths are averaged to provide a good approximation of the behavior of the MM voltage. Averaging the two paths to determine $v_{A,cm}$ produces Equation *(182)*:

$$v_{A,cm} = \frac{1}{2}\left(v_{Q2} - \frac{1}{2}v_{Ci} - v_{Q1} + \frac{1}{2}v_{Ci}\right) \tag{182}$$

It can be seen that v_{Ci} is eliminated from Equation *(182)*. Therefore, simplifying Equation *(182)* produces Equation *(44)*:

$$v_{A,cm} = \frac{1}{2}\left(v_{Q2} - v_{Q1}\right) \tag{183}$$

A.8. Construction of Final CEM for Practical Boost Converter

Resolving the final CM voltage source definitions for the simplified buck converter is detailed in this section. The analysis required to determine $v_{UL,cm}$ at the midpoint U, L is no different than what was described for the buck converter in Section 3.3.4.1. The previous analysis, given by Equation (181), demonstrates that $v_{UL,cm}$ referenced to the midpoint of nodes U, L is zero. Therefore, $v_{UL,cm}$ is eliminated from the CEM for the boost converter.

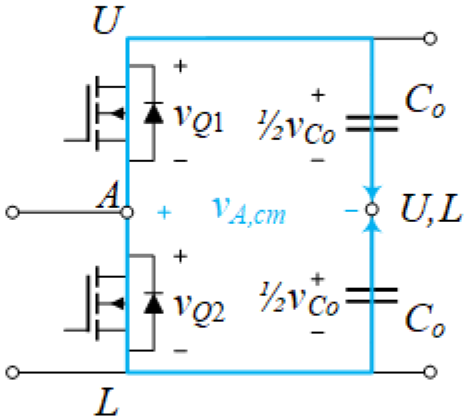

Figure 67. MM representation about the switching devices for the boost converter

The final voltage source left to resolve is $v_{A,cm}$. Equation *(41)*, with the midpoint of nodes U, L as the specified reference point, indicates that $v_{A,cm}$ represents the voltage defined from the A node to the midpoint U, L. Figure 67 shows the voltage source in question in reference to the MM model. Similar to the analysis for the buck converter in Section 3.3.4.1, $v_{A,cm}$ can be described by more than one path. This voltage could be defined through the lower rail by the series combination of v_{Q2} with $-\frac{1}{2}v_{Co}$. Alternatively, $v_{A,cm}$ could be defined by a path through the upper rail by $-v_{Q1}$ in series with $\frac{1}{2}v_{Co}$. Due to the similarity that the boost converter shares to the buck converter in resolving $v_{A,cm}$, the analysis given in Section 3.3.4.1 can be directly leveraged to describe this CM voltage source. Thus, the CM voltage source for $v_{A,cm}$ is defined in Equation *(44)*, which is restated here as Equation *(45)*:

$$v_{A,cm} = \frac{1}{2}\left(v_{Q2} - v_{Q1}\right) \tag{184}$$

A.9. Source Transformation of the Parasitic Branch

The analysis detailed in this section is focused on applying a source transformation to the two branches that constitute the parasitic BPC branch of the practical CEMs shown in Figure 68.

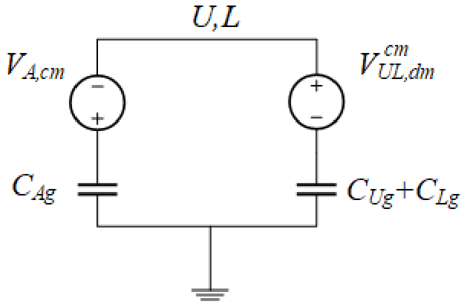

Figure 68. Original parasitic branch for the boost converter

For sake of the analysis, Z_{Culg} is labelled here as the frequency domain impedance representation for the combined capacitor $C_{Ug}+C_{Lg}$. Z_{Cag} is labelled as the frequency domain impedance representation for the capacitor C_{Ag}. Applying a source transformation from the voltage source of the U/L branch to a current source produces Equation *(185)*:

$$i_{dm}^{cm}=\frac{v_{UL,dm}^{cm}}{Z_{Culg}} \tag{185}$$

The same source transformation for the *A* branch produces Equation *(186)*:

$$i_{cm}=\frac{v_{A,cm}}{Z_{Cag}} \tag{186}$$

The impedance for each transformation is unchanged, but these elements are placed in parallel with the appropriate current sources given by Equations *(185)* and *(186)*. The transformed circuit is shown in Figure 69.

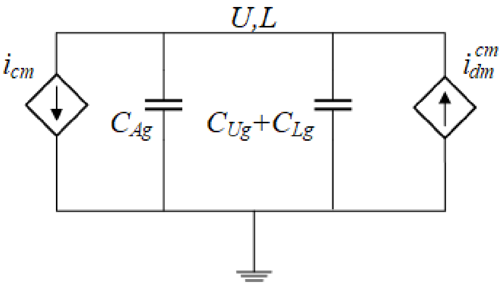

Figure 69. Source transformations of the parasitic branch

Since all elements in the system are defined at the same node, the system can be further simplified. Specifically, the capacitors are combined in parallel, and the current sources are added together with consideration of polarity. This results in a single capacitance defined as $C_{bp} \triangleq C_{Ug} + C_{Lg} + C_{Ag}$, with frequency domain impedance Z_{Cbp}. Noting the polarity of the current sources, the single current source is given by Equation *(187)*:

$$i_{tot} = -i_{cm} + i_{dm}^{cm} \tag{187}$$

Substituting in the definitions for i_{cm} and i_{dm}^{cm} produces Equation *(188)*:

$$i_{tot} = -\frac{v_{A,cm}}{Z_{Cag}} + \frac{v_{UL,dm}^{cm}}{Z_{Culg}} \tag{188}$$

The final step is in this process is to apply the source transformation once again to transition back to a voltage source. The result is shown in Figure 70.

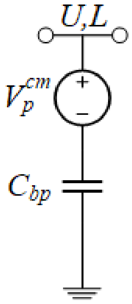

Figure 70. Final single branch transformation

The impedance is again unchanged but placed in series with the new voltage source. The voltage source is defined by Equation *(189)*:

$$v_p^{cm} = Z_{Cbp} i_{tot} \tag{189}$$

Substituting in for the current i_{tot} from Equation *(188)* produces Equation *(190)*:

$$v_p^{cm} = Z_{Cbp}\left(-\frac{v_{A,cm}}{Z_{Cag}} + \frac{v_{UL,dm}^{cm}}{Z_{Culg}}\right) \tag{190}$$

Distributing Z_{Cbp} produces Equation *(191)*:

$$v_p^{cm} = -\frac{Z_{Cbp}}{Z_{Cag}} v_{A,cm} + \frac{Z_{Cbp}}{Z_{Culg}} v_{UL,dm}^{cm} \tag{191}$$

Explicitly specifying the frequency domain representations of the impedances in Equation *(191)* produces Equation *(192)*:

$$v_p^{cm} = -\frac{\frac{1}{j\omega C_{bp}}}{\frac{1}{j\omega C_{Ag}}} v_{A,cm} + \frac{\frac{1}{j\omega C_{bp}}}{\frac{1}{j\omega (C_{Ug} + C_{Lg})}} v_{UL,dm}^{cm} \tag{192}$$

Normalizing the denominators of both coefficients by multiplying both the numerator and denominator of $v_{UL,dm}^{cm}$ by $j\omega (C_{Ug} + C_{Lg})$ and $v_{A,cm}$ by $j\omega C_{Ag}$ produces Equation *(193)*:

$$v_p^{cm} = -\frac{j\omega C_{Ag}}{j\omega C_{bp}} v_{A,cm} + \frac{j\omega (C_{Ug} + C_{Lg})}{j\omega C_{bp}} v_{UL,dm}^{cm} \tag{193}$$

Simplifying the expressions produces Equation *(194)*:

$$v_p^{cm} = -\frac{C_{Ag}}{C_{bp}} v_{A,cm} + \frac{(C_{Ug} + C_{Lg})}{C_{bp}} v_{UL,dm}^{cm} \tag{194}$$

Restating Equation *(194)* for the definitions of $v_{UL,dm}^{cm}$ and $v_{A,cm}$ with respect to the boost converter given by Equations *(45)* and *(43)*, respectively defines the final step. Substituting in the voltage equations for $v_{UL,dm}^{cm}$ and $v_{A,cm}$ produces Equation *(195)*:

$$v_p^{cm} = -\frac{C_{Ag}}{C_{bp}} \left[\frac{1}{2} \left(v_{Q2} - v_{Q1}\right)\right] + \frac{C_{Ug} + C_{Lg}}{C_{bp}} \left[\frac{1}{2} \frac{C_{Lg} - C_{Ug}}{C_{Ug} + C_{Lg}} v_{Co}\right] \tag{195}$$

A.10. Thevenin Equivalent Analysis of Practical Boost CEM

The analysis detailed in this section is focused on applying Thevenin equivalent circuit analysis techniques to the CEMs shown in Figure 15

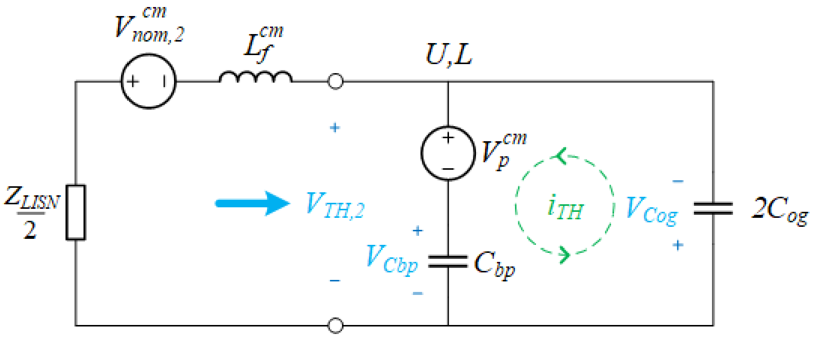

Figure 71. Original CEM for the boost converter

The remaining term to solve for is the Thevenin equivalent voltage source. The Thevenin voltage identified in Figure 32 is given by Equation *(196)*:

$$v_{TH,2} = v_p^{cm} + v_{Cbp} \tag{196}$$

The value for v_{Cbp} is initially unknown, but it can be resolved by finding the current i_{th}. Performing the KVL loop in the direction of the current shown in Figure 32 produces Equation *(197)*:

$$v_p^{cm} + v_{Cbp} + v_{Cog} = 0 \tag{197}$$

Isolating v_{Cbp} and v_{Cog} and expressing these voltage sources in terms of i_{TH} produces Equation *(198)*:

$$Z_{Cbp} i_{TH} + Z_{Cog} i_{TH} = -v_p^{cm} \tag{198}$$

Combining similar terms and isolating for i_{TH} produces Equation *(199)*:

$$i_{TH} = -\frac{1}{Z_{Cbp} + Z_{Cog}} v_p^{cm} \tag{199}$$

With i_{TH} isolated, it is possible to solve for the Thevenin equivalent voltage. Expressing v_{Cbp} in terms of i_{TH} and substituting that relationship into Equation *(196)* produces Equation *(200)*:

$$v_{TH,2} = v_p^{cm} + Z_{Cbp} i_{TH} \tag{200}$$

Substituting Equation *(199)* for i_{TH} into Equation *(200)* produces Equation *(201)*:

$$v_{TH,2} = v_p^{cm} - \frac{Z_{Cbp}}{Z_{Cbp} + Z_{Cog}} v_p^{cm} \tag{201}$$

Expressing the terms of the coefficients by their frequency domain representations produces Equation *(202)*:

$$v_{TH,2} = v_p^{cm} - \frac{\frac{1}{j\omega C_{bp}}}{\frac{1}{j\omega C_{bp}} + \frac{1}{j\omega(2C_{og})}} v_p^{cm} \tag{202}$$

Multiplying the denominator and numerator by $j\omega C_{bp}(2C_{og})$ and simplifying the coefficients into one expression for v_p^{cm} produces Equation *(203)*:

$$v_{TH,2} = \left(1 - \frac{2C_{og}}{2C_{og} + C_{bp}}\right) v_p^{cm} \tag{203}$$

Simplifying the coefficient produces Equation *(204)*:

$$v_{TH,2} = \left(\frac{2C_{og} + C_{bp} - 2C_{og}}{2C_{og} + C_{bp}}\right) v_p^{cm} \tag{204}$$

Further simplifying the coefficient produces Equation *(205)*:

$$v_{TH,2} = \frac{C_{bp}}{C_{bp} + 2C_{og}} v_p^{cm} \tag{205}$$

Substituting in the definition for v_p^{cm} from Equation *(52)* into Equation *(205)* produces Equation *(206)*:

$$v_{TH,2} = \frac{C_{bp}}{C_{bp} + 2C_{og}} \left\{ \frac{1}{2} \left[\frac{C_{Ag}}{C_{bp}} \left(v_{Q1} - v_{Q2}\right) + \frac{C_{Lg} - C_{Ug}}{C_{bp}} v_{Co} \right] \right\} \tag{206}$$

Distributing the outer coefficient leads to the elimination of the C_{bp} terms in the denominator of each coefficient.

A.11. Simplification of Practical Boost CM Voltage

This section is concerned with simplifying the CM voltage source term found for the practical boost converter. Defining $q_{ac} \triangleq \frac{C_{Ag}}{C_{bp}+2C_{og}}$ and $q_{dc} \triangleq \frac{C_{Lg}-C_{Ug}}{C_{bp}+2C_{og}}$ and substituting these definitions into Equation *(55)* produces Equation *(207)*:

$$v_{tot}^{cm} = \frac{1}{2}\left\{\left[v_{Q2} - \frac{a}{1-m}\left(v_{Q2} - v_{Ci}\right) - v_{Co}\right] + \left[q_{dc}v_{Co} + q_{ac}\left(v_{Q1} - v_{Q2}\right)\right]\right\} \tag{207}$$

Simplifying Equation *(207)* for similar terms produces Equation *(208)*:

$$v_{tot}^{cm} = \frac{1}{2}\left[\left(1 - \frac{a}{1-m}\right)v_{Q2} + \frac{a}{1-m}v_{Ci} + (q_{dc} - 1)v_{Co} + q_{ac}\left(v_{Q1} - v_{Q2}\right)\right] \tag{208}$$

Simplifying the coefficient for the single v_{Q2} term produces Equation *(209)*:

$$v_{tot}^{cm} = \frac{1}{2}\left[\left(\frac{1-m-a}{1-m}\right)v_{Q2} + \frac{a}{1-m}v_{Ci} + (q_{dc} - 1)v_{Co} + q_{ac}\left(v_{Q1} - v_{Q2}\right)\right] \tag{209}$$

Splitting the single v_{Q2} term into two equal quantities produces Equation *(210)*:

$$\begin{aligned} v_{tot}^{cm} = \frac{1}{2}\Bigg[&\left(\frac{1-m-a}{1-m}\right)\frac{v_{Q2}}{2} + \left(\frac{1-m-a}{1-m}\right)\frac{v_{Q2}}{2} + \frac{a}{1-m}v_{Ci} + (q_{dc} - 1)v_{Co} \\ &+ q_{ac}\left(v_{Q1} - v_{Q2}\right)\Bigg] \end{aligned} \tag{210}$$

In order to simplify the expressions between $\left(v_{Q1} - v_{Q2}\right)$ and the single v_{Q2} term, a new quantity is simultaneously added and subtracted from Equation *(210)* to keep the expression consistent. The additional terms are associated with v_{Q1}, and they are highlighted in red in Equation *(211)*:

$$\begin{aligned} v_{tot}^{cm} = \frac{1}{2}\Bigg[&\left(\frac{1-m-a}{1-m}\right)\frac{v_{Q2}}{2} - \left(\frac{1-m-a}{1-m}\right)\frac{v_{Q1}}{2} + \left(\frac{1-m-a}{1-m}\right)\frac{v_{Q1}}{2} \\ &+ \left(\frac{1-m-a}{1-m}\right)\frac{v_{Q2}}{2} + \frac{a}{1-m}v_{Ci} + (q_{dc} - 1)v_{Co} \\ &+ q_{ac}\left(v_{Q1} - v_{Q2}\right)\Bigg] \end{aligned} \tag{211}$$

Each highlighted term is combined with the single v_{Q2} terms in proximity, and this produces Equation *(212)*:

$$v_{tot}^{cm} = \frac{1}{2}\left[\left(\frac{1-m-a}{1-m}\right)\frac{v_{Q2} - v_{Q1}}{2} + \left(\frac{1-m-a}{1-m}\right)\frac{v_{Q1} + v_{Q2}}{2} + \frac{a}{1-m}v_{Ci} + (q_{dc}-1)v_{Co} + q_{ac}\left(v_{Q1} - v_{Q2}\right)\right] \tag{212}$$

To combine similar coefficients, a negative sign is applied to the coefficient in front of $\frac{v_{Q2}-v_{Q1}}{2}$. Applying this negative sign and extracting a coefficient of $\frac{1}{2}$ from the term $q_{ac}\left(v_{Q1} - v_{Q2}\right)$ produces Equation *(213)*:

$$v_{tot}^{cm} = \frac{1}{2}\left[-\left(\frac{1-m-a}{1-m}\right)\frac{v_{Q1} - v_{Q2}}{2} + \left(\frac{1-m-a}{1-m}\right)\frac{v_{Q1} + v_{Q2}}{2} + \frac{a}{1-m}v_{Ci} + (q_{dc}-1)v_{Co} + 2q_{ac}\frac{v_{Q1} - v_{Q2}}{2}\right] \tag{213}$$

Combining similar terms with respect to $\left(v_{Q1} - v_{Q2}\right)$ produces Equation *(214)*:

$$v_{tot}^{cm} = \frac{1}{2}\left[\left(2q_{ac} - \frac{1-m-a}{1-m}\right)\frac{v_{Q1} - v_{Q2}}{2} + \left(\frac{1-m-a}{1-m}\right)\frac{v_{Q1} + v_{Q2}}{2} + \frac{a}{1-m}v_{Ci} + (q_{dc}-1)v_{Co}\right] \tag{214}$$

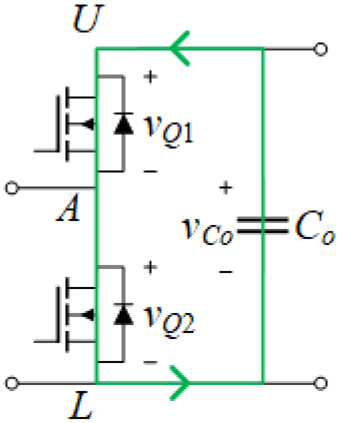

Figure 72. KVL loop around switching devices

Further simplifying the total CM voltage source requires redefining MM voltage sources. By taking advantage of the KVL loop shown in Figure 72, $v_{Q1} + v_{Q2}$ can be readily simplified to be equal to v_{Co}. This simplification produces Equation *(215)*:

$$v_{tot}^{cm} = \frac{1}{2}\left[\left(2q_{ac} - \frac{1-m-a}{1-m}\right)\frac{v_{Q1} - v_{Q2}}{2} + \left(\frac{1-m-a}{1-m}\right)\frac{v_{Co}}{2} + \frac{a}{1-m}v_{Ci} + (q_{dc} - 1)v_{Co}\right] \tag{215}$$

Simplifying similar terms with respect to v_{Co} produces Equation *(216)*:

$$v_{tot}^{cm} = \frac{1}{2}\left[\left(2q_{ac} - \frac{1-m-a}{1-m}\right)\frac{v_{Q1} - v_{Q2}}{2} + \frac{a}{1-m}v_{Ci} + \left(\frac{1-m-a}{2(1-m)} + q_{dc} - 1\right)v_{Co}\right] \tag{216}$$

Extracting a coefficient of $\frac{1}{2}$ from the term v_{Co} produces Equation *(217)*:

$$v_{tot}^{cm} = \frac{1}{2}\left[\left(2q_{ac} - \frac{1-m-a}{1-m}\right)\frac{v_{Q1} - v_{Q2}}{2} + \frac{a}{1-m}v_{Ci} + \left(\frac{1-m-a}{1-m} + 2q_{dc} - 2\right)\frac{v_{Co}}{2}\right] \tag{217}$$

Rewriting the coefficient 2 as $\frac{2(1-m)}{1-m}$ and simplifying the coefficient for v_{Co} produces Equation *(218)*:

$$v_{tot}^{cm} = \frac{1}{2}\left[\left(2q_{ac} - \frac{1-m-a}{1-m}\right)\frac{v_{Q1} - v_{Q2}}{2} + \frac{a}{1-m}v_{Ci} + \left(2q_{dc} + \frac{1-m-a-2(1-m)}{1-m}\right)\frac{v_{Co}}{2}\right] \tag{218}$$

A.12. Thevenin Equivalent Analysis of Practical Buck CEM

The analysis detailed in this section is focused on applying Thevenin equivalent circuit analysis techniques to the CEMs shown in Figure 15

The Thevenin impedance is found by shorting the voltage sources and combining the remaining elements into a single lumped component. As can be seen in Figure 40, shorting v_p^{cm} and $v_{nom,1}^{cm}$ leaves C_{bp} in parallel with the series combination of L_f^{cm} and $2C_{og}$. The equivalent representation of the passive elements' combination seen in Figure 40 produces Equation *(68)*:

$$Z_{TH} = \frac{Z_{Cbp}(Z_{Lf} + Z_{Cog})}{Z_{Cbp} + Z_{Lf} + Z_{Cog}} \tag{219}$$

where Z_{Cbp}, Z_{Lf}, and Z_{Cog} represent the frequency domain impedance relationships for C_{bp}, L_f^{cm}, and $2C_{og}$, respectively. Equation *(68)* can be resolved into a single impedance defined by a transfer function, but this additional complexity does not provide improved clarity. Therefore, the impedance is left as a parallel combination between C_{bp} and the series combination of L_f^{cm} and $2C_{og}$.

The final term necessary to complete the analysis is the Thevenin equivalent voltage source. As shown in Figure 40, the Thevenin voltage source is the series combination of v_p^{cm} and the voltage across the BPC, v_{Cbp}, which is given by Equation *(220)*:

$$v_{TH,1} = v_p^{cm} + v_{Cbp} \tag{220}$$

The term v_p^{cm} is well defined, but v_{Cbp} needs to be resolved by isolating the current i_{TH}. Performing the KVL loop specified in Figure 40 produces Equation *(221)*:

$$v_p^{cm} + v_{Cbp} + v_{Cog} + v_{Lf} + v_{nom,1}^{cm} = 0 \tag{221}$$

Isolating v_{Cbp}, v_{Cog}, and v_{Lf} and expressing these voltage sources in terms of i_{TH} produces Equation *(222)*:

$$Z_{Cbp} i_{TH} + Z_{Cog} i_{TH} + Z_{Lf} i_{TH} = -v_p^{cm} - v_{nom,1}^{cm} \tag{222}$$

Combining similar terms and isolating for i_{TH} produces Equation *(223)*:

$$i_{TH} = \frac{-1}{Z_{Cbp} + Z_{Cog} + Z_{Lf}} \left(v_p^{cm} + v_{nom,1}^{cm} \right) \tag{223}$$

Expressing v_{Cbp} in terms of i_{TH} and substituting that relationship into the Thevenin voltage expression given by Equation *(220)* produces Equation *(224)*:

$$v_{TH,1} = v_p^{cm} + Z_{Cbp} i_{TH} \tag{224}$$

Substituting Equation *(223)* for i_{TH} into Equation *(224)* produces Equation *(225)*:

$$v_{TH,1} = v_p^{cm} - \frac{Z_{Cbp}}{Z_{Cbp} + Z_{Cog} + Z_{Lf}} \left(v_p^{cm} + v_{nom,1}^{cm} \right) \tag{225}$$

The coefficient related to the ratio of impedances in Equation *(225)*, is labelled here as q_{TH}. Analyzing this coefficient further is beneficial to understanding the model. Explicitly stating the definition given for the coefficient produces Equation *(226)*:

$$q_{TH} = \frac{Z_{Cbp}}{Z_{Cbp} + Z_{Cog} + Z_{Lf}} \tag{226}$$

Expressing the impedances for their frequency domain representations produces Equation *(227)*:

$$q_{TH} = \frac{\frac{1}{j\omega C_{bp}}}{\frac{1}{j\omega C_{bp}} + \frac{1}{j\omega 2 C_{og}} + j\omega L_f^{cm}} \tag{227}$$

Normalizing q_{TH} by multiplying the numerator and denominator by $j\omega C_{bp}$ produces Equation *(228)*:

$$q_{TH} = \frac{1}{1 + \frac{j\omega C_{bp}}{j\omega 2 C_{og}} + (j\omega)^2 C_{bp} L_f^{cm}} \tag{228}$$

Simplifying the expression further produces Equation *(69)*:

$$q_{TH} = \frac{1}{1 + \frac{C_{bp}}{2 C_{og}} - \omega^2 C_{bp} L_f^{cm}} \tag{229}$$

Equation *(69)* provides a concise description of the frequency dependence of the CM behavior of the buck CEM, which is one of the key differences from the boost CEM. By leveraging this definition of q_{TH}, the final voltage source can be updated from Equation *(225)* to Equation *(230)*:

$$v_{TH,1} = v_p^{cm} - q_{TH}\left(v_p^{cm} + v_{nom,1}^{cm}\right) \tag{230}$$

Simplifying the expression produces Equation *(70)*:

$$v_{TH,1} = (1 - q_{TH})v_p^{cm} - q_{TH}v_{nom,1}^{cm} \tag{231}$$